BIOPHYSICAL CHARACTERIZATION OF LIVING CELLS AND MEMBRANE RECEPTORS BY ATOMIC FORCE SPECTROSCOPY

A Dissertation
Submitted to the Graduate Faculty
of the
North Dakota State University
of Agriculture and Applied Science

By

Lina Alhalhooly

In Partial Fulfillment of the Requirements
for the Degree of
DOCTOR OF PHILOSOPHY

Major Program:
Physics

October 2021

Fargo, North Dakota

North Dakota State University
Graduate School

Title

BIOPHYSICAL CHARACTERIZATION OF LIVING CELLS AND MEMBRANE RECEPTORS BY ATOMIC FORCE SPECTROSCOPY

By

Lina Alhalhooly

The Supervisory Committee certifies that this ***disquisition*** complies with North Dakota State University's regulations and meets the accepted standards for the degree of

DOCTOR OF PHILOSOPHY

SUPERVISORY COMMITTEE:

Dr. Yongki Choi
Chair

Dr. Alan Denton

Dr. Erik Hobbie

Dr. Sanku Mallik

Approved:

10/08/2021
Date

Dr. Sylvio May
Department Chair

ABSTRACT

Cellular biomechanics and cellular communication via receptor-ligand interactions play an important role in controlling cell development and maintaining cellular functions. Atomic force spectroscopy (AFM) technique has been widely used to characterize the changes in cellular biomechanics and quantify the receptor-ligand interactions. In this dissertation, we introduce working principles of AFM-based force spectroscopy, visualize cross-communications between membrane mechanics and cellular signaling, and identify quantitative relationship between receptor-ligand binding dynamics and multivalent interactions.

First, by exploiting force spectroscopy methods, we probed biomechanical kinetics (stiffness, morphology, roughness, adhesion) of the brain, breast, prostate, and pancreatic cancer cells with standard chemotherapeutic drugs in normoxia and hypoxia over 12 – 24 hours. After exposure to the drugs, we found that brain, breast, and pancreatic cancer cells became approximately 20 – 50% less stiff, while prostate cancer cells became more stiff, due to either drug-induced disruption or reinforcement of cytoskeletal structure. However, the rate of the stiffness change decreased up to 2-folds in hypoxia, suggesting a correlation between cellular stiffness and drug resistance of cancer cells in hypoxic tumor microenvironment. Our results show that a degree of chemotherapeutic drug effects on biomechanical and biophysical properties of cancer cells is distinguishable in normoxia and hypoxia, which are correlated with alteration of cytoskeletal structure and integrity during a drug-induced apoptotic process.

Second, we probed the binding strength of ligand-receptor interactions on live pancreatic cancer cells using single-molecule force spectroscopy methods, in which the peptides (cyclic arginine-glycine-aspartic acid: cRGD) was functionalized on a force probe tip through the polyethylene glycol-based bifunctional linker molecules. Although the density of integrin

heterodimer receptors on the cell surface of each cell differs from cell to cell, the individual cRGD-integrin complexes exhibited a cell type-independent, monovalent bond strength. The load-dependent, bond strength of multivalent cRGD-integrin interactions scaled sublinearly with increasing bond number, consistent with the noncooperative, parallel bond model. Comparison of energy landscapes of the bond number revealed a substantial decrease of kinetic off rates for multivalent bonds, along with the widened width of the potential well and the increased potential barrier height between bound and unbound state, enhancing the stability of multivalent bonds between them.

ACKNOWLEDGMENTS

First, I would like to express my gratitude to my advisor Dr. Yongki Choi for his guidance and excellent advice throughout my PhD, without whom I would not have been able to complete this research. I would like to thank my supervisory committee, Dr. Alan Denton, Dr. Sanku Mallik, and Dr. Eric Hobbie for their consultancy and great support.

I am also so grateful having wonderful colleagues in Dr. Choi's lab: Dr. Sung Oh Woo, James Froberg, Myungkeun Oh, and Sakura Tani, thank you so much for your encouragement, support, and the enjoyable discussions.

I would also like to thank the physics department for supporting me throughout my PhD. The department chair, Dr. Sylvio May who always supports and helps students. Also, my academic advisor Dr. Alan Denton who endlessly supports students and he is such as an inspiration to me and to many. Thanks for all faculty, students, and staff for making the time that I have spent at NDSU physics department enjoyable and valuable.

I would also like to acknowledge our collaborators who significantly contributed to this research. First, special thanks for Dr. Sanku Mallik in pharmaceutical sciences for his great contribution and support. Also, Dr. Mallik's group members helped me a lot. Thanks so much for Matthew Confeld for his extensive support, preparing samples and doing a lot of work for my research. Thanks a lot for Babak Mamnoon for his great contribution in this research. Thanks for Jessica Pullan for collaboration. I would like to thank Dr. Jiha Kim from biological science department for her collaboration, support, and encouragement. Also, I like to thank Dr. Kim's student Reed Jacobson for helping us.

Finally, I would like to acknowledge my husband Khaled for his love, support, and patience. Thanks for my wonderful daughters, Lilas and Batool for encouraging me and being

patient and independent throughout my study. Thanks for my family in Jordan, especially my lovely parents who always support, encourage, and keep me in their prayers.

DEDICATION

This dissertation is dedicated to my parents, Ahmad Issa and Fatima. I also dedicated my dissertation to my sister Ghada Alhalhooly.

TABLE OF CONTENTS

LIST OF TABLES

LIST OF FIGURES

CHAPTER 1. INTRODUCTION

Nanotechnology-based tools applied in biological sciences have been well developed and served as powerful techniques for studying biology and biophysics at a single cell or molecule level. For example, fluorescence resonance energy transfer (FRET) [1], stochastic optical reconstruction microscope (STORM) [2], transmission electron microscope (TEM), scanning electron microscope (SEM) [3], and atomic force microscope (AFM) [4] have been widely used to investigate biomechanical and biophysical properties of biological materials. Among these techniques, AFM has proven its efficacy in providing high throughput quantitative analysis through high resolution imaging, 3D characterization, and mechanically probing single-molecule interactions. Furthermore, all these capabilities can be performed in the physiological environment in real-time [5] [6] [7].

Investigating the living cell communication frontlines such as the cell surface and membrane receptors is of great significance for biological and pharmaceutical sciences[8] [9] [10]. Cellular biomechanics and cellular communication through receptors play an important role in controlling cell development and maintaining cellular functions [11] [12] [13]. AFM-based force spectroscopy technique has been employed extensively in exploring the biophysical properties of cell surface and membrane receptors [14] [15] [16]. For these reasons, cellular biomechanics and receptor-ligand membrane interactions were studied using AFM in this thesis.

The working principles of the AFM technique as well as the theoretical approach of the AFM-based measurements were demonstrated in chapter 2 and chapter 3. In chapter 2, the imaging and force spectroscopy procedures of measuring elasticity for biomolecules and living cells were described. Then, single-molecule force spectroscopy technique besides the AFM-tip

functionalization were introduced in chapter 3. Additionally, the dynamical analysis of the membrane receptor-ligand interactions was illustrated.

In chapter 4, the biomechanical and biophysical properties of four cancer cell lines were quantified under chemotherapeutic drug exposure using AFM in normoxic and hypoxic conditions. First, the cellular elasticity was measured in a time-dependent manner before and after treatment in both conditions: normoxia and hypoxia. Then, the morphological alterations due to the drug exposure were investigated under similar conditions. Our results have shown direct evidence of the drug-induced changes of the cytoskeletal components, as well as the effect of a low-oxygen environment on enhancing the cancer cell resistance against the chemotherapeutic treatment.

In chapter 5, single and multiple interactions between α_v integrin receptors and cRGD ligands were investigated using AFM. First, the unbinding force of the single receptor-ligand bond was quantified. Then, force-based receptor distributions were compared between three pancreatic cancer cell lines and a healthy pancreas cell line. Next, the thermodynamic and kinetic parameters were examined for single receptor-ligand bindings upon varying the loading rates. Finally, the multivalent interactions of the α_v integrin-cRGD bindings were quantified and the thermodynamic parameters were analyzed. Based on our results, a comprehensive quantitative description of α_v integrin and cRGD ligand interactions was provided.

CHAPTER 2. BIOMECHANICAL CHARACTERIZATION OF LIVING CELLS USING THE AFM

Introduction

The mechanical properties of a material are defined by how the material responds to any stimulus of external force. The relationship between the response, as a form of deformation, and the external force is given by the elasticity which is also called Young's modulus. The living cells have intrinsic viscoelastic characteristics in their physiological environments. The healthy cellular mechanics guarantees adequate physical and biochemical connections between the cell and the external environment. Thus, the cell keeps well-functioning and maintains its integrity.

Measuring the mechanical properties of cells is of great importance as cellular mechanics is directly related to cellular functions [17]. Cellular mechanics represents the main indicator of cell viability and cell ability to perform metabolic activities [18]. A variety of biomechanical and biophysical assay approaches such as micropipette aspiration [19], optical and magnetic tweezers [20] [21], mechanical microplate stretcher [22], and AFM have been used to measure the elasticity of living cells. Among those, the AFM method has emerged as a powerful tool to investigate biomechanical properties of single cells in physiological solutions in real-time [13] [23] [24]. In this chapter, I will describe the AFM working principles of imaging and measuring cellular biomechanical properties, as well as the theoretical approach of force measurements.

Atomic Force Microscope

Atomic Force Microscope (Figure 1) is comprised of a cantilever-tip assembly that raster scans across the sample surface using a piezoelectric tube controlled by a computer. The deflection of the cantilever is monitored using an optical detection system in the form of a laser

that reflects off the back of the cantilever and onto a four-quadrant photodiode while scanning. The feedback loop containing the piezo system maintains a constant tip-sample force.

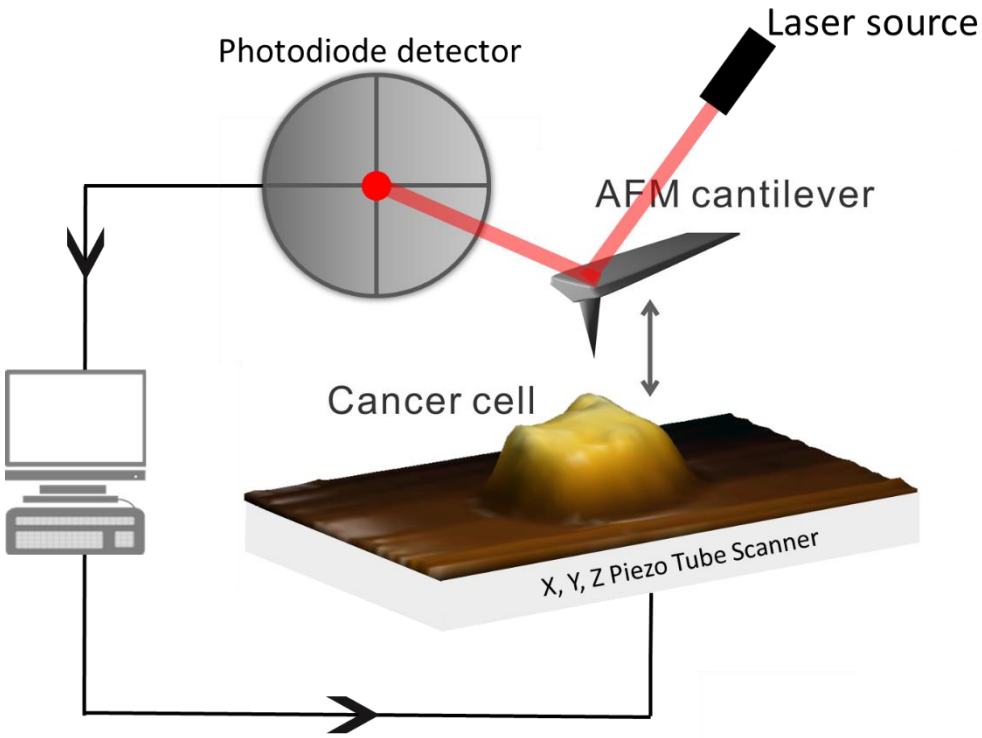

Figure 1. A representation scheme of AFM components and working principle. The cantilever deflection is monitored by a photodiode which controls the tip-sample separation to maintain a constant interaction force using a feedback loop.

AFM scanning can be done by operating in contact mode, where a constant cantilever deflection is maintained, or in semi-contact (tapping) mode where the cantilever oscillates near resonance and constant amplitude is maintained. AFM is also capable of force spectroscopy measurements. The great advantage of AFM is the possibility of performing measurements at very high resolution and in the liquid environment which is the natural medium for most biological samples. AFM can be used for topographical imaging, measuring mechanical properties, and investigating the biophysical properties of molecular interactions [25]. Another advantage comes from its real-time measurements [26], which provide not only static but also

dynamic information about the investigated sample. Thus, AFM can be applied to study many types of biological samples, ranging from small cellular structures (e.g., exosomes) to large ones like living cells.

AFM imaging principle

The origin of the AFM name is due to the basic principle of measuring repulsive or attractive interaction forces between the AFM tip atoms and the sample surface atoms. AFM operates imaging by moving the cantilever-tip assembly laterally to scan over the sample surface line by line. As the cantilever is elastic, tip-sample interaction easily affects the cantilever position. How the tip position changes depends on the operating mode used for imaging. The operating mode is chosen according to the elastic characteristics of both the cantilever and the sample. The two primary AFM modes are contact mode and semi-contact (tapping) mode.

In the contact mode, the cantilever deflection due to tip-sample interaction is monitored by a laser beam and maintained constant by a feedback loop. As a result, an iso-force image is created by recording the feedback signals as a topographic image. This mode is usually used for imaging hard materials using a cantilever with a high elastic constant.

In the tapping mode, the cantilever oscillates at a high amplitude near its resonance frequency. The tip-sample interaction affects the oscillation amplitude while the feedback loop maintains a constant amplitude. Then, the sample topography is recorded. Operating under the tapping mode allows the tip to interact with the sample only at the bottom of each oscillation cycle, protecting both the sample and the tip from damage. Thus, the tapping mode is suitable for imaging soft materials and biological molecules including living cells.

AFM force spectroscopy principle

In AFM force spectroscopy experiments, the cantilever and tip are moved directly towards the sample until they are in contact with it, and then retracted again, while the interaction between the tip and the sample is measured. When the cantilever approaches the sample, the indentation (cantilever deflection) remains zero until making a contact with the sample. The cantilever keeps indenting into the sample until the deflection reaches a target depth. Then AFM pulls the cantilever away from the sample. During this process, the cantilever deflection is recorded as a function of its location and the device provides data as a cantilever deflection vs. distance.

Force-distance curve

The force-distance (FD) curve explains the interaction between the cantilever tip and the sample. When the cantilever approaches the sample, the indentation (cantilever deflection) remains zero until making physical contact with the sample surface (at zero on the x-axis) as in Figure 2. The cantilever keeps indenting into the sample until the deflection reaches a target depth called set-point. Then, AFM pulls the cantilever away from the sample. Recording this process results in two curves: the approach curve (red line, Figure 2) and the retract curve (blue line, Figure 2). The stiffness of the sample determines the curve slope.

The raw data by AFM usually represents the dependence between the electrical signal, which is proportional to the cantilever deflection, and the vertical location of the cantilever which is converted into a tip-sample distance. Then, the indentation part of the approaching curve is used to fit with Hertz model (Figure 3). As a result, Young's modulus will be extracted.

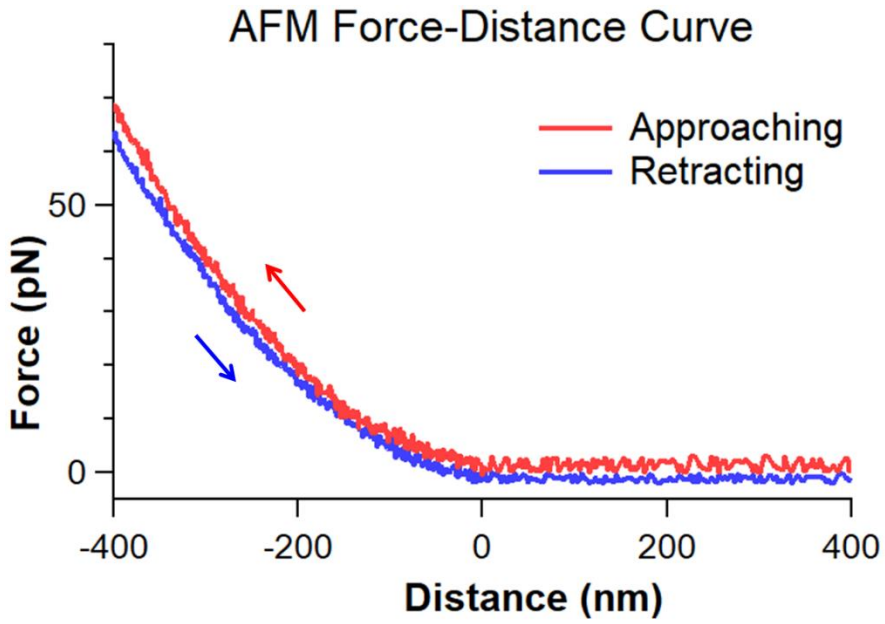

Figure 2. Typical FD curve recorded during approaching-retracting cycle between the AFM cantilever and a cancer cell surface.

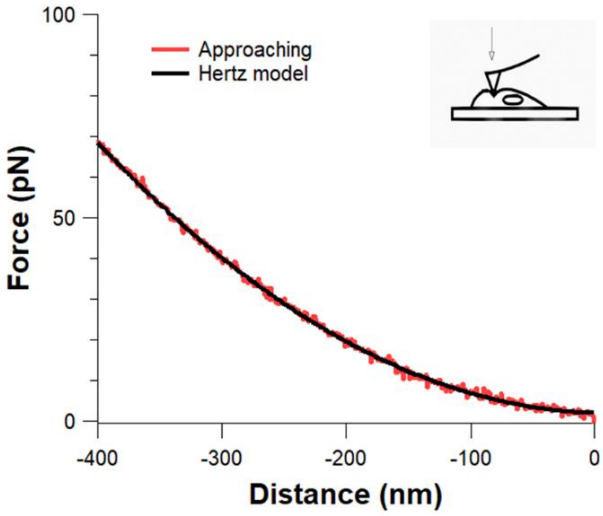

Figure 3. Fitting the data of approaching FD curve with Hertz model to extract Young's modulus.

The theoretical approach of cellular elasticity measurements

Young's modulus is a measure of material elasticity, defining the relationship between stress (force per unit area) and strain (proportional deformation). The relative cell stiffness (Young's modulus) is extracted from FD curves. The FD curves are obtained on the central

cytoplasmic region of the cell surface. To prevent cell damage and eliminate potential substrate effects, all measurements should be performed with a shallow indentation depth of cells (<500 nm). One can also determine the tip speed by setting the time needed to perform the FD curves in the approaching and retracting cycle. A fast tip may cause damage to the sample or to the tip itself. So, it is recommended that the tip velocity does not exceed 10 μm/s.

The Young's modulus is usually determined by fitting the FD curves with the Hertz model [27]. The FD curves should be converted to force-indentation curves. The force F is calculated from the cantilever deflection d and the cantilever spring constant k using Hooke's law ($F = kd$). The tip-sample separation called indentation δ is calculated through the difference between relative piezo displacement Δz and cantilever deflection d (i.e., $\delta = \Delta z - d$). Second, the force-indentation curves in the post-contact region are fitted by the Hertz model. Depending on the tip geometry (four-sided pyramid), the Young's modulus can be extracted using $F(\delta) = \left(\frac{E}{1-s^2}\frac{tan\alpha}{\sqrt{2}}\right)\delta^2$, where E is the Young's modulus, s is the Poisson's ratio, and α is the tip face angle. The Poisson's ratio is defined as the ratio between transverse strain to axial strain which describes how the volume changes under tensile pressure. Poisson's ratio value is 0.5 for typical soft biological samples in fluid, demonstrating that the material is perfectly incompressible and deformed elastically.

AFM Imaging of Biomolecules and Living Cells

Traditional methods used for characterizing biomolecules, such as X-ray crystallography [28], require pretreatment of the sample which modifies the natural characteristics of investigated structures. The AFM high-resolution images of biomolecules and living cells reveal structural details and conformational functional changes in real-time and in physiological conditions which cannot be examined by other approaches. Therefore, AFM is highly

recommended for investigating biological and cellular activities by tracking the structural changes.

AFM is widely used to image a variety of biomolecules as well as living cells at high lateral resolution and in the liquid environment [23]. AFM imaging requires to appropriately adjust scanning parameters according to the tip and the sample characteristics. The scanning parameters include interaction force magnitude, scanning speed, and scanning area. They should be carefully set to acquire the desired outcomes, depending on the molecule's deformability and size.

Examples of AFM images in air or liquid are shown here. The first example is imaging pancreatic cancer exosomes (PANC-1 exosomes) in the air (Figure 4), where the particles with around 50 nm height were imaged. Also, an AFM image for a living pancreatic cancer cell (PANC-1 cell) was obtained in the liquid which shows the cell surface topography, size, and how it spreads over the substrate (Figure 5). AFM has been recently employed in many important studies as a complementary tool such as testing drug delivery methods using nanoparticles [29] and characterizing bio-composites of immobilizing enzymes on graphene substrates [30] [31].

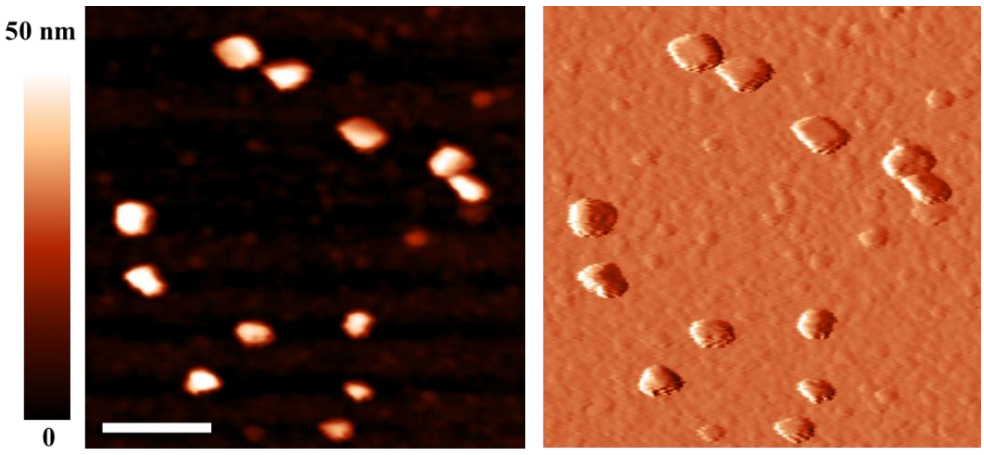

Figure 4. AFM images of PANC-1 exosomes in the air: topographical image (left) and deflection image (right). The scale bar is 250 nm.

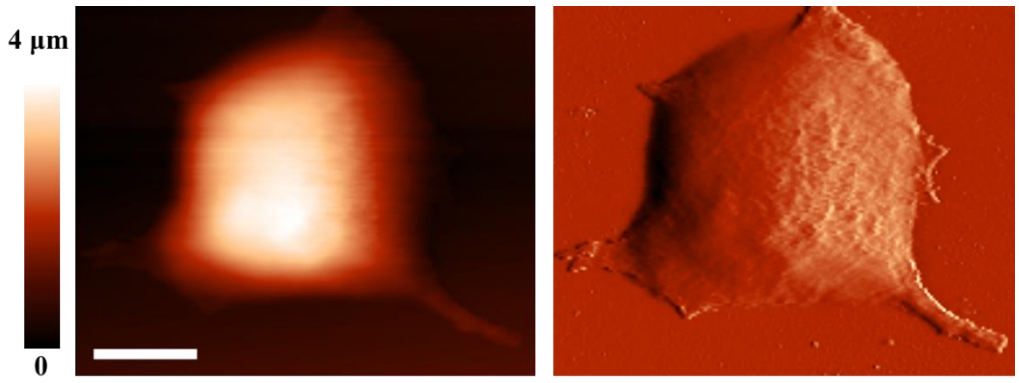

Figure 5. AFM images of living PANC-1 cell in the liquid: topographical image (left) and deflection image (right). The scale bar is 5 µm.

The AFM topographical image is recorded depending on the voltage applied to the z piezo ceramic system that is needed to keep the oscillation amplitude constant in tapping mode, or the deflection constant in case of contact mode. So, the topographical image demonstrates the height scale for the sample. On the other hand, the magnitude (deflection) image is recorded by measuring the error signal from the photodetector that represents the change in amplitude between each two adjacent recorded points, providing an image with more details of the scanned structures.

AFM Cellular Elasticity Measurements

Young's modulus was calculated for three pancreatic cancer cell lines, (PANC-1, BxPC-3, and MIA-PaCa-2), as well as a normal pancreas cell line hTERT-HPNE. First, each cell was imaged in the culturing medium at room temperature. Then, FD curves were recorded on the central region of the cell. AFM measurements were performed within 1-2 hours to maintain cell viability. The approaching and retracting speed of the probe (AFM tip) was 1 µm/s for all stiffness measurements. The elastic modulus for each cell was determined by fitting FD curves with the Hertz model.

At least 10 cells were tested by AFM force spectroscopy from each cell line. FD curves were obtained on the central region where at least five curves were taken at different positions. Figure 6 illustrates representative FD curves for each cell line, showing the force magnitude needed for indentation of 400 nm. Compared to the FD curve of hTERT-HPNE cell, less force is required for the three cancer (PANC-1, BxPC-3, and Mia-PaCa-2) cells to indent at the same depth, indicating that the cancerous cells are softer than the healthy cell.

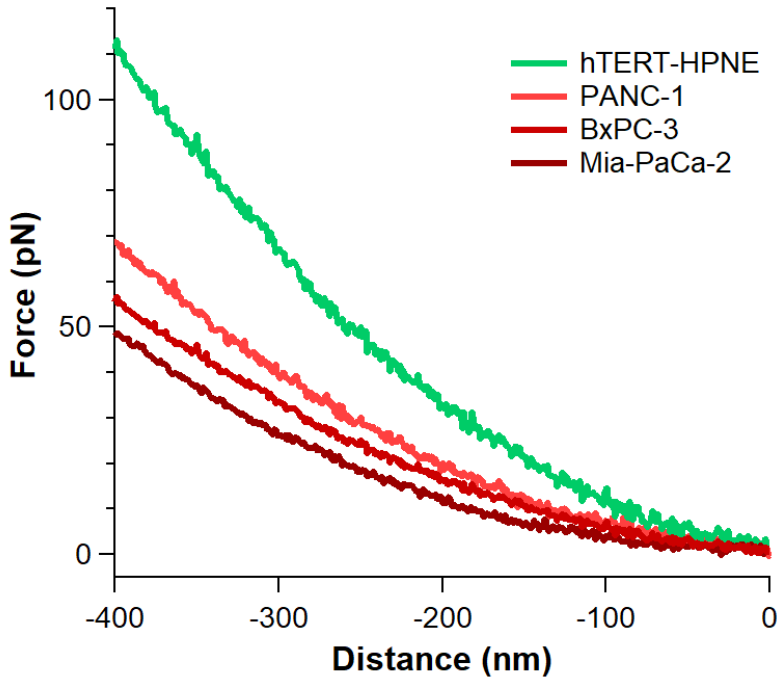

Figure 6. Cell-indentation portion of FD curves recorded during approaching process between the AFM tip and the cell surface of: hTERT-HPNE cell (green) and PANC1, BxPC-3, and Mia-PaCa-2 cells (red).

Analysis of all samples (Mia-PaCa-2 cells, n =10; BxPC-3 cells, n =21; PANC-1 cells, n =49) yielded average measured elastic moduli (mean ± SD) obtained using ex vivo culture sample for all cancerous cells of 0.45 ± 0.1 kPa, 0.52 ± 0.08 kPa, and 0.58 ± 0.06 kPa, respectively (Figure 7A, B, and C). Figure 7 shows histograms of the measured Young's modulus for all cancer and normal cells. The majority of the cell stiffness over the distribution

curve (mean ± SD) obtained for healthy pancreas cells hTERT-HPNE was 1.0±0.2 kPa, Figure 7D; (*n* =10).

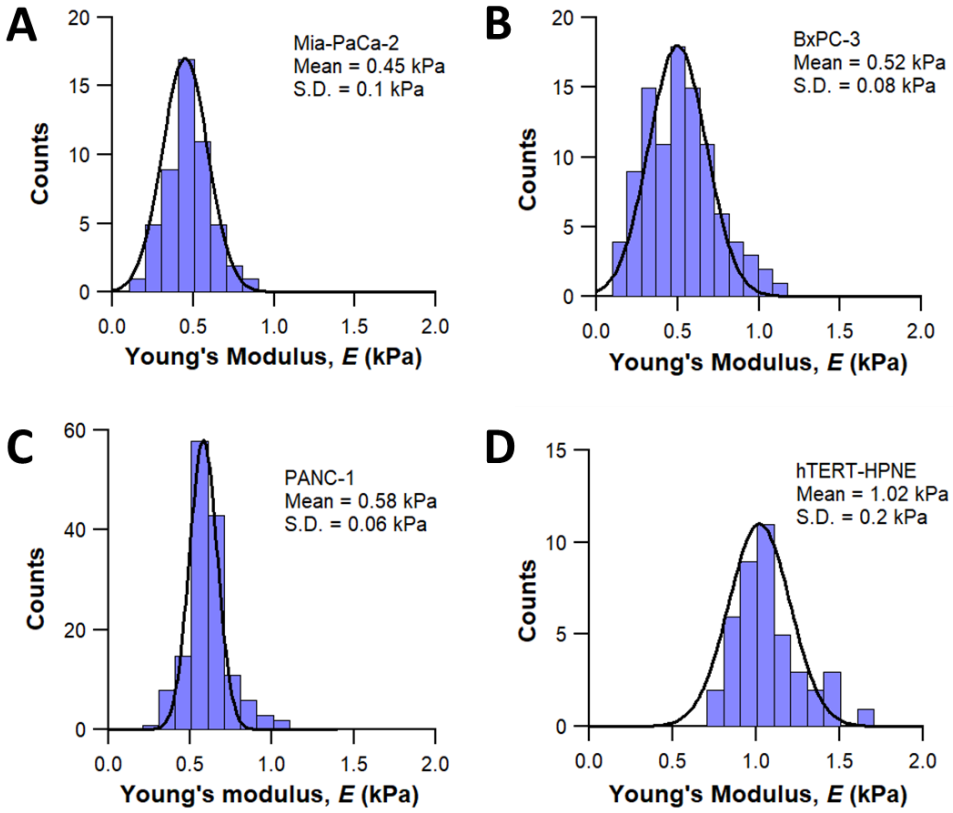

Figure 7. Histograms of the measured cell elasticity from three pancreatic cancer cell lines Mia-PaCa-2 (A), BxPC-3 (b), PANC-1 (C), and hTERT-HPNE (D). The majority of the young's modulus values are remarkably similar for the cancer cell lines while less than the normal cells values by nearly 50%.

In our study, AFM force spectroscopy measurements of Mia-PaCa-2 cells yielded very similar findings for BxPC-3 and PANC-1. On the other hand, performing the same experiment on the healthy cells hTERT-HPNE, revealed that the cancerous cells are around 50% softer than the normal cells. Furthermore, as our results showed that the elasticity of cancer cells is less than that of normal cells, this indicates that cancer cells showed increased deformability as compared to normal cells due to biochemical alterations resulting from the starting of disease, such as cancer metastasis [27] [32] [33].

CHAPTER 3. BIOPHYSICAL CHARACTERIZATION OF MEMBRANE RECEPTOR-LIGAND INTERACTIONS USING THE AFM

Introduction

AFM has proven its ability to measure piconewton forces at high lateral resolution in both air and liquid [34]. Therefore, it has increasingly been used to investigate biomolecular interactions at the single-molecule level in the physiological environment. One important way for living cells to initiate communication with surroundings is the cellular membrane receptors binding to ligands of the extracellular matrix or other cells. AFM has widely been used to quantify specific receptor-ligand interactions on the single-molecule level. Examples include investigating the adhesion forces of avidin-biotin pair [35] and studying the interaction between transforming growth factor-1 and its receptor in living cells [36].

The general strategy to investigate receptor-ligand interactions is to bind ligands to AFM tip to probe the receptors on the cell surface. The AFM single-molecule force spectroscopy SMFS technique enables measuring receptor-ligand interactions through the FD cycle. In the approaching-retracting round, the tip, carrying the ligands, is first approached the cell surface where receptor-ligand pair is formed. During subsequent tip retraction, an increase in force is applied due to the receptor-ligand bond until breaking this bond at a certain amount of force (rupture force).

The rupture force is also dependent on the rate of force change during the FD cycles [37]. Such experiments characterize the membrane receptor-ligand interactions and provide insight into the binding affinity, rate constants, and energy landscape parameters. In addition, receptor-ligand recognition experiments allow force-based localization of receptor binding sites over the living cell membrane [38].

In this chapter, I will present the SMFS principles as well as the protocols of binding ligands to AFM tips to be used for the SMFS experiments. Finally, the dynamic force model used in our dynamic analysis of cell membrane receptor and ligand interactions will be introduced here.

Single-Molecule Force Spectroscopy

Force spectroscopy technique

The spectroscopy term is usually used for describing the techniques studying matter-radiation interaction. Nevertheless, it is well-known in the scientific community that force spectroscopy is defined as probing interaction forces between biomolecules at the single-molecule level. The principle of this technique [38] relies on applying a pulling force to the molecule of study to measure its mechanical properties under stretching. Force spectroscopy technique can explore the physical principles underlying the mechanical functioning of biomolecules in the living systems which have still been investigated extensively.

Several powerful force spectroscopy techniques are available for investigating significant biological processes that rely on molecular interactions. These techniques include shear flow detachment [39], surface force apparatus [40], biomembrane force probe [41],optical tweezers [42], and AFM. AFM-based force spectroscopy has proven its efficiency in investigating high-resolution molecular interactions on a wide range of force scales in the physiological environment.

To probe cell membrane receptors, atomic force spectroscopy is applied using a ligand-coated tip, the schematic diagram is presented in Figure 8. To align the tip and cell surface, the tip is roughly positioned above a cell via an optical microscope and then performs the raster scanning to image the cell. From the acquired image, the position of the tip is selected above the

central cytoplasmic region of the cell surface. Then, arrays of FD curves are obtained over a selected area. Each FD curve reveals an event of receptor-ligand binding or no binding, depending on the receptor's existence in the contact site between the tip and cell surface. For the chosen area, the number of curves can be determined to achieve the desired resolution of recognition measurements scanning. Different resolutions are chosen through the study according to the purpose of mapping.

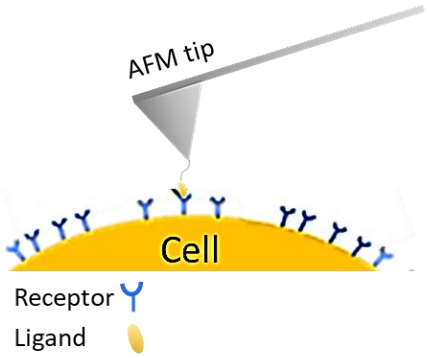

Figure 8. A scheme of ligand-functionalized AFM tip and cell surface receptors, where the binding occurs between the ligand and the cell receptor.

FD curves in SMFS experiments

The molecular recognition measurements are recorded by AFM through the FD curves. During recording the FD curve over the living cell surface, the tip initially approaches the cell, contacts the cell surface, further indents no more than 500 nm to guarantee the cell membrane safety and finally retracts from the contact. When the coated tip becomes in contact with the cell surface, the recognition event between a cell receptor and its conjugate ligand on the tip occurs. Then, when the tip retracts away from the cell, a specific signal is recorded due to the rupture between the ligand and the cell membrane receptor (Figure 9B), Figure 9A demonstrates the retracting FD curve with no recognition event. The unbinding force (rupture force) is simply identified (Figure 9B) as the force magnitude needed to break the bond: the difference between the lowest negative force and zero force of the system.

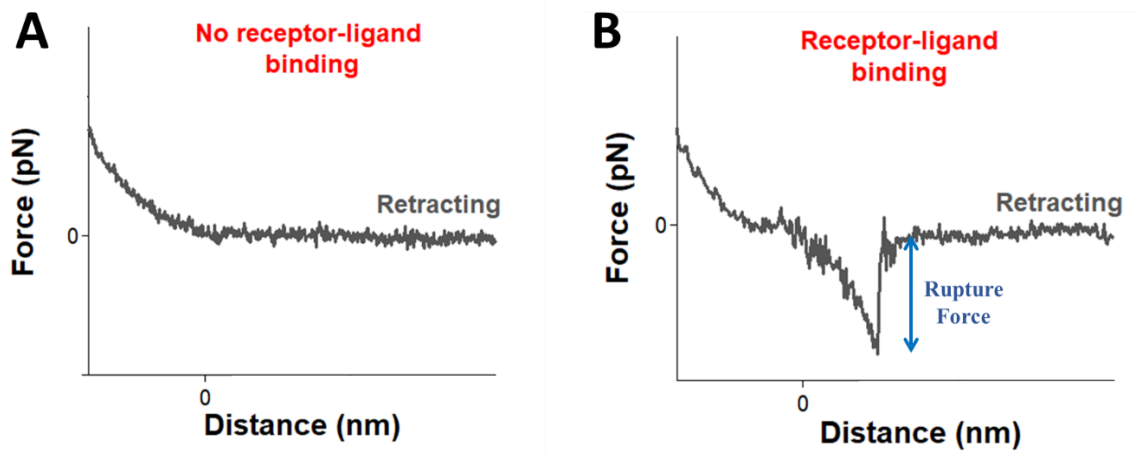

Figure 9. Representative retracting FD curves for: (A) no binding event between the ligand and receptor, and (B) receptor-ligand binding event.

Specific and nonspecific binding

The binding that occurs between the ligand and the receptor is classified as specific binding. On the other hand, nonspecific binding attributed to the adhesion between the tip surface and the cell membrane. The AFM tip may adhere to some molecules on the cell membrane while retracting. This adherence is usually weak and causes membrane lifting. Through the backward movement from the set point until detachment from the membrane, the tip bends (deflects) linearly without any relaxation. This is clear in the FD curve that contains nonspecific binding in Figure 10, the slope of retracting curve doesn't change until detachment from the cell membrane.

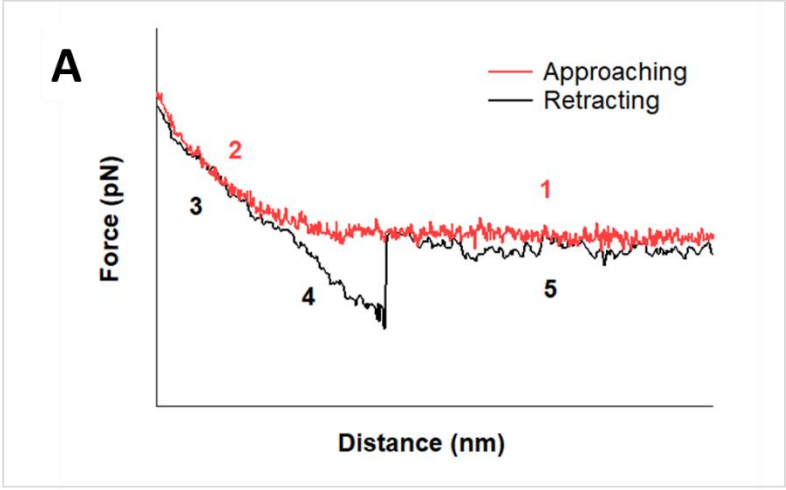

Figure 10. A representative retracting FD curve of nonspecific binding between the AFM tip and the cell membrane (A). A schematic configuration shows the AFM bending phases (B) corresponding to areas (1 to 5) on the FD curve in (A).

Modifying the AFM tip with ligands leads to specific binding with the cell receptors when performing the force spectroscopy measurements (Figure 11A). The ligand is usually attached to the tip by a linker. The linker causes a relaxation before rupturing from membrane receptor. When the tip detaches from the cell surface while the ligand binds to a receptor, the ligand linker leads to a relaxation in which the tip doesn't suffer any deflection for a moment. Then, the tip deflects again because of the binding force between the ligand and the receptor before the complete detachment (Figure 11B).

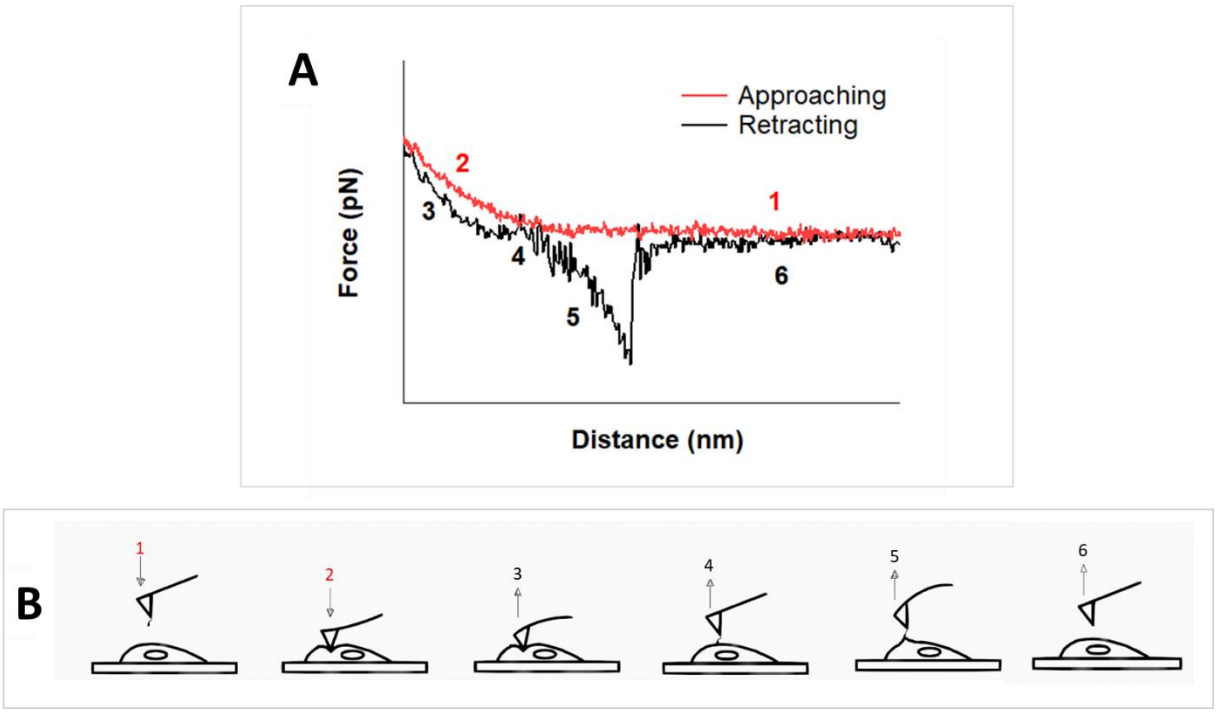

Figure 11. A representative retracting FD curve of specific binding between ligand-coated AFM tip and the ligand cognate cell membrane receptor (A). A schematic configuration shows the AFM bending phases (B) corresponding to areas (1 to 6) on the FD curve in (A).

However, both specific and nonspecific binding may occur in the same force spectroscopy measurement (Figure 12). During the retraction process in the FD cycle, the adhesion with the membrane takes place first. As this nonspecific adhesion is weak, the tip lifts the soft cell membrane a distance according to the membrane elasticity. Then, the detachment from the membrane occurs followed by a relaxation after which the receptor-ligand binding signal appears in the FD curve. The signal of receptor-ligand detachment in the FD curve looks like parabola (nonlinear) shape while it takes a linear shape for nonspecific binding. Furthermore, nonspecific binding signal also has the same slope of the tip-cell interaction between setpoint and contact point in the retracting curve.

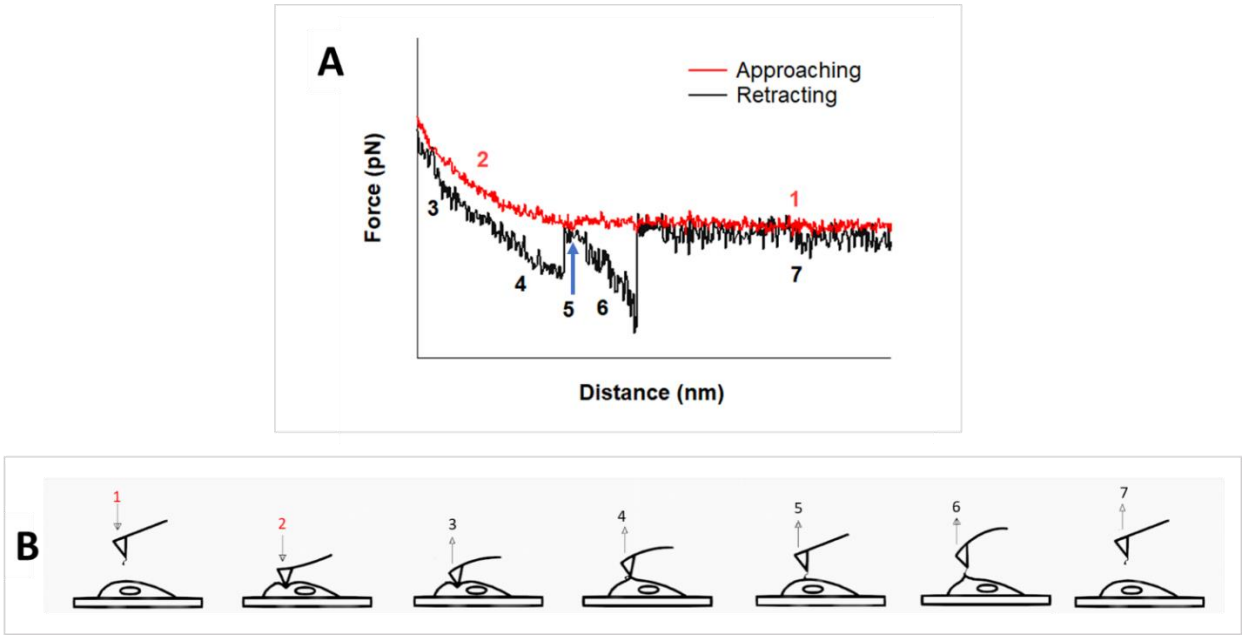

Figure 12. A representative retracting FD curve of specific and nonspecific bindings occur in the same force spectroscopy measurement (A). A schematic configuration shows the AFM bending phases (B) corresponding to areas (1 to 7) on the FD curve in (A).

Modifying the AFM tip with ligands reduces the nonspecific adherence between the tip and the membrane molecules , but even if specific and nonspecific bindings occur in the same force spectroscopy measurement, they are differentiated according to the linearity of FD curve signal, tip relaxation after the contact point, and the rupture force magnitude ($F_{Specific} > F_{Nonspecific}$).

To achieve a successful specific single-molecule binding spectroscopy measurement, two key points should be taken into consideration. First, the low sufficient density of both AFM tip ligands and the cell surface receptors is crucial for successful events. Second, a crosslinker has to be used to connect the ligand to AFM tip to distinguish the specific from nonspecific bindings and to provide a flexible orientation to the ligand [43].

Control experiments

For controlling the force measurements, FD curves are recorded after incubating the cells sample in a solution of free ligands which is called blocking experiments. Consequently, the binding probability decreases, and this refers to the occupation of binding sites of receptors by the free ligands in the solution. For more confirmation, another control experiment can be done; the living cells are knocked out of the receptors' genes [44]. Then, the FD curves are obtained on the knocked-out cells using ligand-coated tips. Knocking out the receptors' genes dramatically reduces the number of detected recognition events. These control experiments confirm the specificity of receptor-ligand binding.

Rupture force measurements

To determine the specificity of the recognition interaction between the ligands and receptors, FD curves are recorded between the ligand-coated tip and the receptor at a certain retracting speed. The individual rupture force events are usually recorded over a selected cellular membrane area. The scanned area presents force-based map of the receptors' distribution while the average rupture force is revealed from a histogram of the total recorded events (Figure 13A, B). Rupture force measurement is considered as an indicator for the strength of the investigated molecular interactions. These values reflect the atomic chemical forces contributing to the bond [45]; therefore, another complementary assay is provided at the atomic level.

Imaging receptor's distribution

The AFM capabilities are not limited to only quantitatively describing the receptor-ligand interaction, but also to localize the receptors over the cell surface. Single-molecule force spectroscopy can be applied to locally identify the receptor-ligand binding on the living cell surface [38]. Detection and localization of receptors over the cell membrane provide insight into

the receptor's population level, distribution, and binding strength to its ligands, which are critical information for designing effective drugs, for example targeting integrin receptors on the cancer cells using cRGD ligands [46].

Receptor-ligand multiple interactions

As shown in previous sections of this chapter, the ligands can discriminate specific receptors among several receptors and molecules on the cell membrane. Also, the receptor-ligand binding can be quantified by applying SMFS experiments. Moreover, the receptors' coverage can be determined on cell surfaces. Thus, gaining this necessary information enables us to optimize the targeting affinity among single and multiple receptor-ligand binding to achieve binding selectivity among cells with different receptor expressions. Binding selectivity is enhanced with multiple bindings compared to single bindings.

The force measurements can be performed with higher ligands concentration on the AFM tip. Following the SMFS procedure, the force spectroscopy measurements with higher ligands density on the tip reveal the number of bonds that formed between receptors and ligands in the rupture events. Collecting data in the form of histogram helps to determine the single and multiple binding (Figure 13C). In this case, multiple gaussian fittings can be applied to multiple peaks on the histogram. Hence, the peak with lowest force value of each distribution corresponds to a single bond, while the higher corresponds to multiple bonds, double or triple bonds. Fulfilling multiple bindings (multivalency) enhances the binding affinity for the receptors and their ligands.

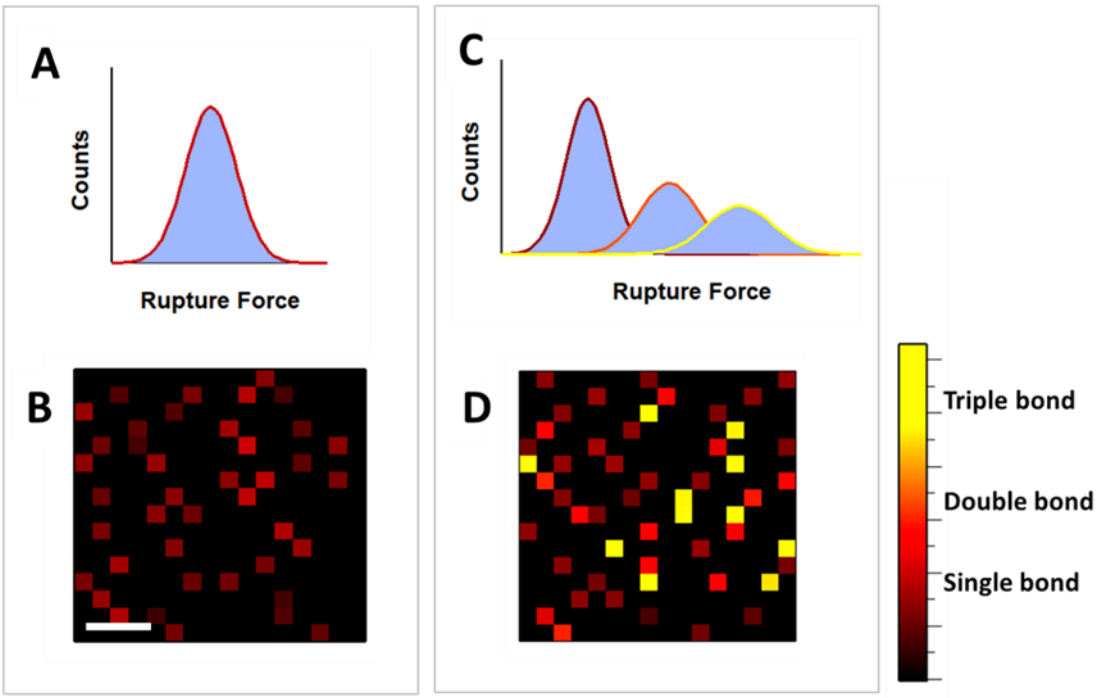

Figure 13. Representative diagrams for analyzing and presenting single and multiple receptor-ligand unbinding data. Rupture force measurements of single binding are represented as a histogram (A) corresponding to a map (B) of receptors' distribution with color scale revealing the rupture force magnitude. Controlling the ligands density of the tip, multiple binding can be formed, and the rupture force measurements distribution shows a histogram with multiple peaks (C) such as double and triple binding. The successful binding events on the map (D) demonstrate the number wise of bonds corresponding to a color scale of force magnitude. The blue color in the histograms represents the data. The scale bar in the map is usually 100 nm which is appropriate for the highest resolution used for detecting membrane receptors.

AFM-Tip Functionalization

The AFM probe can be chemically modified by attaching the ligands to the probe surface. Functionalizing the AFM tips leads to create sensitivity towards the targeted receptors on the cellular membrane. The ligands-coated AFM tip can then be used to quantify the receptor-ligand interactions or the distribution of the receptors over the cell surface. To prepare the AFM tips for SMFS measurements, the tips are cleaned first. Then, three subsequent steps are followed to functionalize the tips as described in the following sections.

Cleaning AFM tips

The AFM tips have to be cleaned prior to functionalization according to a well-known protocol [47]. First, the silicon nitride (Si_3N_4) tips are extensively washed with chloroform and dried with N_2. Then, the tips are washed with Piranha solution (H_2SO_4/30% H_2O_2, 7:3) or with nitric acid solution (10%) to remove any organic contaminants. Then, they are washed with deionized water and dried with N_2. This allows generating more hydroxyl groups on the tip surface which makes it ready for the next step.

Amino functionalization

AFM-tip functionalization process starts with coating the tip with amine groups which is done by incubating the tip in ethanolamine hydrochloride in dimethyl sulfoxide (DMSO) solution overnight at room temperature [48]. Using DMSO as a solvent instead of other polar solvents (e.g., ethanol) prevents forming long and sticky polymers which results in sticky AFM tip. The silicon nitride AFM tip interacts with ethanolamine HCl/DMSO using silanol groups (Si-OH) that are naturally formed on the tip surface in the ambient condition after cleaning the tip. Immersing the hydroxylated AFM tip in this solution leads to produce amino groups (NH_2) on the tip surface.

Attaching linkers to AFM tip

The second step of AFM tip functionalization is a crosslinker binding to the AFM tip. In receptor-ligand recognition experiments, it is necessary to use a flexible linker molecule to specify the binding of a certain membrane molecules from nonspecific tip-membrane adhesion [49]. The linker is attached to the tip surface first, then the targeting peptide is linked to the free end of the linker. Flexible polyethylene glycol (PEG) tethers have frequently been used as a linker because they are inert molecules and freely reorient. Also, PEG linkers can discriminate

specific interactions from non-specific probe-cell membrane adhesion due to their nonlinear stretching behavior.

Generally, PEG linker uses an N-hydroxysuccinimidyl (NHS) ester function on one end to bind with amino group coating the AFM tip. To achieve that, the amino-coated tip is incubated in the PEG-linker solution for 2-4 hours, resulting in forming stable amide bond between NHS (of the PEG linker) and the NH_2 group (on the AFM tip surface). Then, the tip is extensively washed in chloroform and dried with N_2. The PEG free end has a functional group that should covalently be able to bind to the ligand. PEG linkers can be synthesized with different functional groups depends on which ligand needs to be conjugated to.

Attaching ligand to a linker

Finally, the AFM tip with PEG linkers is incubated in a solution of the targeting peptide molecules. In chapter 5, we used cRGD peptide to detect the presence of α_v integrins on the living cell surface. PEG linker with Azido group on the free end was used where it covalently binds to the alkyne (hexynoic acid) moiety of the cRGD peptide by cycloaddition click chemistry.

Controlling ligand concentration on the AFM tip

The ligand density on the tip can be controlled to sufficiently low concentration by following well-established protocols [47]. To confirm that most of the recorded recognition events are single bindings, the density of ligands should guarantee 1 to 3 ligands per sufficient tip-sample contact area. The concentration of ligands can also be increased to achieve multiple interactions by increasing the linkers concentration.

Dynamics of Membrane Receptor-Ligand Interactions

Information on the receptor-ligand complex dissociation dynamics and bond energy barriers can be derived from the single molecule dynamic force spectrum of the receptor-ligand bond [37] [50]. Measuring the rupture force using AFM at a constant tip speed demonstrates only a single point in the bond strengths spectrum. When the AFM tip speed changes, dynamic spectrum of bond strengths appears.

As the force spectroscopy technique requires pulling the receptor-ligand bond during the measurement, it is indispensable to rely on the theoretical approach that describes the bond rupture under external force. In the absence of external force, the lifetime of a reversible bond is determined by the thermal energy of the surrounding. The lifetime is given by the inverse of off-rate constant as: $\tau(0) = k_{off}(0)^{-1}$. Applying an external force reduces the lifetime and as a result, the rupture force becomes measurable because of the bond resistance of detachment.

The theoretical framework for our system started with Kramers theory in 1940 [51]. Kramers model, the transition state theory, describes a Brownian particle escape from the bound state to the unbound state crossing an energy barrier of a 1-dimensional energy landscape. The model also shows that the external applied force, affecting the reaction rates of transition, lowers the energy barrier. In Kramers transition theory, the escaping is induced only by thermal fluctuations.

After that, the likelihood *p(t)* of the particle escape, between the two states in a potential *U(x)* at time *t* and coordination *x*, was described by Klein-Kramers' equation [51] [52]:

$$\frac{\partial}{\partial t}p(t) = \kappa(x, v, U(t)) \times p(t) \quad (1)$$

where κ is the rate of escape.

Later in 1978, Bell's model was introduced based on Kramers theory to describe the changed rate of bond dissociation under external forces for the first time [50]. In Bell's model, the off-rate constant is defined as the natural oscillation frequency w_0 times the likelihood of rupturing the bond under external force which is given as

$$k_{off}(F) = w_0 \times \exp\left[\frac{-(E_b - F.x_b)}{K_B T}\right] = k_{off}(0) \times exp\left[\frac{F.x_b}{K_B T}\right] \quad (2)$$

Where F is the external force, x_b is barrier width, and $K_B T$ is the thermal energy. Bell's model has a significant insight into studying the bond rupture induced by mechanical force, but all energy landscape features are packed in the reaction coordinate *x*. Bell's kinetic theory of bonds was applied for atoms in solid for the first time by Zhokov et al. [53]. Evans and Ritchie extended Bell's model in 1997 based on Kramers transition theory and introduced a model that describes bond rupture under an external force, taking into account the distributions of experimentally measured rupture forces that result from the stochastic nature of the bond rupture.

Starting from the first-order of the kinetic theory [52], the probability of breaking the bond in time interval *dt* is given by:

$$\frac{\partial p(t)}{\partial t} = -k_{off}(t) \times p(t) \quad (3)$$

Solving the differential equation (3), with substituting the off-rate from equation (2) resulting in a distribution formula of rupture forces in terms of loading rate (*df/dt*) [37] [54] as follows:

$$P(t, F) = k_{off}(F(t)) \times \exp\left[-\int_0^t k_{off}(T) dT\right] \quad (4)$$

In the elastic system of receptor-ligand binding, the applied force is linearly related to the time as $F(t) = k_{ef} \times v \times t = r \times t$, where k_{ef} is the effective elastic constant of the system, v

is the retracting speed of exerting force, and *r* is the rate of force change. The effective spring constant for the system is given by ($\frac{1}{K_{ef}} = \frac{1}{k_{sample}} + \frac{1}{k_{tip}}$).

In terms of the applied force, the probability distribution can then be written as a function of *F*, $P(F) = \frac{k_{off}(0)}{r} \times \exp\,[f(F)]$, and by applying the condition $\frac{dP(F)}{dF} = 0$, the most probable rupture force is given by [37]

$$F = \frac{K_B T}{x_B} \ln\left[\frac{r\,.\,x_B}{K_{off}(0).K_B T}\right] \tag{5}$$

The most probable rupture force *F* of the receptor-ligand bond is obtained by fitting the measurements taken from AFM-based force spectroscopy experiments, at a certain tip retracting speed, to a Gaussian distribution. Applying different speeds causes variation in the bond strength value, appearing weak or strong depending on how fast the force is loaded.

The dynamic force spectrum for receptor-ligand complex can be investigated using the force spectroscopy in a range that guarantees the cell safety. The speed of AFM tip is determined by changing AFM parameters prior performing the force measurements. Changing the AFM tip speed reveals the linear relationship between the average rupture force and the logarithm of force loading rate [37].

As the average rupture force of receptor-ligand bond increases logarithmically with the loading rate, the dissociation rate constant $K_{off}(0)$ and the energy barrier distance x_b can be extracted from the slope and the intercept of the fitted linear curve between force and logarithm of loading rate (equation 5). Only one linear regime is noticed in the force and logarithm of loading rate relation, indicating that the dissociation of the complex has to pass one energy barrier from bound state to unbound state.

CHAPTER 4. DYNAMIC CELLULAR BIOMECHANICS IN RESPONSES TO CHEMOTHERAPEUTIC DRUG IN HYPOXIA PROBED BY ATOMIC FORCE SPECTROSCOPY[1]

Introduction

Cell surface plays important roles in fundamental cellular functions such as signaling, communication, adhesion, transport, and tumor metastasis [13] [55] [56] [57]. The cell surfaces dynamically interact with physical, chemical, and biological environments surrounding cells and thus, alteration in cell's surface structure substantially influences overall cell functions [13] [58]. In particular, deformability of cells associated with cell shape, motility, and invasion has shown implications for cell death and cancer metastasis [59] [27], which is critical information for developing new anticancer drugs with increased efficacy in cancer chemotherapy [60] [61].

Chemotherapeutics rely on the release of anticancer drugs at tumor sites and the anticancer drug-induced cancer cell death, which has been well-understood biochemically [59]. While a number of studies have shown the relationship between chemotherapy-induced cell death [59] [62] and alteration in cellular mechanics such as stiffness [27], the impact of drugs on biomechanical and biophysical properties of cancer cells is not fully understood yet. Furthermore, stiffness at the tissue-level is significantly affected by the tumor stage, invasiveness, and location within the tumor due to the deposition of extracellular matrix, which influences the cellular behavior and metastatic capacity at the single-cell level as well [63] [64] [65] [66]. Nevertheless, cancer cells at the metastatic sites or during epithelial mesenchymal

[1] The material in this chapter was co-authored by Lina Alhalhooly, Babak Mamnoon, Jiha Kim, Sanku Mallik, and Yongki Choi. Lina Alhalhooly was primarily responsible for designing experiments, performing experiments, collecting data, analyzing data, and drawing conclusions from the results.

transition (EMT) have become softer and more deformable through substantial rearrangements in the cytoskeleton [67] [68].

One of the primary drivers of EMT and metastasis is hypoxia defined as the oxygen low - level environment. Hypoxia is the condition with oxygen low-level ranging from 0.3% to 4.2% oxygen in cell culture (2–32 mmHg), while normoxia is the condition of normal oxygen level in cell culture, approximately 20-21% oxygen (160 mmHg). Hypoxia can induce cytoskeletal injury and remodeling through the activation of the RhoA/ROCK signaling pathway by hypoxia-inducible factor-1α [63] [69] [70]. Using breast tumors, Plodinec et al. has shown the correlation between hypoxia and the softness of cancer cells [63]. However, it is unclear whether hypoxia is the solely responsible for cancer cell softening without taking into account the surrounding tumor microenvironment. Hypoxia is also known to be involved in drug resistance through changes in cellular metabolism, drug detoxification efficiency, and genetic instability [71].

Thus, further information on dynamics of cellular elasticity, morphology, and adhesion, and correlation between them following exposure to the drugs is a key to expanding our knowledge of the drug effects on cancer cell physiology and enhancing the chemotherapeutic potential of drugs [72]. Furthermore, investigation of hypoxia on the efficacy of chemotherapeutic drugs is of major interest among biological and biomedical fields because hypoxic condition appeared in almost all solid tumors and increases the cancer cell survival and resistance to chemotherapy, leading to poor clinical outcomes [73] [74].

A variety of biomechanical and biophysical assay approaches such as micropipette aspiration [19], optical and magnetic tweezers [20] [21], mechanical microplate stretcher [22], and atomic force microscopy (AFM) [75] have been used to assess the deformability of living cells. Among those, the AFM method has proven to be an ideal technique for investigating

nanoscale-resolution morphology and biomechanical properties of single cells in physiological solutions [13] [76] [24][1, 29, 30]. Furthermore, the functionalization of the AFM probe with selective ligands permits quantitative measurements of the structure and function of the intracellular components such as cytoskeleton, adhesion force and binding probability between membrane receptors and ligands [72]. Recently, the stiffness analysis of live metastatic cancer cells using the AFM method has demonstrated the applicability in distinguishing cancerous cells from normal ones [27]. Several studies using the AFM-based force measurements also have shown a significant change in cell stiffness with increasing metastatic efficiency in human cancer cell lines and chemotherapy exposure in leukemia cells [59].

In this chapter, we quantified the drug effects on the biomechanical and biophysical properties of four cancer cell lines: MDA-MB-231 triple negative breast cancer, PANC-1 pancreatic cancer, PC-3 prostate cancer, and U-118 MG glioblastoma cell lines. The AFM force techniques were applied to trace time-dependent changes in cellular morphology, elasticity, roughness, and adhesion after exposure to standard chemotherapeutic drugs for each of the cancer cells: gemcitabine forPANC-1, doxorubicin for MDA-MB-231, vincristine for U-118 MG, and mitoxantrone for PC-3. Comparison of such parameters in normoxia and hypoxia provides a fundamental understanding of the drug effect on cellular cytoskeletal structure and integrity and its dependence on the oxygen condition surrounding the microenvironment.

Materials and Experimental Methods

Cell culture

The MDA-MB-231 triple negative breast cancer, PANC-1 pancreatic cancer, PC-3 prostate cancer, and U-118 MG glioblastoma cell lines were purchased from American Type Culture Collection (ATCC, Manassas, VA). The cells were cultured in Dulbecco's Modified

Eagle Medium (DMEM) supplemented with 10% fetal bovine serum (Avantar Seradigm) and 1% v/v antibiotics (Penicillin, Streptomycin, Amphotericin B solution, Corning). All chemotherapy drugs including doxorubicin, gemcitabine, mitoxantrone, and vincristine were purchased from Sigma Aldrich. A humidified incubator containing 5% CO2 and 21% Oxygen at 37°C was used for normal incubation (normoxia), while for hypoxic condition a chamber supplemented with 2% oxygen and 5% CO2 at 37°C was used (Biospherix C21, Parish, NY).

Cell treatment

All cell lines were cultured in T25 cell culture flasks to reach 80–90% confluency. The cells were then trypsinized (Thermo Fisher Scientific), counted, and seeded (40,000 cells) in 35 mm glass bottom dishes (ibidi GmbH, Germany). The cells were incubated for 48 hours followed by the drug treatment. The MDA-MB-231, PANC-1, PC-3, and U-118 MG cells were treated with 5 μM doxorubicin, gemcitabine, mitoxantrone, and vincristine, respectively, for various times including 2, 4, 6, 8, 10, 12, 16, 18, and 24 hours under both hypoxic and normoxic conditions. The time intervals were determined based on the cell viability in each condition, which allows us to monitor a continuous change in biomechanical properties without missing any sudden change and determine time-dependent trends for them. At the end of treatment time points, the cells were washed with phosphate buffer saline (PBS) for 2 times and replenished with DMEM before AFM imaging and spectroscopy measurements. For cytochalasin D experiments, the PANC-1 cell line was seeded in the glass bottom dishes (40,000 cells per dish, 4 dishes for each cell line) and pre-incubated for 48 hours. The cells were then separately treated with 5 μM cytochalasin D (Cayman Chemical, Ann Arbor, MI) for 45 and 60 minutes under normoxia, and for 60 and 90 minutes under hypoxia. At the end of treatment time points, the

cells were washed with PBS for 2 times and replenished with DMEM before AFM measurements.

Cell viability

Each cell line was seeded in 96-well cell culture plates (5,000 cells per well) and incubated overnight. The cells were then treated with different concentrations of doxorubicin, mitoxantrone, vincristine, and gemcitabine ranging from 0.5 to 15 μM. The cells were washed 3 times with phosphate buffered saline after 12 and 24 hours. A mixture of the cell culture medium and Alamar Blue reagent (9:1 v/v ratio) was added into each well. After 5 hours, the fluorescence was measured with 560 and 595 nm excitation and emission wavelengths respectively, and the cell viability was calculated.

Fluorescence microscopy

The PANC-1 and MDA-MB-231 cells were seeded into 12-well cell culture plates (5,000 cells per well) and incubated in either normoxia or hypoxia for 48 hours. The MDA-MB-231 cells were then treated with 5 μM doxorubicin for 3 hours. Gemcitabine was loaded into nanocarriers composed of biocompatible and biodegradable polylactic acid (PLA) and polyethylene glycol (PEG) polymers, along with fluorescent lissamine-rhodamine dye, as previously described [77] [78]. Briefly, the PLA-PEG polymer and lissamine-rhodamine dye were mixed at a 95:5 molar ratio with 0.2 mg/ml gemcitabine solution. When the cells were treated with drug-loaded carriers for 3 hours, these carriers disintegrated and released gemcitabine. Due to the presence of fluorescent lissamine-rhodamine dye, the cells were identified under fluorescent microscopy. The PANC-1 cells were treated with 5 μM gemcitabine loaded into the nanocarriers for 3 hours. Subsequently, the cells were washed with PBS for three times. The nuclei of the cells were stained with Hoechst 33342 (NucBlue™, Invitrogen) dye.

Then, the cells were washed again with PBS for three times and a fluorescence microscope (Leica) was used for imaging.

Atomic force microscopy

The cell imaging and spectroscopy measurements were conducted using a commercial AFM (NT-MDT NTEGRA) with optical viewing system and V-shaped silicon nitride AFM probes with a spring constant of 0.08 N/m (Nanoworld) at room temperature. Cantilever spring was calibrated by the thermal noise fluctuation methods [79], and the deflection sensitivity of each tip was calibrated by force-distance curve measurements on the bare glass area of the petri dish. At least 5 cells at each condition were randomly selected for all imaging and other force measurements. To prevent the false measuring of already dying or dead cells due to the drug treatment, we excluded the cells that are loosely attached or floating. The scanning resolution was 256 × 256 pixels with a scan rate of 0.1–0.5 Hz, depending on the scanning areas of irregular cell size. The acquired images were flattened, if required, to eliminate the background noise and tilt from the surface using all unmasked portion of scan lines to calculate individual least-square fit polynomials for each line.

Stiffness and adhesion measurements

The FD curves were obtained on the central cytoplasmic region of cell surface. The approaching and retracting rates of probe were 1 μm/s for all measurements. Depending on the tip geometry (four-sided pyramid), the Young's modulus can be extracted using $F(\delta) = \left(\frac{E}{1-r^2}\frac{tan\alpha}{\sqrt{2}}\right)\delta^2$, where E is the Young's modulus, r is the Poisson's ratio, and α is the tip face angle. The Poisson's ratio of 0.5 for typical soft biological samples and the tip face angle of 35° were used. The mean Young's modulus was calculated by at least total 35 FD curves at each

time point, and the mean adhesion was obtained from a total of 60 adhesion measurements at each condition.

Surface roughness measurements

The analysis of the surface roughness of cells was carried out using the Image Analysis P9 software (NT-MDT) using acquired AFM images. The root-mean-square roughness *Rrms* was quantified, which was given by $R_{rms} = \sqrt{\frac{1}{N_x N_y}\sum_{j=1}^{N_y}\sum_{i=1}^{N_x} Z_{ij}^2}$, where $Z_{ij} = Z(x_i, y_i)$ is the height function defined over a rectangular area in the XY plane with a uniform grid of dimensions N_x and N_y and of steps Δx, Δy along the X and Y directions, respectively [80]. For each cell, at least five areas ($2.5 \times 2.5\ \mu m^2$) on the central flat region were selected and analyzed. The mean roughness was calculated by a total of 125 roughness measurements at each condition.

Statistical analysis

All data were expressed as mean ± standard deviation and analyzed using the Prism 8 (GraphPad software). The statistical significance was determined using analysis of variance followed by suitable post-hoc test. The *p*-values lower than 0.05 were considered statistically significant.

Results and Discussion

Measuring the biomechanical properties of four cancer cell lines

As explained earlier in the background chapter, the force-distance curves display the direct interaction between the tip and cell surface, which allows us to compare the elastic responses of each cell. Compared to the force-distance curve of PANC-1 cell, more force is required for U-118 MG cells to indent at the same depth ($d < 0$ nm), implying that the cell surface of U-118 MG is relatively stiffer than PANC-1. By fitting the non-linear region of the force-distance curve to the Hertz model (black curves in Figure 14), the relative cell stiffness

(Young's modulus, *E*) of individual cells was calculated (see the Background for more details) [27] [81] [82]. Given inhomogeneity of cells, the force-distance curves and the Young's modulus were collected by taking multiple indentation measurements at different locations over the central cytoplasmic regions of individual cells at the same indentation depth (400 nm).

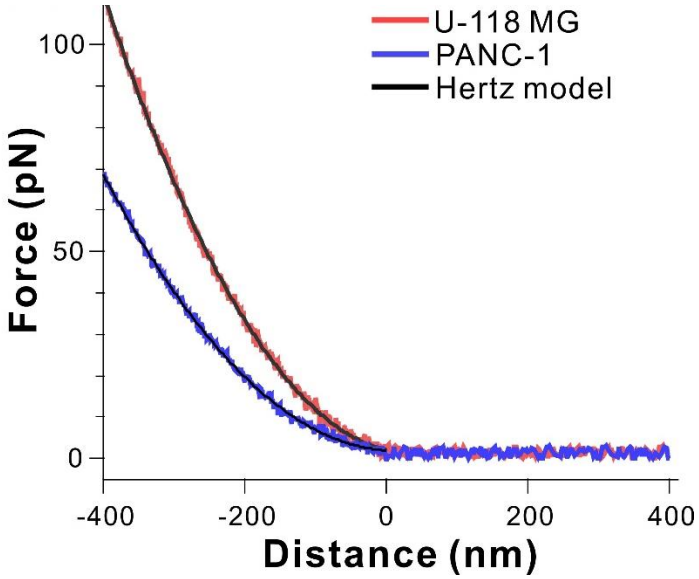

Figure 14. Typical FD curves recorded during approaching process between the cantilever and cell surface of U-118 MG (red) and PANC-1 (blue) cells, along with the Hertz model (black), which allows to determine Young's modulus E.

To evaluate distribution of the cell elasticity, a histogram of the Young's modulus was generated from 49 live PANC-1 cells, where 7 force-distance curves per cell were measured (Figure 15A). The histogram fits well to a Gaussian distribution, determining the mean *E* of 0.58 kPa with a standard deviation (s. d.) of 0.06 kPa. Figure 15B compares the stiffness of four cancer cells pre-cultured in the media for 48 hours under normal condition (normoxia). The mean *E* of the cancer cells examined in this work ranged from 0.58 to 0.95 kPa, which agrees with previously reported *E* values of the cancer cells [83] [84] [85] [86]. Such low *E* values across cancer cells indicate that the cells are easily deformable, potentially increasing adaptiveness to the environment and metastatic capacity.

The mean *E* values (mean ± s. d.) for U-118 MG, MDA-MB-231, PANC-1, and PC-3 cells were 0.95 ± 0.15 kPa, 0.61 ± 0.06 kPa, 0.58 ± 0.06 kPa, and 0.78 ± 0.11 kPa, respectively. These results suggest that U-118 MG and PC-3 cells are relatively stiffer than MDA-MB-231 and PANC-1 cells, while the stiffness of MDA-MB-231 and PANC-1 cells revealed no statistical differences ($P > 0.05$).

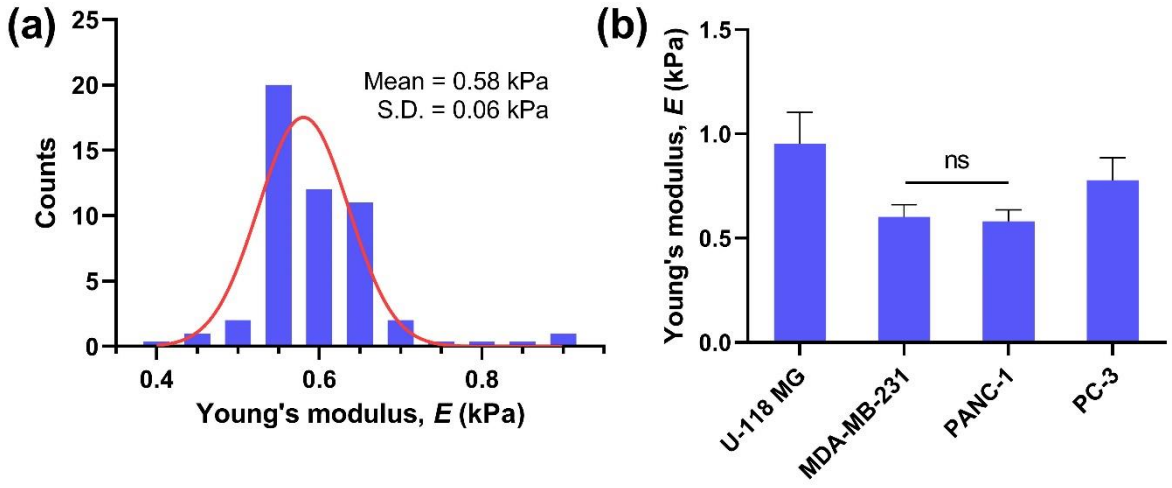

Figure 15. Young's modulus E for live cancer cells. (a) Histogram of E for PANC-1 cells (n = 49 cells; 7 force-distance measurements per cell) pre-incubated in normoxia for 48 hours and its fit to Gaussian distribution. (b) Comparison of Young's modulus E for four different cancer cells (U-118 MG, n = 9; MDA-MB-231, n = 10; PANC-1, n = 49; PC-3, n = 10; 7 force-distance measurements per cell) pre-incubated in normoxia for 48 hours. Data are mean ± s.d. ns, not significant by Student's t-test.

Time-dependent elasticity measurements under drug treatment in normoxia and hypoxia

After initial assessments of cell stiffness, stiffness kinetics following exposure to chemotherapeutic drugs were examined under two oxygen abundancy-dependent conditions: normoxia and hypoxia. The measured *Et* values for each time point were converted to a normalized *E* (= *Et*/*Et*=0) using the *Et*=0 values in Figure 15B, in order to compare relative changes in *E*. Each cancer cell line was pre-cultured in the media for 48 hours under normoxic condition prior to time-dependent experiments.

Brain cancer cell line

In control measurements performed in normoxia (Figure 16, blue curve) and hypoxia (Figure 16, green curve), the stiffness of U-118 MG (brain cancer cell line) cells exhibited little or no changes in both conditions during 24 hours of measurements. The linear regression analysis to both measurements revealed that trends of *E* values were not significantly different ($P > 0.05$). These observations indicate no significant changes in the cell stiffness during 24 hours of additional culture in hypoxic condition after 48 hours of pre-culture in normoxia. Considering the inherent hypoxic tumor microenvironment of glioblastoma [87], cancer cells are expected to be adapted to the hypoxic culture condition, and thus, no significant changes were recorded in biomechanical properties.

Following exposure to the chemotherapeutic drug vincristine, the stiffness of U-118 MG cells was significantly decreased in a time-dependent manner for both normoxia and hypoxia. The *E* value began to slowly decrease within the first 4 hours of exposure, and then rapidly dropped to ~42% of the initial *E* value until 10–12 hours of exposure in normoxia (Figure 16, red curve).

After 12 hours of drug treatment, the mean *E* and one standard deviation were 0.40 and 0.13 kPa, respectively.

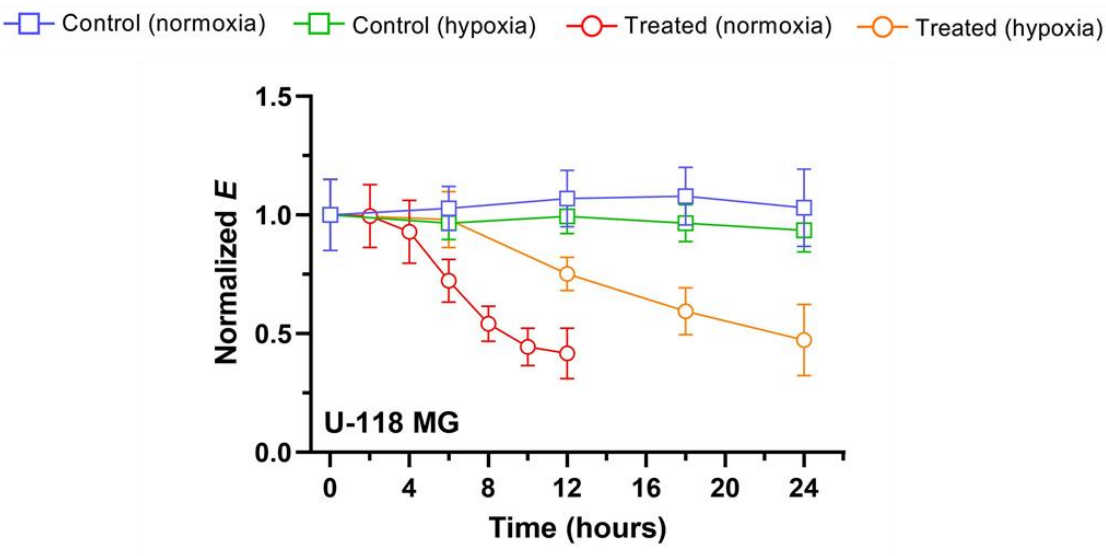

Figure 16. Time trace of normalized Young's modulus E in normoxia and hypoxia. The blue and green square represent the normalized E of untreated, control cells of U118 MG in normoxia (n = 5) and hypoxia (n = 5), respectively. The red and orange represent the normalized E of U-118 MG cell exposed to vincristine in normoxia (n = 5) and hypoxia (n = 5), respectively. Data are mean ± s.d.

While a similar trend of *E* was observed in hypoxia after vincristine treatments, the overall decrease was slower and gradual over 24 hours of exposure time (Figure 16, orange curve). When cells were treated in hypoxia, it took twice as long to reach the lowest *E* value (~ 0.45 kPa) compared to cells treated in normoxia.

The chemotherapeutic drug vincristine is a potent microtubule-destabilizing agent and widely used to treat several types of cancers [88] [89]. The disruption of microtubules leads to reorganization of cytoskeletal structures and change in the cell integrity. Previous research has shown that, due to the depolymerization of cytoskeleton, the stiffness of several cancer cells and peripheral sensory neurons decreases and becomes more elastic after treating them with vincristine [90], which is consistent with our observation of significant changes in vincristine-treated cell stiffness. Interestingly, our data show that the stiffness changes are much slower in hypoxic condition. This result suggests that hypoxia could contribute to drug resistance by delaying the biomechanical dysregulation process induced by the drug.

Breast, pancreatic, and prostate cancer cell lines

To further investigate the relationship between a chemotherapeutic drug-induced change in stiffness and cancer type, three additional cancer cells were examined: breast, pancreatic, and prostate cancer cell lines. The time-traced, control measurements of stiffness for three cancer cells in normoxia and hypoxia were analogous to those obtained with U-118 MG cells (Figure 17–18). These results suggest hypoxia itself has no significant effect on the biomechanical structure of cancer cells. Next, each cell line was exposed to standard chemotherapeutic drugs including doxorubicin (MDA-MB-231), gemcitabine (PANC-1), and mitoxantrone (PC-3), and traced in normoxia and hypoxia by serial, single-cell stiffness measurements over 12–24 hours. In case of MDA-MB-231 and PANC-1, the *E* values were significantly decreased upon exposure to the drugs in time-dependent fashion.

In normoxia, both cells became approximately 14–18% less stiff after every 2 hours of exposure and reached the lowest *E* values of 0.15–0.25 kPa within 12 hours of exposure. While the stiffness of both treated cells was reduced in a time-dependent manner in hypoxia, the decreasing rate of *E* was approximately 30–36% lower than in normoxia. Although the rates are slightly different for each cell, the overall changes in stiffness of three cancer cells (U-118 MG, MDA-MB-231, and PANC-1) in hypoxia were consistent with exposure to the chemotherapeutic drugs and their exposure time.

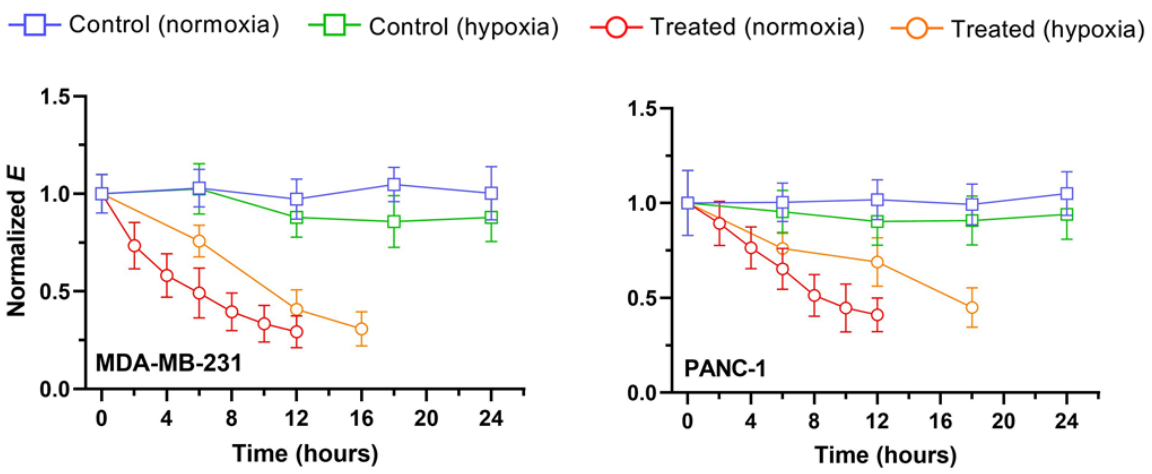

Figure 17. Time trace of normalized Young's modulus E after exposure to 5 μM drugs in normoxia and hypoxia. The blue and green square represent the normalized E of untreated, control cells of MDA-MB-231(a) and PANC-1(b) in normoxia (n = 5 per cell line) and hypoxia (n = 5 per cell line), respectively. The red and orange represent the normalized E of MDA-MB-231 cell exposed to doxorubicin and PANC-1 exposed to gemcitabine in normoxia (n = 5 per cell line) and hypoxia (n = 5 per cell line), respectively. Data are mean ± s.d.

Similar to vincristine, doxorubicin and gemcitabine are two of most effective chemotherapy drugs for several cancer treatments. While both drugs are well known to inhibit DNA synthesis [89] [91], a number of action mechanisms have been proposed for drug-mediated cell deaths. For example, doxorubicin was shown to intercalate nucleic acids and participate in depolymerization of actin filaments, destabilization of cytoskeletal structures, thus reducing the biomechanical strength of a cell, such as stiffness [92] [80]. A significant decrease of Young's modulus and a change in cellular morphology of lung cancer cells treated by methotrexate, classified as an antimetabolite like gemcitabine, were also previously reported [93]. Thus, our observations of the reduced stiffness of MDA-MB-231 and PNAC-1 cells following exposure to drugs demonstrate that these types of chemotherapeutic drugs eventually induce disruption of cytoskeletal structure by either direct or indirect interaction with cytoskeletal components. Furthermore, our results from elastic measurements of all cancer cells in hypoxia indicate that the cancer cells adapt to hypoxic microenvironment and become more resistant to the drug.

Interestingly, PC-3 cells exhibited a reversed trend: the stiffness of PC-3 cells began to increase after exposure to the chemotherapeutic drug mitoxantrone (Figure 18). In normoxia, cell stiffness increased significantly after 6 hours of treatment and reached a two-fold increase by 12 hours. Similarly, cell stiffness increased in hypoxia in a time-dependent manner, except stiffening took nearly twice longer compared to normoxia.

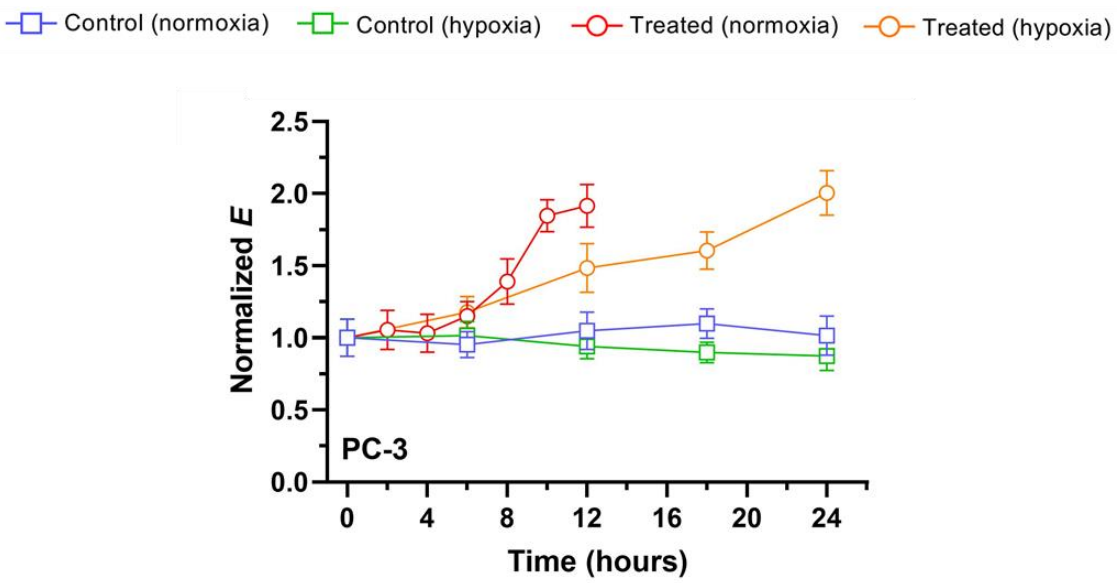

Figure 18. Time trace of normalized Young's modulus E in normoxia and hypoxia. The blue and green square represent the normalized E of untreated, control cells of PC-3 in normoxia (n = 5) and hypoxia (n = 5), respectively. The red and orange represent the normalized E of PC-3 cells exposed to mitoxantrone in normoxia (n = 5) and hypoxia (n = 5), respectively. Data are mean ± s.d.

Note that PC-3 cells treated with mitoxantrone for 12 hours in normoxia and 24 hours in hypoxia were loosely attached on the substrate, or completely detached from the substrate and floating, which limited further evaluation of the cell stiffness beyond this time point. While the drug treatment exerted the opposite effect on cellular stiffness in the case of PC-3 cells, hypoxia played a similar role in attenuating changes of the biomechanical property of cells upon drug treatment.

Like other chemotherapeutic drugs, mitoxantrone targets an enzyme to mediate DNA damage. This drug interferes with the action of DNA topoisomerase II associated with many DNA metabolic events such as transcription and replication [94].

Despite the similarity in the action mechanism of doxorubicin and mitoxantrone, the reverse results from stiffness measurements with PC-3 cells following treatment with mitoxantrone suggest that mitoxantrone induces further polymerization of cytoskeletal filaments and thus increases cell stiffness. Similar findings have been previously reported; antitumor antibiotic topotecan treatments with several patient metastatic tumor cells led to an increase in stiffness [95] and treating leukemia cells with either dexamethasone or daunorubicin resulted in increased cell stiffness by nearly two orders of magnitude [59]. Thus, drug-induced biomechanical reinforcement could be dependent on the type of cancer cells and chemotherapeutic drugs, though the underlying mechanism is unclear.

Drug-dose and treatment time optimization

The optimal dose and time of drug treatment associated with a change in the cell's stiffness was determined by our dose-response curves with viability for each cell line (Figure 19). Half-maximal inhibitory concentration (IC50) was calculated for each cell line where the cells were treated with different drug concentrations as shown in Figure 16−18, indicating the drug efficacy in timely manner. Using the cellular viability values, we were able to determine the time range of drug exposure for our measurements.

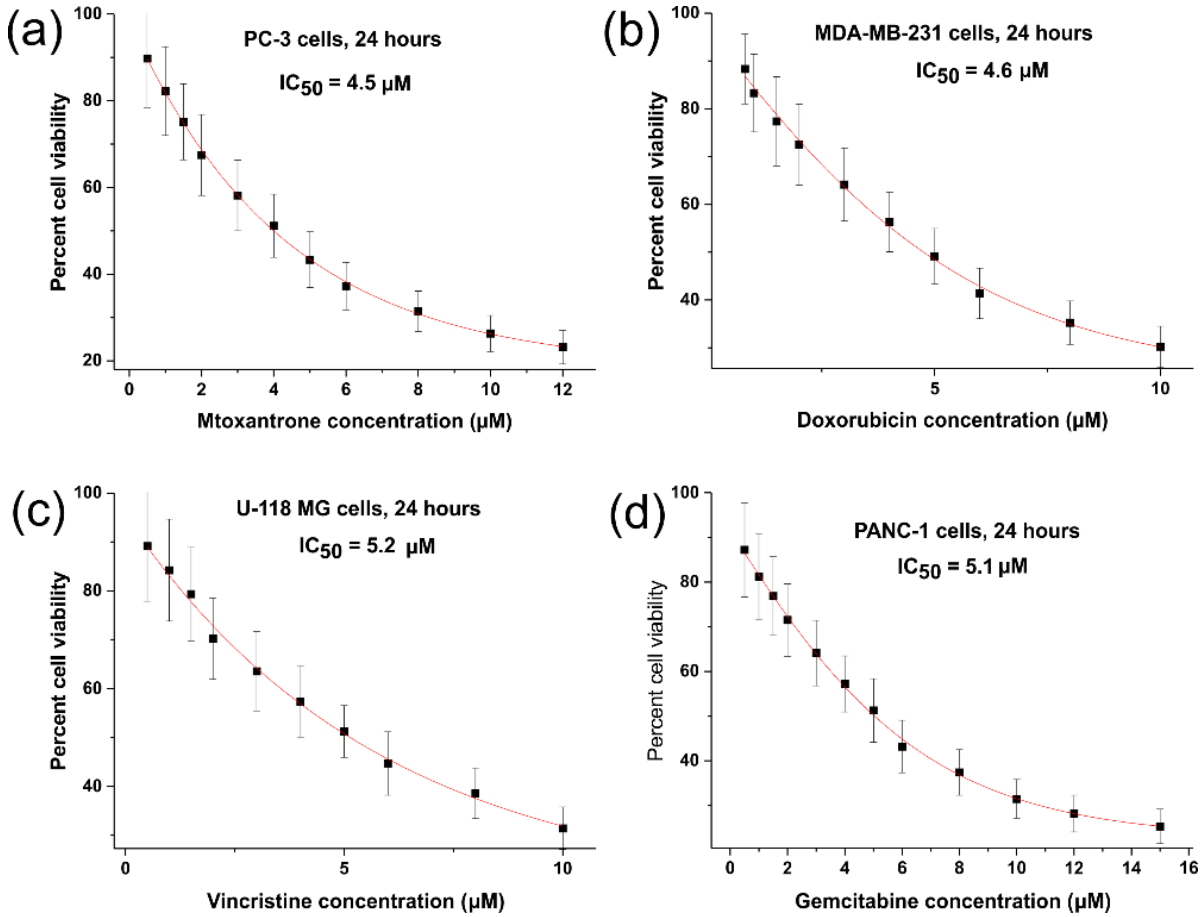

Figure 19. Viability of (a) PC-3, (b) MDA-MB-231, (c) U118 MG, and (d) PANC-1 cells treated with mitoxantrone, doxorubicin, vincristine, and gemcitabine, respectively for 24 hours.

Accordingly, the majority of treated cells underwent deformation after 12 hours in normoxia, which can be seen as a small, rounded shape of cells either loosely attached on the substrate or completely detached from the substrate (Figure 20).

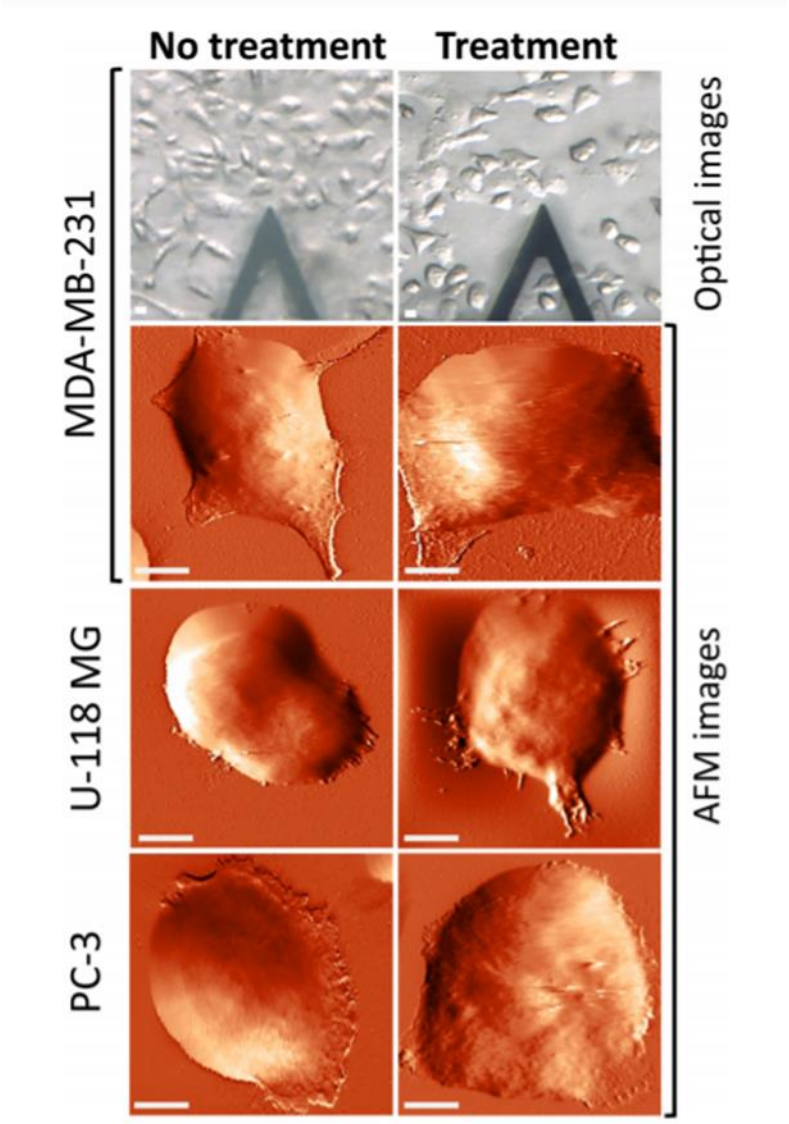

Figure 20. Optical images of MDA-MB-231 cells before and after 12 hours of exposure to doxorubicin in normoxia beside AFM images for MDA-MB-231, U-118 MG, and PC-3 cells before and after 12 hours of treatment in normoxia. The scale bars are 20 µm.

Also, the central cytoplasmic region of cells was not identifiable due to the changes in cellular morphology after 12 hours of treatment, further limiting the evaluation of cell stiffness beyond this time point.

Biochemical and metabolic alteration of hypoxia on the cellular cytoskeleton

Hypoxia induces the gene expression patterns through hypoxia-inducible transcription factors and activates the expression of numerous hypoxia-response genes including cell

adhesion, extracellular matrix, and cytoskeleton [96] [97]. For example, hypoxia influences expression and activation of Rho guanosine triphosphatases, which plays an important role in the regulation of the actin cytoskeleton [98]. However, dynamics and quantification of cytoskeletal changes are complex and differ from cells to cells. Furthermore, the interplay between hypoxia and chemotherapeutic treatments remains unclear. Our observations (Figure 16 – 18) suggest that drug-induced cytotoxicity could stimulate and accelerate such hypoxic effects on cytoskeletal regulation, leading to a gradual change in the stiffness.

Hypoxia itself, on the other hand, induced little change to stiffness in the absence of drugs, suggesting that either biochemical or metabolic processes associated with hypoxia could be a slow process. Otherwise, the interplay between hypoxia and microenvironmental factors including drug-induced cytotoxicity might be a key to activating and accelerating the processes. In addition, several studies have shown that tumor tissues are considerably more rigid compared to the normal tissue due to the stiffening of the peripheral tumor stroma [65] [66]. Thus, the stiffness of individual cancer cells determined by the changes of intracellular cytoskeletal structure may not be directly reflected in the overall stiffness of tridimensional tumor tissue, which relays on the alteration of the tumor stroma, rather than cancer cells [63].

Morphological changes due to drug treatment in normoxia and hypoxia

To examine the relationship between cell biomechanics and cell structures induced by chemotherapeutic drugs, the morphological changes of cancer cells were also investigated. Two parameters including cell body height and roughness were quantified and compared for individual cells before and after drug exposure for 12 hours in normoxia and 16–24 hours in hypoxia. The representative AFM images of control and treated PANC-1 cell display significant morphological changes after chemotherapeutic drug exposure (Figure 21).

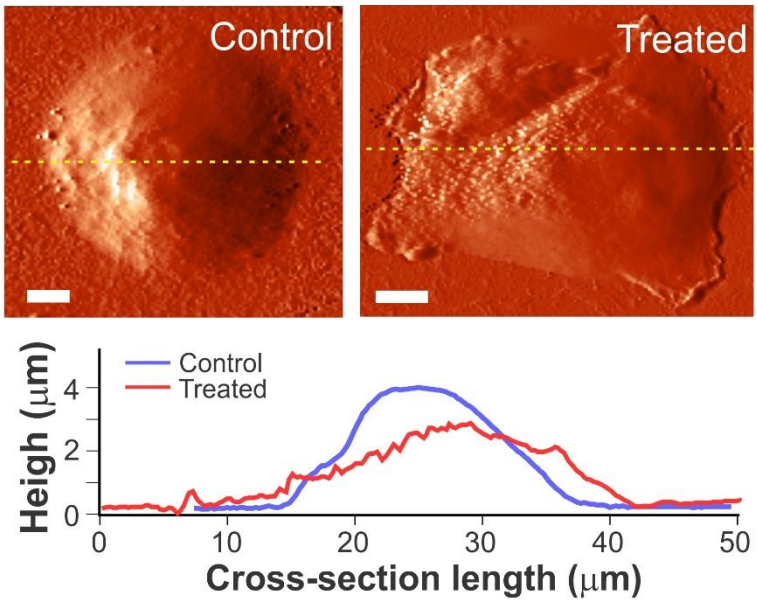

Figure 21. The drug-induced morphological alteration in cancer cells. An example deflection image of a live PANC-1 cell before (left) and after (right) gemcitabine treatment for 12 hours under normoxia. The scale bar is 5 μm. The cross-section analysis (yellow lines in the AFM images) shows changes in cell body height and roughness.

First, the cross sectional analysis of AFM images along the central cytoplasmic region of the cell revealed that the cell body decreases in height after exposure to drugs for U-118 MG, PANC-1, and MDA-MB-231 cells (Figure 22A). The apparent height was reduced by 13–25% from the initial height in both normoxia and hypoxia, but the changes in cell body height were indistinguishable between normoxia and hypoxia ($P > 0.05$). These results are consistent with stiffness changes for those cells, reflecting that the alteration in cell morphology is coupled with disruption of the cytoskeleton structure induced by drug treatments. Second, the roughness of individual cells was analyzed before and after treatments (Figure 22B), which is a sensitive measure of the structure and integrity of membrane-cytoskeleton interface [99]. The root-mean-squared roughness of those cells after exposure to chemotherapeutic drugs was increased by 39–75% as compared to non-treated cells. These observations imply that the structure of the cell's surface became less homogeneous and lost its structural integrity because of the

depolymerization of cytoskeletal filaments associated with drug-induced cell death process [90] [100] [101].

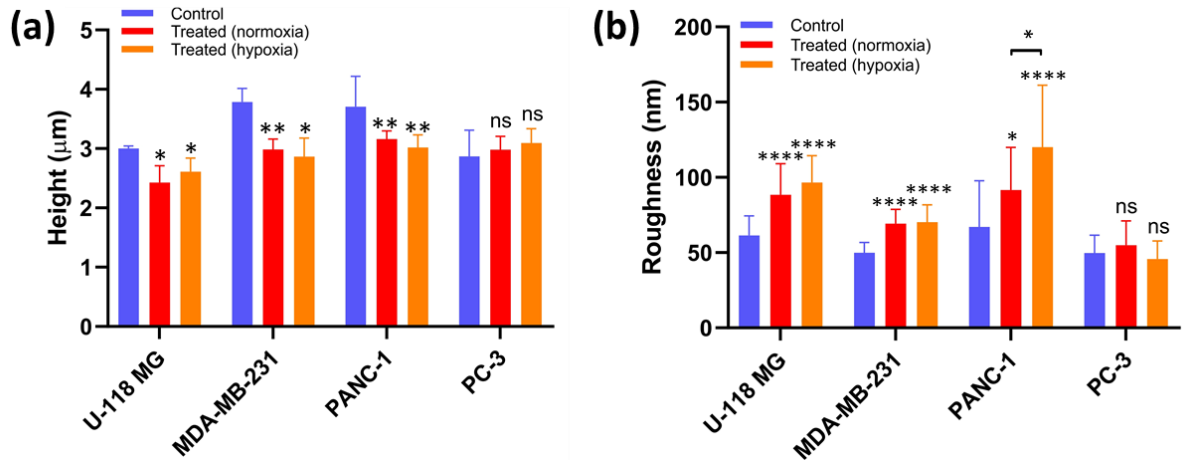

Figure 22. Alteration in (a) apparent cell height above the cytoplasmic region (n = 5 per group), and (b) surface roughness obtained from non-curved region of cell image (n = 5 per group). Data are mean ± s.d. The mean height and roughness of treated cells in normoxia and hypoxia were significantly different from that of untreated control cells ($P < 0.05$ by ANOVA) except as otherwise indicated by ns (not significant by ANOVA).

Despite the substantial increase in stiffness of PC-3 cells after mitoxantrone treatments, no significant change in cell body height and roughness of cell surface was observed in neither normoxia nor hypoxia following exposure to the drug. As might be expected, the reinforcement of cytoskeletal structure does not appear to alter the apparent cell morphology.

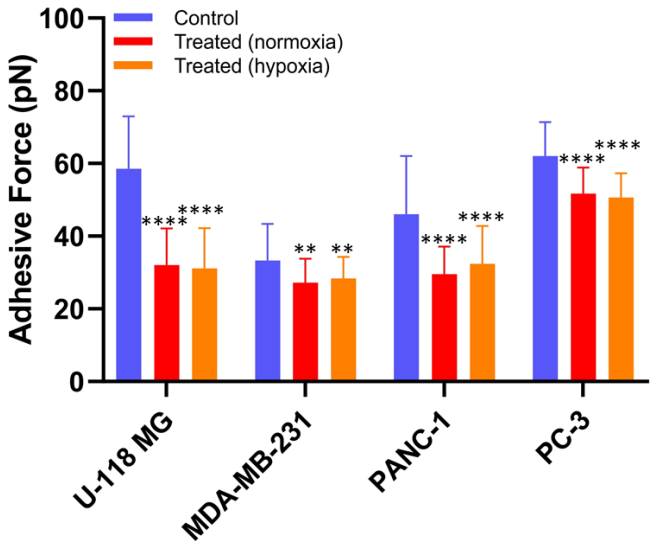

Figure 23. Non-specific adhesion (n = 6 per group) between the AFM probe and cell surface before (blue) and after exposure to the drugs in normoxia for 12 hours (red) and hypoxia for 16 - 24 hours (orange). Data are mean ± s.d. The mean adhesive force of treated cells in normoxia and hypoxia were significantly different from that of untreated control cells ($P < 0.05$ by ANOVA) except as otherwise indicated by ns (not significant by ANOVA).

In addition to apparent changes in cell morphology, variations of cell surface adhesion were examined to understand the relationship between cellular elasticity and adhesive force. The adhesion force spectroscopy between the AFM cantilever tip and the cell surface was recorded while retracting the tip from cell after reaching the target indentation depth of 400 nm (Figure 24).

Like morphology measurements, the three cancer cells (U-118 MG, MDA-MB-231, and PANC-1) exposed to the drugs exhibited a significant decrease in non-specific adhesion between tip and cell surface in both normoxia and hypoxia (Figure 23). Such changes are attributed to alterations in adhesive membrane molecules associated with degradation of the cytoskeletal structure induced by the drugs [102]. Therefore, these cells ultimately lose adhesion completely and are separated from the substrate, making them more round and a balled-up shape was observed in microscopic images (Figure 20).

Notably, the adhesion analysis for PC-3 cells also exhibited reduced cellular adhesion when exposed to mitoxantrone, which could be due to down-regulation in expression of the cell signal molecules and disruption of focal adhesion during the cell death process [103]. These results suggest that adhesion is independent of type of cancer cells and drugs, and it could be considered as an indicator of drug-induced apoptotic cell death.

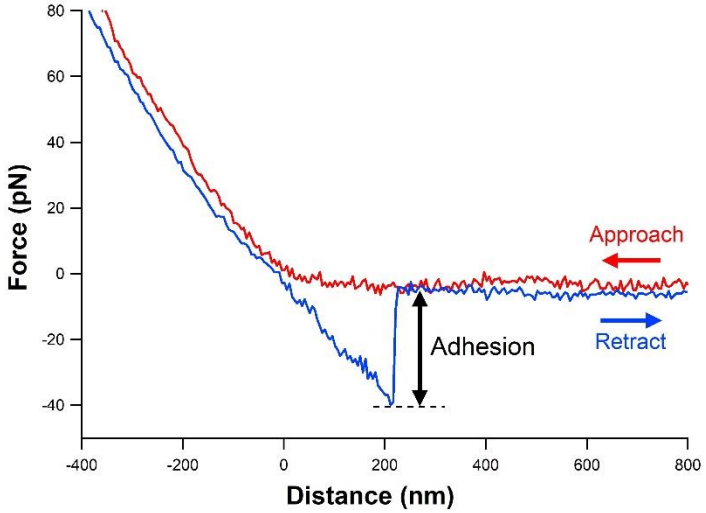

Figure 24. An example of FD curve obtained from the PANC-1 cell, showing approach (red) and retract (blue) curve. When the tip is retracted from the cell surface, adhesion events take place as shown a sawtooth-like shape. The adhesion force was determined as difference between force values at zero-force line of the FD curve and at the negative minimum of the FD curve (black arrow).

Experimental control

Cellular uptake effectiveness of drug in normoxia and hyoxia

To rule out the possibility that attenuated cellular response to the drug in hypoxia is due to less efficient drug delivery into the cells, we investigated the amount of drug uptake by cells in normoxia and hypoxia (Figure 25). Intrinsically fluorescent doxorubicin [104] [105] and gemcitabine loaded into lissamine rhodamine nanocarriers were used for the detection of drugs using fluorescence microscopy (see “Materials and Methods” for more details) [77] [78]. After 3 hours of drug treatment, nuclear localization of drugs was observed. In both cell lines, more than

95% of the cells treated with drugs showed fluorescence localized within the nucleus (Figure 25), indicating oxygen levels did not affect the drug uptake. Considering that there was no difference in cell stiffness between normoxia and hypoxia without drug treatments, the milder stiffness change is likely due to the specific interaction of drugs with DNA and cytoskeletal components in hypoxia.

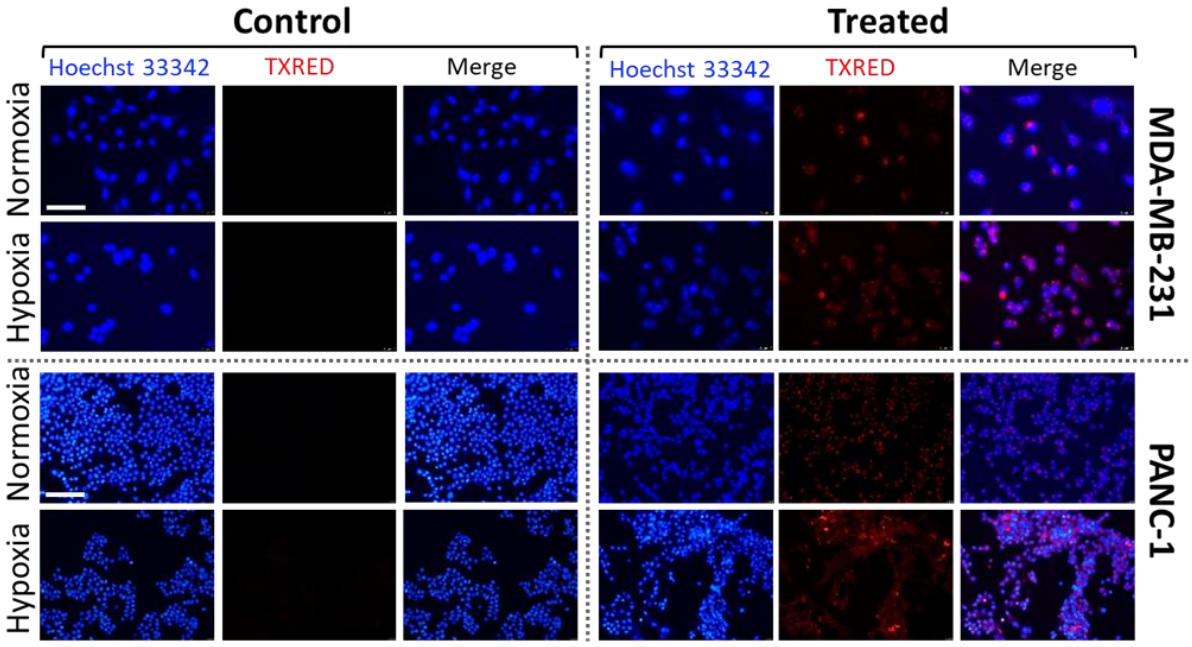

Figure 25. Drug uptake efficiency in normoxic and hypoxic conditions. MDA-MB-231 and PANC-1 cells were treated with doxorubicin and gemcitabine for 3 hours, respectively. Both drugs are detected by Texas Red (TXRED) filter using a fluorescence microscope. Nuclear localization of the drugs is confirmed by colocalization with Hoechst 33342. Scale bar (50 μm for MDA-MB-231 and 100 μm for PANC-1) is applied to all images.

Biomechanical and morphological alterations in response to cytoD drug in normoxia and hypoxia

Finally, we have examined changes in biomechanical parameters of cancer cells exposed to an inhibitor of actin polymerization cytochalasin D in normoxia and hypoxia [106]. The PANC-1 cells became less stiff under increasing duration of exposure to cytochalasin D, and the decrease of stiffness was slower in hypoxia than normoxia (Figure 26).

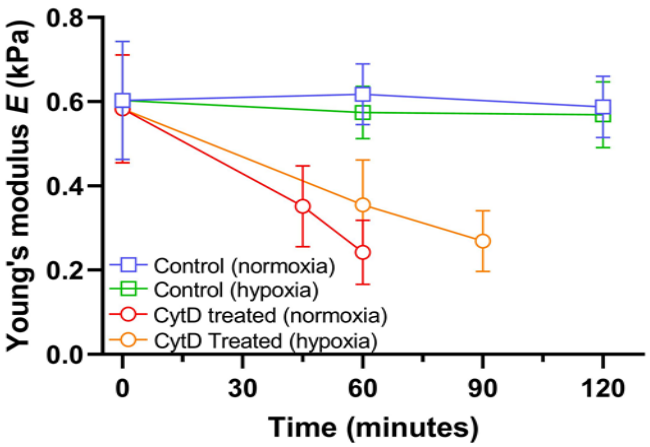

Figure 26. Alteration in biomechanical properties of PANC-1 cells exposed to 5 µM cytochalasin D (CytD) in normoxia and hypoxia. Time trace of Young's modulus E in normoxia (n = 5) and hypoxia (n = 5) after exposure to cytochalasin D.

Also, morphology and non-specific binding force measurements of the cells exposed to cytochalasin D showed a reduction in cell height and cellular adhesion, but an increase in cellular roughness (Figure 27).

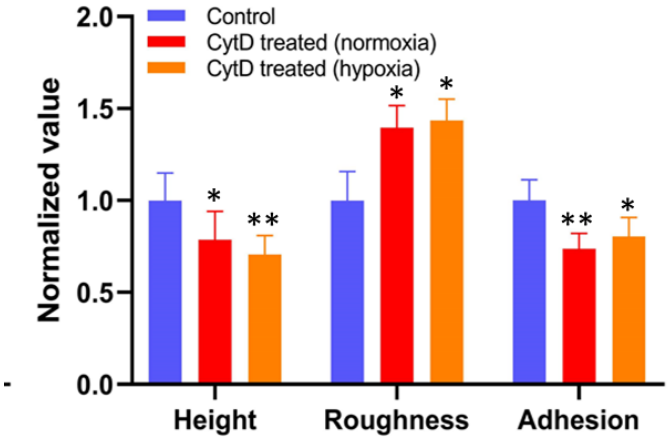

Figure 27. Normalized values of cellular height, roughness, and adhesion measured after exposure to cytochalasin D in normoxia for 60 minutes (n = 5) and hypoxia for 90 minutes (n = 5). Data are mean ± s.d. The mean height, roughness, and adhesive force of treated cells in normoxia and hypoxia were significantly different from that of untreated control cells ($P < 0.05$ by ANOVA).

Similar changes in biomechanical properties of MDA-MB-231 cells treated with chemotherapeutic drugs and cytochalasin D suggest that the drug-induced cytotoxicity is partly due to dynamic changes in the cytoskeletal structure (Figure 28) [107] [108].

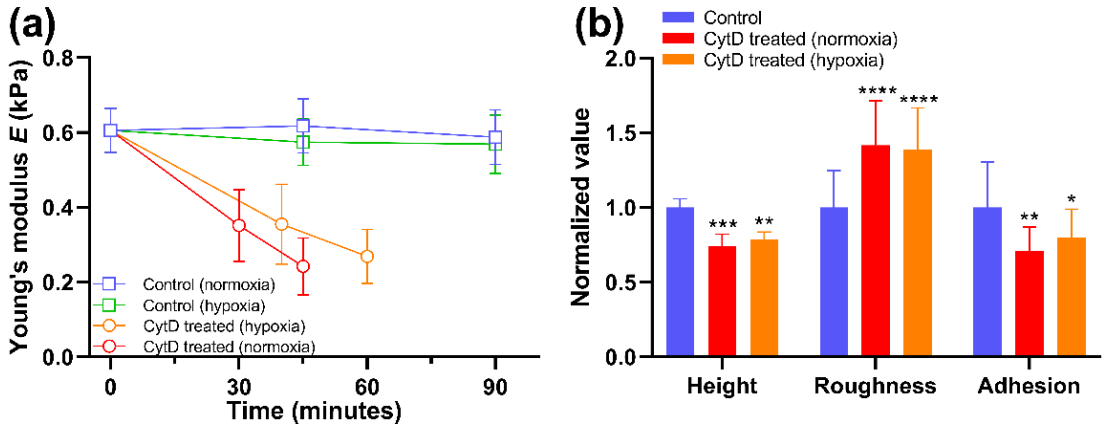

Figure 28. Alteration in biomechanical properties of MDA-MB-231 cells exposed to 5 µM cytochalasin D (CytD) in normoxia and hypoxia. (a) Time trace of Young's modulus E in normoxia (n = 5) and hypoxia (n = 5) after exposure to cytochalasin D. (b) Normalized values of cellular height, roughness, and adhesion measured after exposure to cytochalasin D in normoxia for 60 minutes (n = 5) and hypoxia for 90 minutes (n = 5). Data are mean ± s.d., ns, *, $P < 0.05$; **, $P < 0.01$; ***, $P < 0.001$; ****, $P < 0.0001$ by ANOVA. Statistics between normoxia and hypoxia showed no statistical difference (ns).

Also, hypoxia attenuated the cytoskeletal changes, which might contribute to drug resistance in the context of the tumor microenvironment. Although it is difficult to generalize drug effects on biomechanical and biophysical parameters of cancer cells, a combination of these parameters could help identify and distinguish the drug-induced apoptotic process in normoxia and hypoxia.

CHAPTER 5. MULTIVALENT INTERACTION BETWEEN cRGD AND α_v-INTEGRIN ON PANREATIC CANCER CELLS PROBED BY SINGLE MOLECULE FORCE SPECTROSCOPY[2]

Introduction

Cancer cells activate particular signals to regulate deformability of cytoskeleton structure during epithelial mesenchymal transition for tumor invasion, progression, metastatic expansion [109]. Recent studies of cellular biomechanics have demonstrated the remarkable difference in biomechanical properties (e.g., stiffness, morphology, roughness, adhesion) between normal and cancer cells, as well as their response to the chemotherapy drugs in hypoxia [110]. In addition, cancer cells elevate the expression of membrane proteins and receptors for amplifying cell-to-cell signaling and cell-to-extracellular matrix (ECM) adhesion [111] [112]. Thus, the distinct expression patterns and levels of plasma membrane proteins have been identified one of the most promising biomarkers for cancer diagnosis and attractive candidates for membrane-targeted anticancer drug development and delivery [113].

Integrins are heterodimeric, transmembrane adhesion proteins and mainly involve interactions to other cells and ECM. By regulating expression and activity of integrins, tumor cells control affinity to their environment and increase their migration, invasion, proliferation, and survival implicated in tumor progression and metastasis [114]. Although two subunits of integrins, 18 alpha and 8 beta subunits for human [115], offer a variety of heterodimer combinations (e.g., $\alpha_1\beta_1$, $\alpha_2\beta_1$, $\alpha_V\beta_1$), multiple integrins adhere to common ECM component such

[2] The material in this chapter was co-authored by Lina Alhalhooly, Matthew Confeld, Babak Mamnoon, Sanku Mallik, Yongki Choi. Lina Alhalhooly was primarily responsible for designing experiments, performing experiments, collecting data, analyzing data, and drawing conclusions from the results.

as fibronectin and laminin at the interface between them because of the ligand specificity of α subunit. In particular, a short amino acid sequence of cyclic arginine-glycine-aspartic acid (cRGD) motif is recognized as a common integrin-binding motif on target ligands [114].

Recent integrin studies have revealed that the integrin expression patterns and profiles are closely correlated with metastatic propensity of tumors [116]. For example, distinct expression of integrin α_v, along with its binding partners β_3 and β_5, was found in exosomes isolated from pancreatic cancer cell lines that metastasize primarily to liver [117]. For this reason, cRGD-based strategies to target integrin α_V heterodimers have been extensively studied for cancer therapy, imaging, and diagnosis: nanocarriers grafted with cRGD peptide have proven advantageous in delivering anticancer drugs, peptides, proteins, nucleic acids, and irradiation [118]. Although many cRGD-nanocarriers have demonstrated the successful tumor targeted delivery, more progress requires to be translated from a large number of preclinical studies of nanomedicine field. One effort must be a better understanding of molecular interactions principles between cRGD and integrin, which provides quantitative information about binding selectivity and affinity and help design more effective and enhanced carrier materials and structure.

Atomic force microscopy (AFM)-based, force measurements have been widely applied to probe and quantify intermolecular recognition and dynamic interactions between cRGD and several integrin receptors. The functionalization of the AFM probe with either the cRGD ligand or cells allowed quantitative measurements of binding probability between the ligand and its receptor on cell membrane, as well as force mapping of receptors distribution on the cell surface. For example, direct force measurements of the interactions between the integrin $\alpha_5\beta_1$ and RGD containing fibronectin fragment were acquired by attaching cells to the AFM probe, results from

which agreed with the force measurements performed with RGD ligand-integrin $\alpha_5\beta_1$ on biomimetic, artificial membrane system [119]. Direct measurements on debonding force between the RGD peptide and human platelet integrin $\alpha_{IIb}\beta_3$ receptors have been also studied [120]. From force-distance spectra analysis, single ligand-receptor force and the dissociation off-rate in the absence of the external force were estimated to be ~ 93 pN at a loading rate of 12 nN/s and 33.5 – 0.012 s^{-1}, respectively. However, dynamic interactions between cRGD ligand and α_v integrins on live cell membranes at a single-molecule level have not been well explored, which is a critical to enhance binding specificity and affinity for the development of rapid and sensitive integrin-targeted chemotherapy.

In this work, we quantified the unbinding force between cRGD-peptides and integrin α_v at single-bond resolution and compared the force map of integrin distribution on three human pancreatic cancer cell lines: PANC-1, BxPC-3, and MIA PaCa-2. By varying loading rates, the dissociation off rates of the ligand-receptor bond and the change in Gibbs free energy between bound and the transition state (energy barrier) in the presence and absence of the external force were examined. Furthermore, multivalent effects (multiple bindings of receptor-ligand interactions) of the cRGD ligand on the integrin interactions, along with the thermodynamic parameters and free energy landscape alteration during synchronous and asynchronous unbinding processes of multiple cRGD, were also examined.

Materials and Experimental Methods

Cell culture

To conduct the investigations, all four cell lines (PANC-1, BxPC-3, MIA-PaCa-2, and hTERT-HPNE) were initially obtained from the American Type Culture Collection (ATCC). Cells used were kept under 10 passages and cultured based on ATCC recommendations in a

VWR 25 cm2 culture flask. Glass bottom culture dishes with a 35 mm glass center were washed with 70% ethanol and UV sterilized for one hour inside a biosafety cabinet. Two days before imaging, approximately 40,000 cells suspended in 1 mL of their respective media were seeded onto the confocal microscopy dishes. Prior to imaging, the cell culture media was removed, and the dish washed three times using phosphate buffered saline.

Tip functionalization

Three chemical reactions need to be performed in order to functionalize the AFM tips. The first reaction is amino functionalizing. Then, the amino-coated tip is linked to Azido-dPEG®$_{12}$-NHS (PEG: polyethylene glycol) which was purchased from Quanta Biodesign. First, Si3N4 tip is amino functionalized by immersing the cantilever in ethanolamine hydrochloride/DMSO solution overnight at room temperature, where the solution is prepared by dissolving 3.3g ethanolamine hydrochloride in 6 mL DMSO while heating to 60°C in a glass beaker. Before immersing the cantilever in the solution, the cantilever is washed with Chloroform, dried with Nitrogen gas, placed in Ozon cleaner, washed again with water and ethanol, and dried with Nitrogen. Second, the amino-coated tips are incubated in the PEG-linker solution for 2 hours. PEG linker compound is dissolved in Chloroform with 6.6 mg/mL concentration. After that, the cantilever is extensively washed in Chloroform and dried with Nitrogen.

Finally, the copper complex catalyst was made by mixing copper (II) sulfate (72 mg) with N,N,N',N',N''–penthamethyl diethylenetriamine (PMDETA) (442 µL) were added to 3 mL dionized water and mixed for 2 hours. Ascorbic acid solution (1.4 µmol) was prepared with deionized water. The synthesized cRGD peptide (1mg) was first dissolved in 100 µL of DMSO and 900 µL of deionized water was added. To the peptide mixture, 16 µL of both copper

complex and sodium ascorbate were added. The reaction mixture was then added to a confocal dish containing the AFM tips. The dish containing the AFM tips was then slowly rocked for 24 hours at room temperature.

Synthesis and characterization of the cRGD peptide

Microwave-assisted, solid-phase peptide synthesis was carried out using a Liberty Blue (CEM Corporation) synthesizer. The resin used was a Rink amide (purchased from CEM Corporation). The sequence hexynoic acid-Cys(Acm)-Arg(Pbf)-Gly-Asp(OBtu)-Lys(Boc)-Gly-Pro-Asp(OBtu)-Cys(Acm)-OH was synthesized without the final deprotection step. To cyclize, 0.1 mmol thallium trifluoroacetate in DMF (5 mL) was stirred with the peptide-resin conjugate for 1 hour. The resin was then washed with DMF and dichloromethane 3 times.

Next, the peptide was cleaved from the resin using trifluoroacetic acid (19 mL), distilled water, (0.5 mL), and triisopropylsilane (0.5 mL) for 2 hours. Whatman Grade 1 qualitative filter paper was used to collect the peptide in a 50 mL centrifuge tube to which 30 mL of ice-cold diethyl ether was added. The precipitate was collected and dried in a vacuum desiccator overnight. The dried product was then characterized by MALDI-ToF mass spectrometry (observed mass: 1041.42, expected mass: 1042.43, elemental composition $C_{41}H_{64}N_{14}O_{14}S_2$).

Synthesis of cRGD peptide–Cy5 conjugate

The Cy5 Azide (Sigma-Aldrich) was reacted with the alkyne (hexynoic acid) moiety of the cRGD peptide using Click chemistry (1:1 molar ratio peptide to Cy5-Azide). The copper complex was made by mixing copper (II) sulfate with N, N, N', N', N"–pentamethyl diethylenetriamine (PMDETA) for 2 hours. Ascorbic acid solution (1.4 µmol) was prepared in distilled water. The reaction mixture was then stirred for 24 hours at room temperature. The

mixed solution was then transferred to a 1000 kD dialysis bag and dialyzed against water for 72 hours to remove the catalyst (PMDETA and ascorbic acid) as well as unreacted cRGD peptide.

Cell fluorescent imaging studies

5,000 pancreatic cells were transferred to an 8-well glass coverslip (ibidi µ-slide 8-well glass bottom). Cells were incubated overnight to allow for attachment to coverslip. New media was added along with 100 µM cRGD-Cy5. The cells were incubated with cRGD-Cy5 for 2 hours. Post incubation, cells were washed three times with phosphate buffered saline and then fixed with 4% paraformaldehyde. Cellular actin was stained using phalloidin-488 (Biotium) manufacturer protocol. The cell nucleus was stained using NucBlue™(Invitrogen). Cells were imaged using a Zeiss Axio Observer Z1 LSM 700 microscope with a 40x objective. Images were subsequently analyzed using Imaris Ultimate (ver 8.3).

AFM measurements

The cell imaging and spectroscopy measurements were conducted using a commercial AFM (NT-MDT NTEGRA) (Figure 29) with optical viewing system and V-shaped silicon nitride AFM probes with a spring constant of 0.08 N/m (Nanoworld) at room temperature. Cantilever spring was calibrated by the thermal noise fluctuation methods [62], and the deflection sensitivity of each tip was calibrated by force-distance curve measurements on the bare glass area of the petri dish.

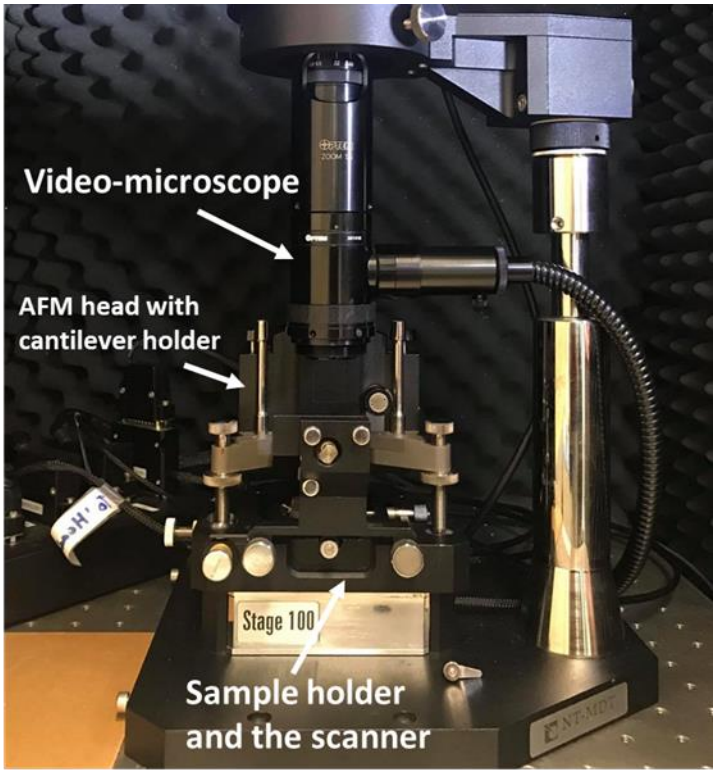

Figure 29. Atomic force microscope (NT-MDT NTEGRA).

At least 5 cells at each condition were randomly selected for the force measurements. To prevent the false measuring of already dying or dead cells due to the drug treatment, we excluded the cells that are loosely attached or floating. The scanning resolution was 256 × 256 pixels with a scan rate of 0.1–0.5 Hz, depending on the scanning areas of irregular cell size. The acquired images were flattened, if required, to eliminate the background noise and tilt from the surface using all unmasked portion of scan lines to calculate individual least-square fit polynomials for each line.

Functionalizing silicon chips and validating ligands density

The same functionalization protocol described previously (chapter 3) was followed to functionalize silicon chips instead of silicon tips, except attaching cRGD molecules. Instead, we fluorescence labeled the PEG linker free end of azido group to AlexaFluor 674 alkyne molecules (CCT). Four chips were coated with the PEG linkers, two with 6.6 mg/ml concentration and two

with 8 mg/ml. Then, the chips were imaged by the fluorescent microscope (fluorescent microscope type), and finally the light intensity of fluorescent images were measured over at least five areas on each chip using ImageJ 1.53e software.

Functionalizing silicon chips and validating ligands attachment

The same functionalization protocol described previously was followed to functionalize silicon chips instead of silicon tips. In this experiment, cRGD molecules were labeled with AlexaFluor 647 NHS ester (CCT) through their lysine amino acids of its side-chain amine group. Then, cRGD molecules were attached to the PEG linkers coating the chip. Here, the used PEG linker concentration was 6.6 mg/ml. Then, two coated chips were imaged by the fluorescent microscope (fluorescent microscope type), and finally the light intensity of fluorescent image was measured over at least five areas on each chip using ImageJ 1.53e software.

Statistical analysis

All data were expressed as mean ± standard deviation and analyzed using the Prism 8 (GraphPad software). The statistical significance was determined using analysis of variance followed by suitable post-hoc test. The *p*-values lower than 0.05 were considered statistically significant.

Results and Discussion

Binding measurements of cRGD ligands to integrin receptors on the cell surface

AFM-based single molecule binding spectroscopy (SMBS) permits to quantify intermolecular force between individual receptors and their ligands. Figure 30A illustrates the rupture force measurements on a cancer cell acquired by an AFM topography image, which is in accord with optical images of the cell (Figure 30B). In particular, a fluorescence image shows that the circular-shape nucleus (blue fluorescence) is located around the central cytoplasmic

region of cell, where the force-distance (FD) measurements were performed. The blue color is due to labeling the nucleus with DAPI stain, while the cellular actin was stained with green to show the cell boundaries. The alkyne linked cyclic-RGD (cRGD) peptides were covalently attached to an amino-coated AFM probe through a bifunctional polyethylene glycol $(PEG)_{12}$ linker utilizing azide-alkyne cycloadditions and EDC/NHS crossing linking with carboxylate with amines (Figure 30C).

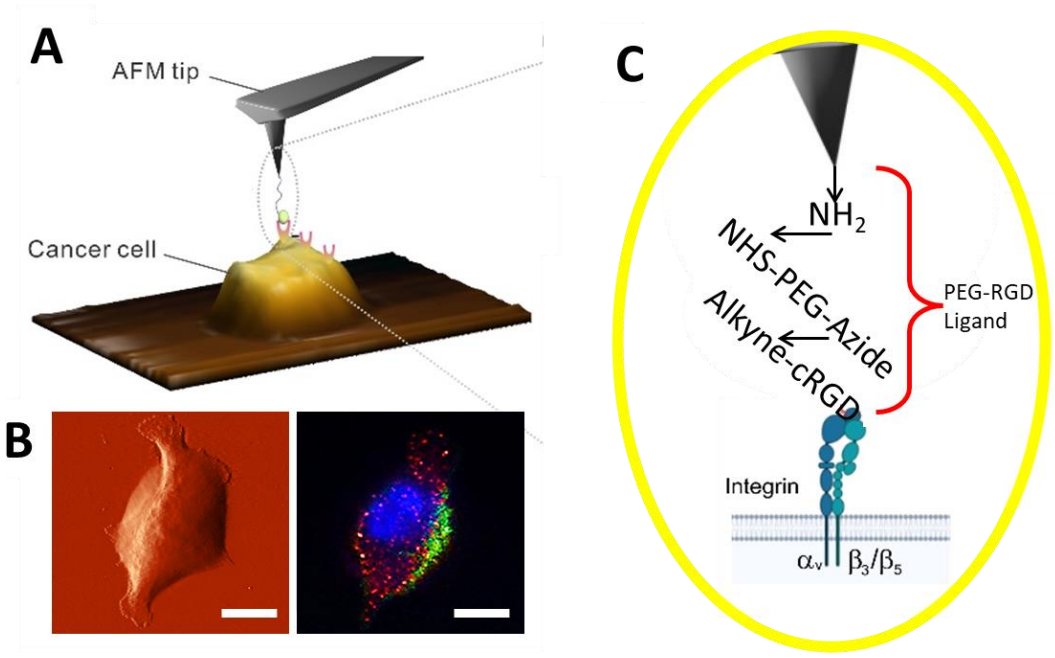

Figure 30. Rupture force measurement of the cRGD-integrin pair. (A) Schematic diagram of single molecule force spectroscopy measurement between the ligand-coated tip and the cell membrane receptor. (B) AFM phase image of PANC-1 cell (left image) and optical microscope image (right image). (c) Schematic representation of ligand binding site on an integrin receptor using AFM functionalized tip. The scale bars are 5 μm.

The additional role of the PEG linker is to add a space between the probe and cell surface, allowing the cRGD ligands to freely interact with the target receptors on the cells. After functionalization, the probe was brought into contact with the cell surface and retracted from it at a constant pulling speed. While approaching to and retracing from the surface, the deflection

signal of the probe as a function of the distance between the probe and surface was recorded and converted to the standard FD curve using Hooke's law described previously.

According to well-known protocol [47], PEG linkers are dissolved in chloroform with 6.6 mg/ml concentration to achieve single or few ligands attachment on the AFM tip. To confirm that, we tried two more different concentrations for the ligands than the standard protocol value.

Initially, the concentration 5 mg/ml was used for the ligands where we could not obtain recognition events with the receptors. Then, 6.6, 8 and 13 mg/ml of the ligands were tested, and the single bindings appear in both concentrations. In the experiments of standard concentration, 16% of total 1,024 FD curves successfully recognized the detection of the integrins using the cRGD-coated tip. From the recognition events, 92% were of single binding events and 8% were double or multiple. On the other hand, 8mg/ml ligand concentration led to approximately 77% of single binding events, while 23% of higher rupture force peak at ~155 pN. The highest ligand concentration, 13 mg/ml, led to around 53% of single binding events and 47% of multiple bindings (divalent and trivalent) (Figure 31).

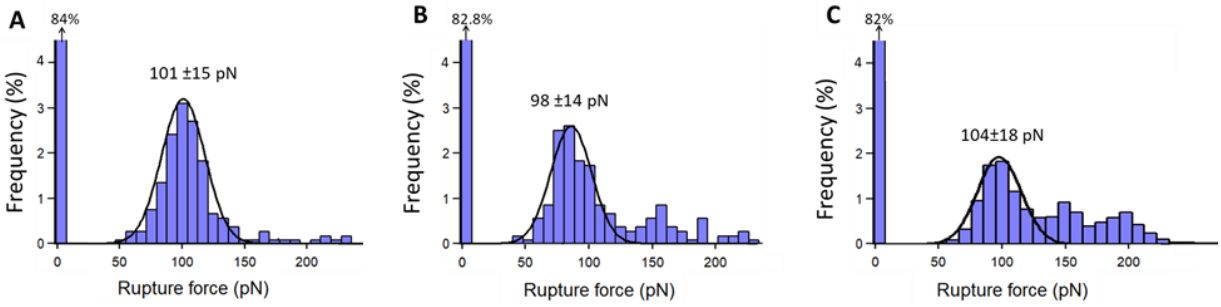

Figure 31. Force spectroscopy data using two different ligands concentrations, 6.6 mg/ml A, 8 mg/ml B, and 13 mg/ml C. The gaussian fitting indicates the single binding events. 1024 curves for each condition were recorded at 1μm/s tip retracting speed. At least three cells were tested from two independent samples per each condition using independent coated tips.

Here, the number of ligands bound to the AFM tip is not limited to just one ligand but is restricted to identifying single molecule detachments. The low density of ligands is also

necessary for single binding recognition experiments to allow sufficient ligand mobility. Another ligands-associated requirement to achieve the single-binding interaction is covalently binding the ligands to AFM tip. The followed protocol guarantees covalent bonds between the ligands and AFM tip which is more than ten times stronger than the receptor-ligand bonds.

To validate our AFM tip functionalization, silicon nitride chips were functionalized applying the previously described protocols. Instead of measuring the chip roughness which is an inaccurate qualitative method [121], we fluorescence labeled the ligands-coated silicon nitride chips [47] [122] specifically fluorescently labeling cRGD peptide, while using PEG linker concentration of 6.6 mg/ml. As a control, nonfunctionalized silicon nitride chips were incubated in the fluorescent probe solution. Then, we compared the light intensity for both: the coated and noncoated chips, resulting in 30 ± 2 a.u. intensity for the coated chip while dark with 2 ± 0.3 a.u. intensity for the noncoated one (Figure 32).

To validate the ligands concentration, the linkers were attached to the chip. As controlling the ligands density depends on the linker density, three linkers' concentrations were used. The free end of linkers was fluorescence labeled and then the chip was fluorescence imaged. The experiment was repeated with the three different concentrations of PEG linker: 0, 5, 6.6, and 13 mg/ml. The intensity of fluorescent images of PEG-coated chips were measured to give 2.2 ±0.2, 4 ± 2, 32 ± 4, and 50 ± 3 a.u. respectively (Figure 32).

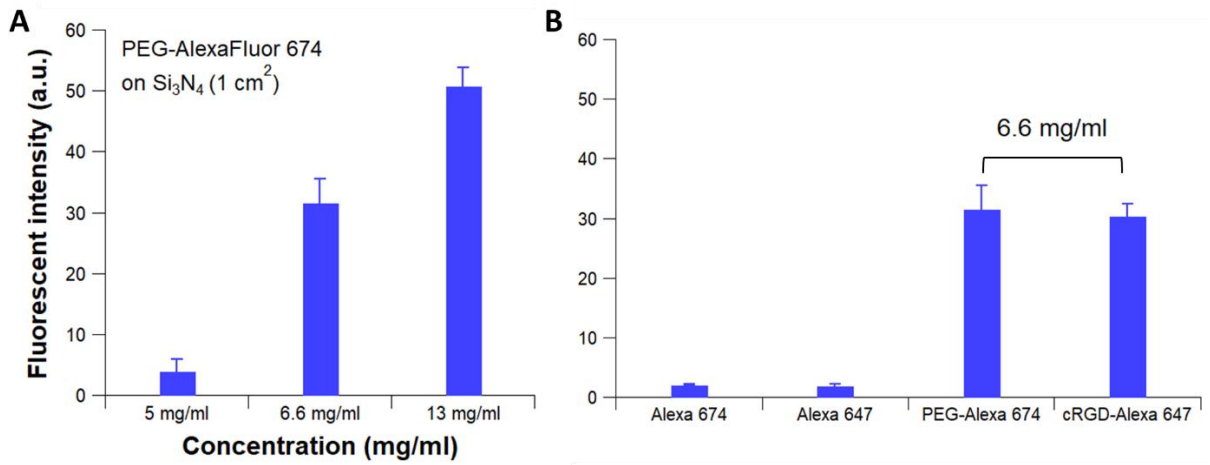

Figure 32. The light intensity data of the fluorescent images of the functionalized chips, resulted upon fluorescence imaging: PEG-Alex 674 linkers at three different concentrations (5, 6.6, 13 mg/ml) (A), and cRGD-Alexa 647 molecules with 6.6 mg/ml linker concentration (B). In (B), the coated fluorescent chips with PEG and cRGD were compared to control chips that were only incubated with the dye molecules with no coating.

Typical FD curves obtained with the cRGD ligand coated probe were displayed in Figure 33B, in which a sharp rupture force F_r of 102 pN (sawtooth pattern in the FD curves) between individual cRGD ligand and integrin receptor was clearly depicted. In contrast, the FD curves at certain area of the cell surface showed only elastic response without the rupture pattern, indicating no ligand-receptor interactions while performing SMBS measurements (Figure 33A).

Although either the probe or ligands could bind nonspecifically and produce similar sawtooth patterns in the FD curve (chapter 3 Figure 9, 10, and 11), such events occur rarely and only in a short distant from the contact region (< 10 nm), along with relatively small force magnitude (< 50 pN), which makes it easily distinguishable from the specific unbinding force of ligand-receptor bond. The rupture distance for the specific events took places > 100 nm from the contact region because of the locally extended height of the elastic plasma membrane while pulling the ligand-receptor bond, rather than the stretched length of PEG-cRGD ligand.

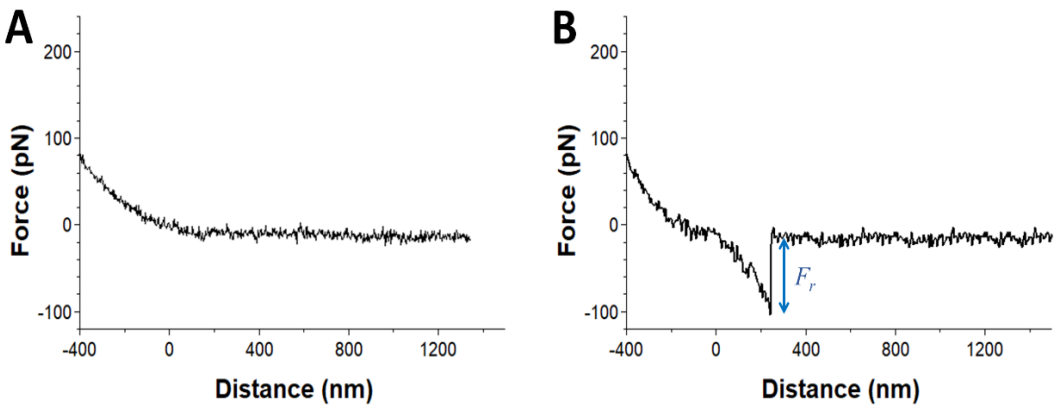

Figure 33. Representative FD curve (A) shows no binding between the receptor and its ligand. (B) Representative retracting FD curve for the single integrin-cRGD binding, where Fr is the rupture force of bond.

The FD measurements were repeated over a wide range of the pulling speed of the probe, which determines a loading rate. When the loading rate increased, F_r increased linearly with the logarithm of the loading rate (Figure 34).

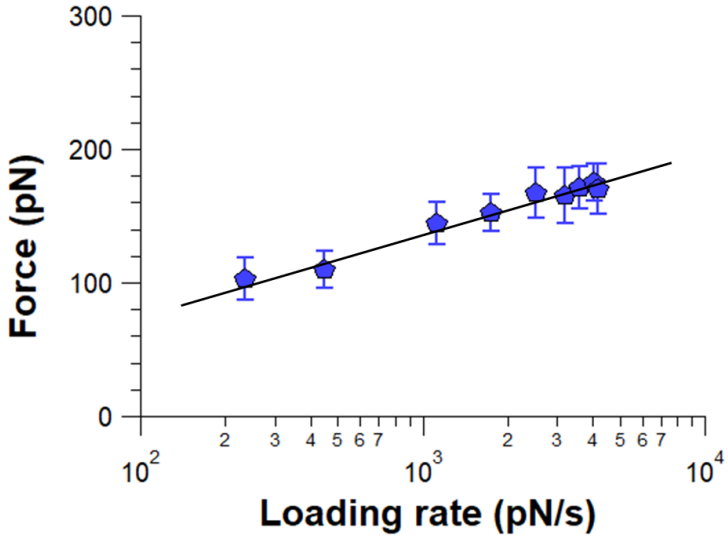

Figure 34. Most probable rupture forces measured at various loading rates. The black curve is the linear fit to average force data. The energy barrier width can be extracted from the slope of the linear fit.

This linear trend agrees with the Bell-Evans model [37] of a single barrier transition between bound and unbound states of the receptor-ligand binary complex. The free energy

landscape depicts the force-driven changes of thermodynamic parameters, including the dissociation off rate k_{off}, the barrier width x_b from unbound to the transition state, and the energy barrier E_b (Figure 35).

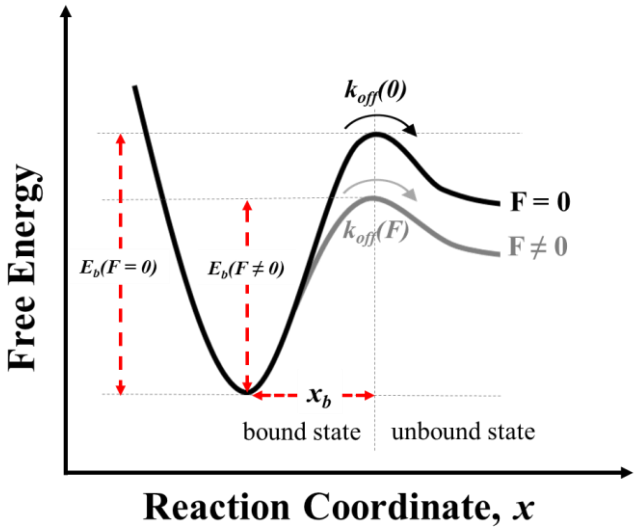

Figure 35. The schematic representation for energy landscape demonstrates dissociation over energy barrier without force (black curve), and with applied external force (grey curve).

Molecular recognition and specificity of cRGD to integrin α_V heterodimer receptors

Confocal laser scanning microscopy with the cells and Cy5-labeled, integrin targeting cRGD verified the specific bindings of cRGD to the ITG receptors (Figure 36A), which were spatially distributed on the cell surface including a ligand interacting cell's top area (Figure 36B). A binding force-based, ligand-receptor recognition map also confirmed the presence of integrin receptors on the cell's top surface (Figure 36C).

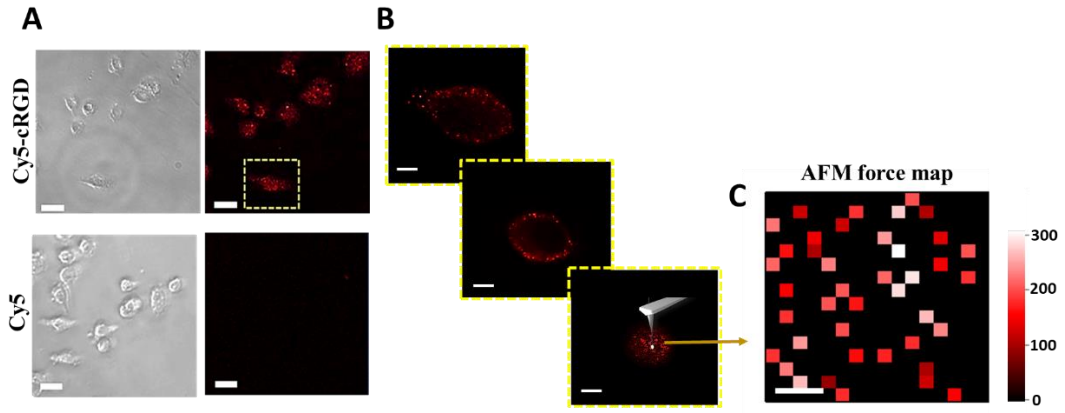

Figure 36. Recognition events between the integrins and cRGD ligands using confocal fluorescent microscope (A, B) and AFM (C). Fluorescent images show the stained cRGD molecules with Cy5 which attached to the receptors on PANC-1 cells, indicating the existence of active integrins on the cell surface. The optical microscope images also confirm the control experiment using only the Cy5 molecules in the samples. In (B), confocal fluorescent images were taken for the assigned cell in at three different depths of the cell starting exactly on the flat central area of the cell surface, and two images through the cell where 1 μm distance is between each image. Scale bar is 20 μm in the optical microscope images (A), 1 μm in (B) and 100 nm in the AFM receptor distribution image (C).

The two-dimensional (2D) map revealed a random, sparse distribution of integrin receptors on the surface and the normal distribution of the F_r strength at a constant loading rate of 450 pN/s with a mean and standard deviation of 105 pN and 17 pN (n = 2,048 FD curves from eight cells), respectively (Figure 37).

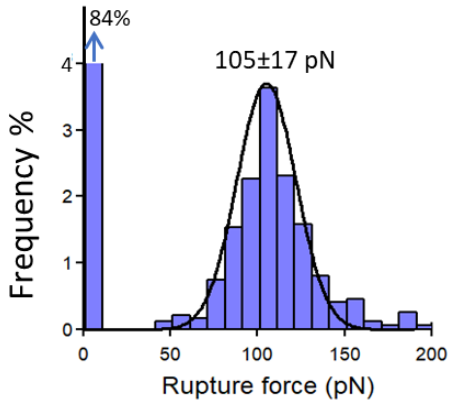

Figure 37. The rupture force histogram at loading rate of 450 pN/s collected from 2,048 FD curves from eight cells, different samples using independent tips.

Compared to the unrecognized area by the cRGD ligands (black color in the map), the relative surface coverage of the integrin receptors was ~ 16% for PANC-1 cells. To further validate specific interactions between cRGD and integrin receptors, an additional recognition mapping with the cRGD-coated AFM probe on the pretreated cell were performed (Figure 38).

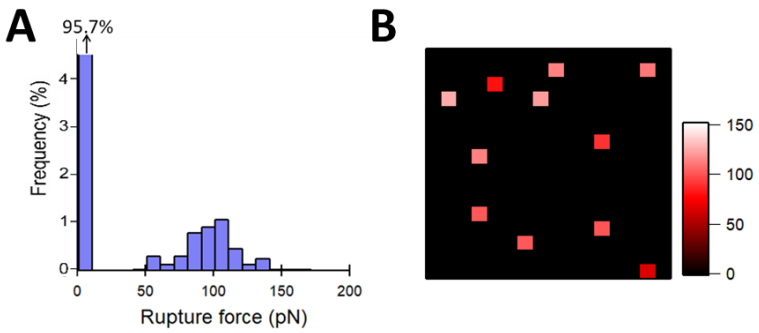

Figure 38. Control experiment of recognition events for cRGD-integrin binding. Blocking the receptors by adding free cRGD peptides to the cells and then recording FD curves with the coated tips lead to reduce detecting the recognition events. Representative maps, 500×500 nm^2 and 16×16 curves (B) were inserted with the histogram (A). (n = 2,048 FD curves) were performed on at least seven cells from different samples using independent tips. The scale bar is 100 nm.

The cell was pre-incubated with an excessive amount of freely diffusive cRGD peptides to block integrin receptors on the cell before SMFS measurements. The recognition map shows almost no surface area were recognized by the probe, suggesting that most integrin receptors on the surface was occupied by the free-cRGD peptides (Figure 38) and cRGD strongly binds to the integrin receptors. As consequences, the relative surface coverage of integrin receptors was decreased from 15% to 4%.

These control experiments were carried out with multiple AFM probes and cells to include cell-to-cell variability and reproducibility.

Distribution and binding strength of integrin receptors on three pancreatic cancer cell lines

Force recognition measurements between cRGD and integrin α_V heterodimers on the cell surfaces of three pancreatic cell lines (PANC-1, BxPC-3, MIA PaCa-2) and one control cell line

(HPNE) were carried out to compare the distribution, binding strength, and surface coverage of the heterodimers on each cell line.

In each cell line, the fluorescence image obtained with Cy5 labelled, free-cRGD peptides and the recognition map obtained with SMFS measurements show uniform distribution of the integrin α_V heterodimers on the cell surface. It should be noted that the fluorescence image includes the receptors on all cell surfaces including top and bottom area of the cell, while 2D recognition map represents only cell's top surface area.

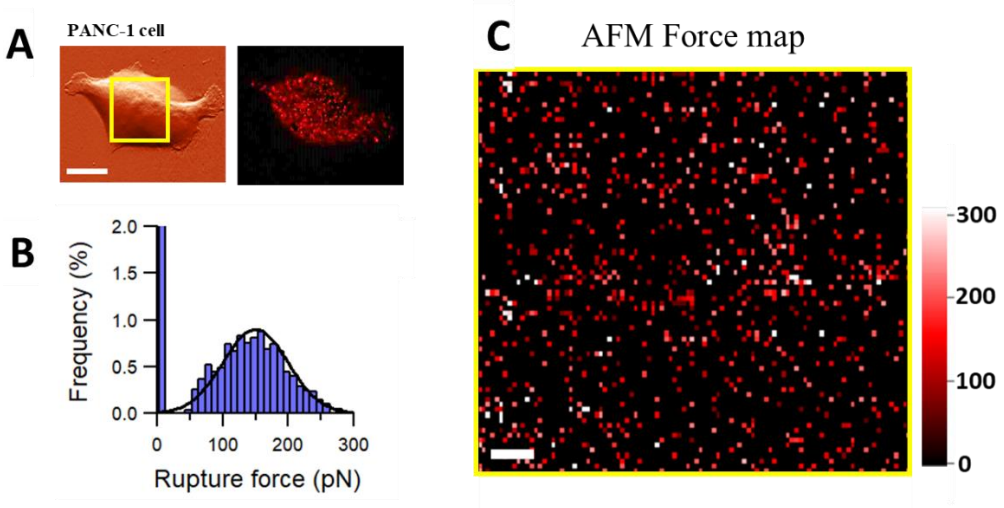

Figure 39. Recognition map obtained with SMFS measurements shows distribution of the integrin α_v heterodimers on the cell surface of the pancreatic cancer cell line PANC-1. For one cell, an AFM phase image and a fluorescence image obtained with Cy5 labelled, free-cRGD peptides (A) besides a histogram of the rupture force measurements with average 165 ± 42 pN (B) and the force map of receptor distribution with 13% coverage (C). The scale bar is 10 μm in the AFM images, and 1 μm in the AFM maps.

The surface coverage of the integrin α_v heterodimers on PANC-1 cells was measured to be 13% (Figure 39). Compared to the PANC-1 cell, other cells including BxPC-3 (Figure 40), MIA PaCa-2 (Figure 41), and HPNE (Figure 42) showed less than twice amount of the integrin α_V heterodimers on the cell surface.

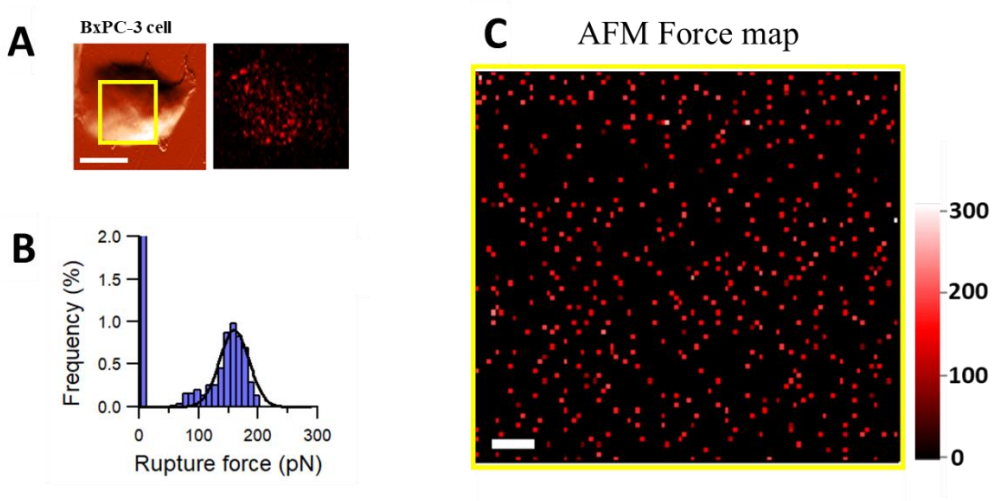

Figure 40. Recognition map obtained with SMFS measurements shows distribution of the integrin αV heterodimers on the cell surface of the pancreatic cancer cell line BxPC-3. For one cell, an AFM phase image and a fluorescence image obtained with Cy5 labelled, free-cRGD peptides (A) besides a histogram of the rupture force measurements with average 175 ± 21 pN (B) and the force map of receptor distribution with 5.9% coverage (C). The scale bar is 10 μm in the AFM images, and 1 μm in the AFM maps.

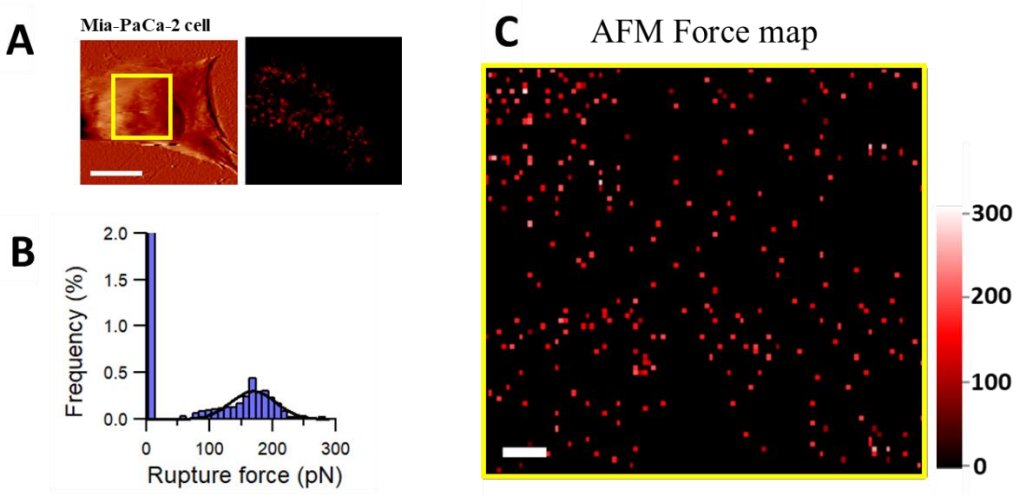

Figure 41. Recognition map obtained with SMFS measurements shows distribution of the integrin αV heterodimers on the cell surface of the pancreatic cancer cell line Mia-PaCa-2. For one cell, an AFM phase image and a fluorescence image obtained with Cy5 labelled, free-cRGD peptides (A) besides a histogram of the rupture force measurements with average 168 ± 40 pN (B) and the force map of receptor distribution with 3.4% coverage (C). The scale bar is 10 μm in the AFM images, and 1 μm in the AFM maps.

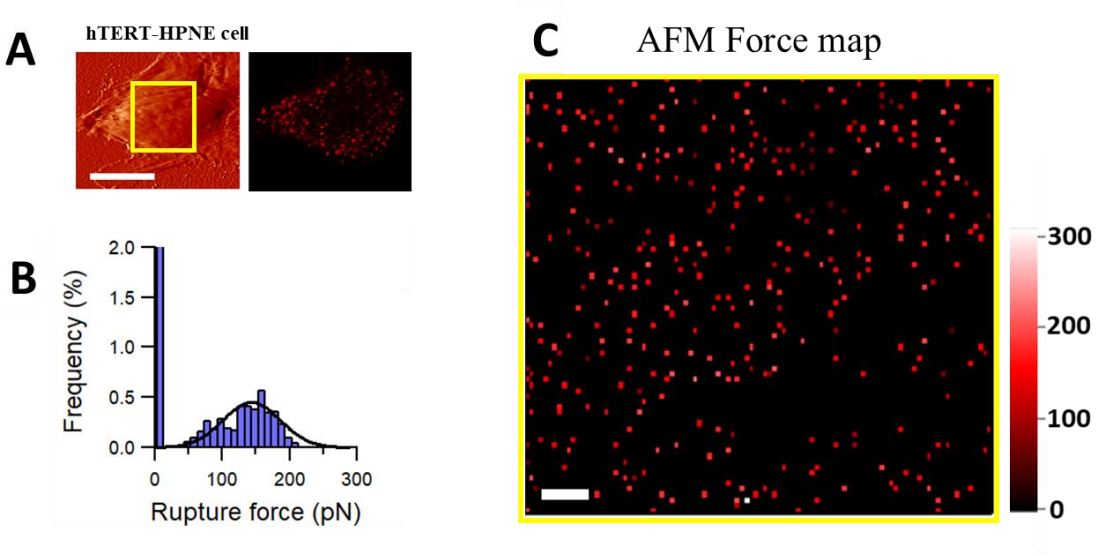

Figure 42. Recognition map obtained with SMFS measurements shows distribution of the integrin αV heterodimers on the cell surface of the pancreatic cancer cell line hTERT-HPNE. For one cell, an AFM phase image and a fluorescence image obtained with Cy5 labelled, free-cRGD peptides (A) besides a histogram of the rupture force measurements with average 150 ± 42 pN (B) and the force map of receptor distribution with 4.7% coverage (C). The scale bar is 10 μm in the AFM images, and 1 μm in the AFM maps.

In contrast to the cell type dependent integrin expression levels, the distributions of rupture force strength for individual cRGD-integrin bonds resulted in the normal distributions for all cell lines at the identical roading rate of 3,200 pN/s, and their means were not significantly different from each cell line ($P < 0.05$). These results imply that the strength of rupture force required to break the cRGD-integrin bond is independent on the cell type. Additionally, a logarithmic trend of the rupture force as a function of the loading rates observed in BxPC-3 and MIA PaCa-2 cell lines further supports the force-assisted, single-barrier transition of the cRGD-integrin complex between bound to unbound state regardless cell type (Figure 43).

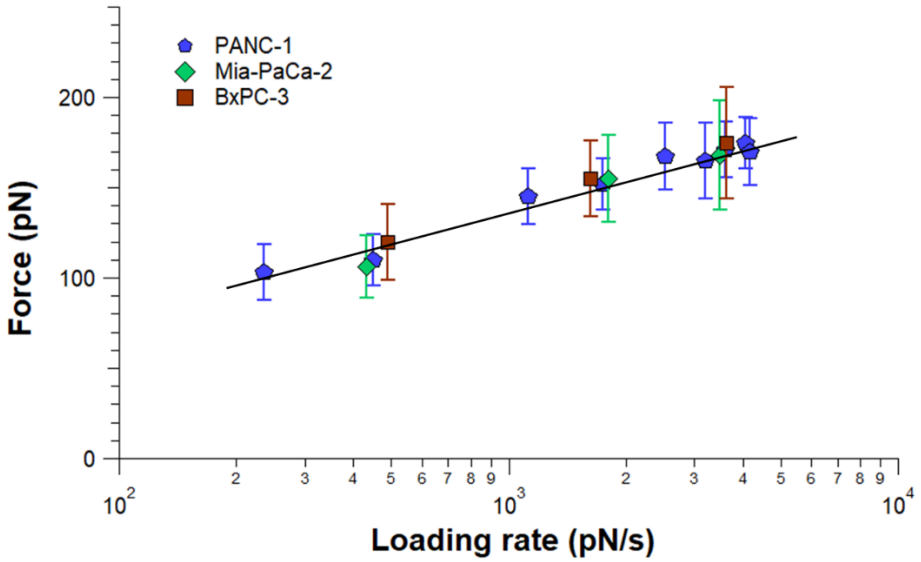

Figure 43. Rupture force dependency on the loading rates recorded for av integrin-cRGD binding using three pancreatic cancer cell lines: PANC-1, Mia-PaCa-2, and BxPC-3. The data shows the consistency of measurements regardless cell type.

Multivalent cRGD-ITG interactions

In addition to single-molecule binding events, multivalent interactions of cRGD-ITG were examined. We performed controlled experiments using the functionalization protocol that limits the ligand density on the probe and yield an average of single receptor-ligand bond. This strategy allows us to distinguish individual events when observed multiple receptor-ligand interactions. Figure 44 shows the distribution of the rupture force obtained from experiments repeated using several probes and cells (n =10).

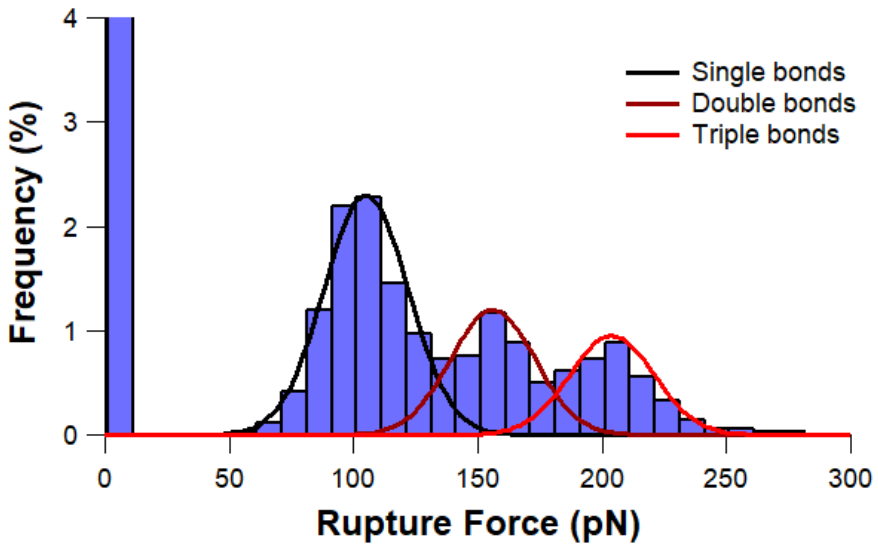

Figure 44. Histogram of rupture force measurements obtained by performing SMFS using high density ligands on the functionalized AFM-tips. Multiple peaks were resulted indicating the number of bonds formed between the integrins and cRGD ligands.

The presence of several ligands on the probe leads to multivalent cRGD-ITG interactions, resulted in the multiple peaks in the rupture force distribution (Figure 44). Thus, additional peaks with the mean of F_r = 157 pN and F_r = 205 pN at the higher force regime (> 105 pN) correspond to rupture force of divalent and trivalent interactions of ligand-receptor, respectively. The strength of divalent bonds was smaller than the simple addition of two monovalent bond ($F_{di} < 2F_{mo}$), and the strength of trivalent bonds was smaller than the three times monovalent bonds ($F_{tri} < 3F_{mo}$). Thus, the strength of multivalent bonds scaled not linear additively, but sub-linearly with increasing bond number, which is in agreement with theoretical predictions of a noncooperative multivalent model and previous experimental observations [123].

In particular, the average rupture force measured in our experiments agreed with the reliability theory by Tees et al., in which the strength of rupture force of N bonds scales with the Harmonic number ($F_N = H_N\langle F_1\rangle$; $H_N = \Sigma(1/i)$). These observations led us to conclude that the

multiple cRGD ligands on the AFM probe interacts with integrin receptors on the cell surface in parallel and bonds are independent of each other.

Dynamic force spectroscopy (DFS) was further performed to examine the load-dependent multivalent cRGD-integrin interactions. Both divalent and trivalent rupture force resulted in a linear trend by taking logarithmic scale of loading rates, suggesting that unbinding mechanism of each bond in multivalent interactions is governed by the Bell-Evans model. Results from FD and DFS measurements enable us to extract several important physical parameters associated with binding thermodynamics. The relationship between F_r and loading can be described by the Bell-Evans expression

$$F = \frac{k_B T}{x_b} ln\left(\frac{r x_b}{k_{off}^0 k_B T}\right), \quad (6)$$

where k_B the Boltzmann constant, T the temperature, r is the loading rate, k_{off}^0 is the kinetic-off rate in the absence of external perturbation ($F = 0$), and x_b is the barrier width from unbound to the transition state. Our DFS data fit equation (6) very well, and fitting determines the values of k_{off}^0 and x_b for multivalent cRGD-integrin bonds.

Single linear fit to the logarithmic loading rate implies the ligand-receptor transitions from bound to unbound occur through a single barrier in the relatively slow loading range from 235 to 6720 pN/s used in the experiments. The energy landscapes of multivalent interactions of cRGD-integrin reconstructed from the DFS measurements were depicted in Table 1. The value $k_{off}^0 = 0.1863\ s^{-1}$ for the monovalent cRGD-integrin bond was consistent with previous studies of cRGD ligand and several cell receptors, which further validates single-molecule interactions between α5β1 Integrin and fibronectin [119].

Table 1. Dynamic force spectroscopy (DFS) results for single and multiple α_v integrin-cRGD bindings. The data was fitted to Bell-Evans model and then the thermodynamic parameters k_{off}^0 (off-rate constant) and x_b (energy barrier width) were extracted. The energy barrier values were also calculated.

Number of Bonds	x_b ***(A°)***	k_{off}^0 ***(s^{-1})***	E_b ***(K_BT)***
Single	1.57	0.1863	24.01
Double	1.61	0.0571	25.19
Triple	1.68	0.0090	27.03

Compared to the monovalent bond, k_{off}^0 values for divalent and trivalent cRGD-integrin bonds were decreased 3.2 folds and 20 folds, respectively. These results indicate that multivalent bonds increase the stability of cRGD-integrin bound states. Additionally, we found the small x_b value (~ 1.6 Å) which is good agreement with values determined for cell surface receptors bound to peptide-based ligands [124]. The x_b values were increased from 1.57 to 1.68 Å with number of bonds, implying the width of the potential well of the bound state became widened. Although the widen width of the potential well could contribute to the additional stability of the multivalent bound states, little changes in the x_b values could attribute to the mechanical or configurational constrains from other ligands rather than the existing of additional conformational substates between the bound to transitions states.

The rate of escape from bound to unbound states under external force could be analyzed by the Kramers problem, which can be written as $k_{off}^0 = we^{-E_b/k_BT}$, where w and E_b are the frequency prefactor and the potential barrier height, respectively. By taking $w \sim 5 \times 10^{10}$ s^{-1}, E_b was estimated to be 24.01, 25.19, and 27.03 k_BT for monovalent, divalent, and trivalent bonds, respectively. The trend of the increasing barrier height with bond number is consistent with other kinetic parameters, suggesting that multivalent bonds spend longer time in the bound states and enhance the stability of the bonds.

Sequential rupture of cRGD-integrin bonds

Finally, we discuss the asynchronous, sequential rupture events of divalent and trivalent interactions (Figures 45 and 46). For the divalent case, two possible unbinding of the cRGD-integrin bonds could occur: both bonds rupture synchronously (Figure 44); or two successive ruptures for each bond take places (Figure 45). The majority divalent unbinding events showed a single, synchronous rupture behavior with $<F_{di}>$ = 157 pN, and approximately 5% divalent bonds ruptured sequentially.

In the FD curves in Figure 45, the first rupture force corresponds to a breaking up of a weaker bond while pulling two cRGD-ITG complexes, and the second rupture represents a breaking event of the other, relatively strong bond. The first rupture force was measured to be 135.3 ± 5 pN, which is stronger than breaking monovalent bond, but less than the synchronous divalent rupture force. Such lower force for the asynchronous rupture could attribute to the intrinsically weakly bound cRGD-integrin complexes, the different lengths from the ligand to the receptors, and mechanical or geometrical constrain when pulling of ligands. In contrast, the mean of the second rupture force (100.2 ± 6 pN) was nearly the same strength of monovalent rupture force within 1σ, suggesting that the second bond acts as an independent, monovalent bond after dissociating of the other bond.

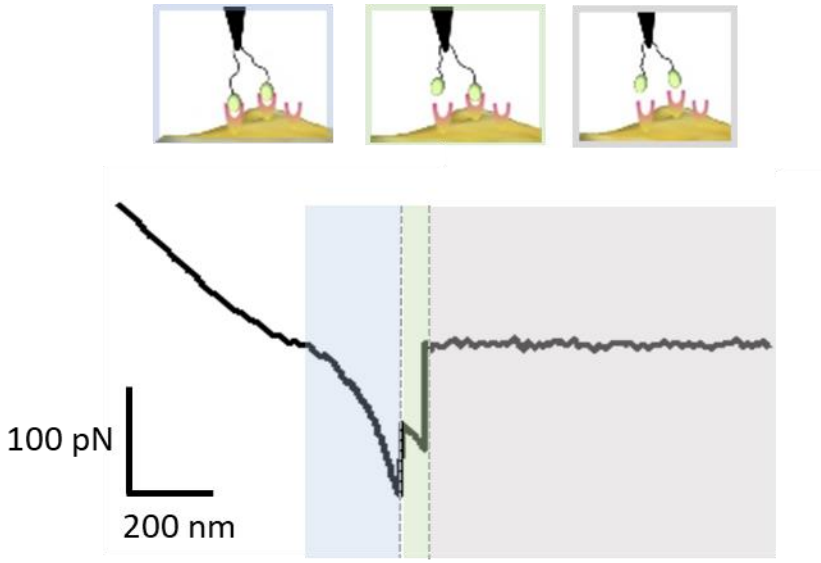

Figure 45. Asynchronous rupture event of divalent αv integrin-cRGD interaction. In the retracting FD curve, binding of the two bonds is around 135 pN (in the light blue area), while the rupture force of the lasted single bond is around 100 pN (in green area).

For the trivalent interactions, three different sequential unbinding events were observed: two rupture events occurred together at the either first (Figure 46A) or last (Figure 46B); or three rupture events took place one by one (Figure 46C).

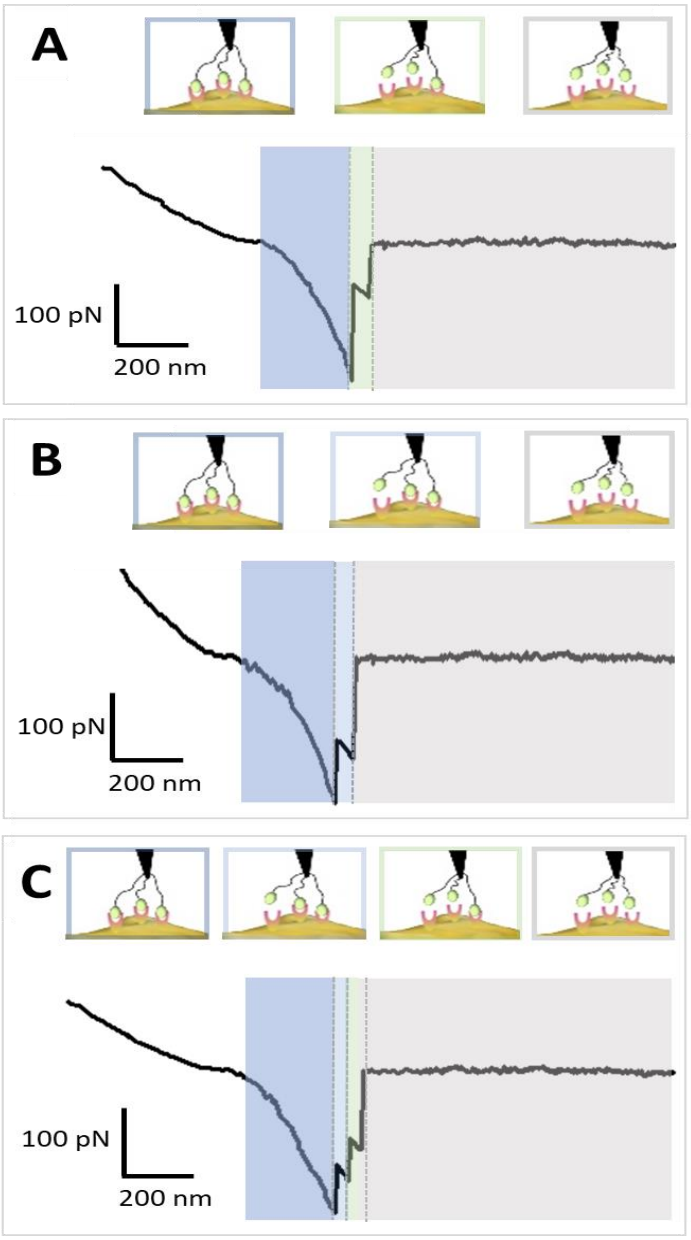

Figure 46. Asynchronous rupture event of trivalent αv integrin-cRGD interactions. In the retracting FD curve, rupturing of the two bonds occurs either first (A), or last (B), while the rupture event can also occur as a form of single rupturing one by one (C).

Regardless of the unbinding sequence, the first rupture force was closed to each other with the mean of 179.7 ± 7 pN, which lies between the force strength for breaking double and triple bonds synchronously. Interestingly, the last rupture force for both divalent bond and monovalent bond in the sequential events was nearly identical to that of synchronous rupture

cases (Figure 47). These results indicate that individual rupture mechanism and the force magnitude are independent to the multivalency interactions and further support the parallel bond model.

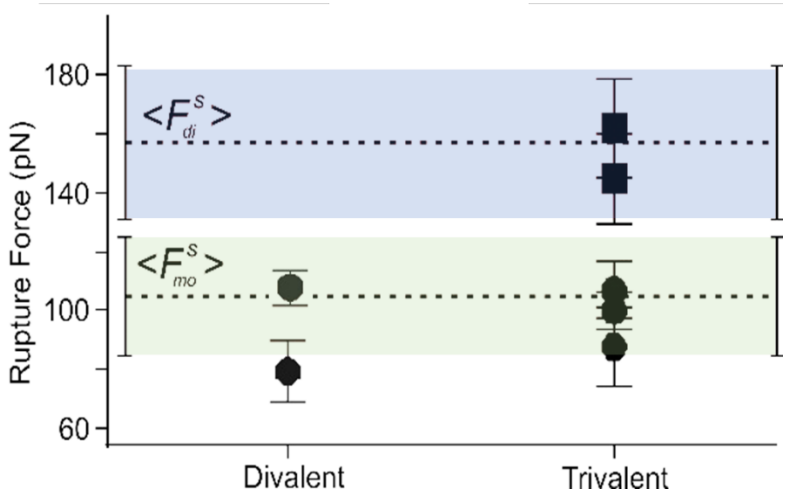

Figure 47. Rupture force diagram of the asynchronous rupture events distribution of the αv integrins and cRGD ligands. This illustration shows the average rupture forces of monovalent and divalent that occur during the divalent and trivalent rupturing.

CHAPTER 6. OVERALL CONCLUSION

In conclusion, we have demonstrated alteration of cancer cells' biomechanical and biophysical properties induced by the standard chemotherapeutic drugs using AFM-based, time-traced imaging and force spectroscopy measurements. We found that stiffness kinetics depends on the type of the drug, exposure time to the drug, and oxygen levels in the microenvironments, while the stiffness of untreated cancer cells remains consistent in both normoxia and hypoxia. In addition, such changes in the stiffness due to either disruption or reinforcement of cytoskeletal structure induced by the drug were coupled with substantial alteration in cellular morphology, surface roughness, and cytoadhesion. Although the drug treatment alone significantly affects the cellular stiffness, the efficacy can be dampened by drug resistance due to the hypoxia, emphasizing the complex underpinning mechanisms that govern overall biomechanical and biophysical properties.

Results from FD curves, 2D recognition mapping, and DFS measurements revealed several important physical parameters associated with binding and unbinding thermodynamics. First, the rupture force of individual cRGD-integrin bonds was unchanged for different pancreatic cancer cells and healthy control cells while the integrin population has substantially reduced. Second, the dissociation dynamics of the binary complex fitted to the Bell-Evans force-assisted, single-barrier two-state transition model, in which the kinetic off rate of multivalent bonds was substantially decreased. Third, sequential rupture events of multiple bonds revealed that the force strength for breaking up the initial bonds under multivalent interactions was weaker than that of synchronous multiple rupture events, but the last rupture events and the force strength were identical to the synchronous case, suggesting independent parallel bond mechanism. This study providing a quantitative relationship between cRGD-integrin binding

dynamics and multivalent interactions will allow a better understanding of integrin's binding selectivity, affinity, and stability to cRGD peptides and could help design of new cRGD-based nanoparticles for cancer imaging, drug delivery, and chemotherapeutics.

REFERENCES

[1] T. Förster, “Experimental and theoretical investigation of the intermolecular transfer of electronic excitation energy,” *Naturforsch*, vol. A 4, 321–327 (1949).

[2] M. J. Rust, M. Bates, and X. Zhuang, “Sub-diffraction-limit imaging by stochastic optical reconstruction microscopy (STORM),” *Nat. Methods*, vol. 3, no. 10, pp. 793–795, Oct. 2006, doi: 10.1038/nmeth929.

[3] T. Mulvey, “Electron microscopy—The U.K. involvement,” *Micron Microsc. Acta*, vol. 17, no. 2, pp. 67–75, Jan. 1986, doi: 10.1016/0739-6260(86)90036-5.

[4] G. Binnig, C. F. Quate, and Ch. Gerber, “Atomic Force Microscope,” *Phys Rev Lett*, vol. 56, no. 9, pp. 930–933, Mar. 1986, doi: 10.1103/PhysRevLett.56.930.

[5] N. Kodera, D. Yamamoto, R. Ishikawa, and T. Ando, “Video imaging of walking myosin V by high-speed atomic force microscopy.,” *Nature*, vol. 468, no. 7320, pp. 72–76, Nov. 2010, doi: 10.1038/nature09450.

[6] J. J. Heinisch *et al.*, “Atomic force microscopy - looking at mechanosensors on the cell surface.,” *J. Cell Sci.*, vol. 125, no. Pt 18, pp. 4189–4195, Sep. 2012, doi: 10.1242/jcs.106005.

[7] A. J. Katan and C. Dekker, “High-speed AFM reveals the dynamics of single biomolecules at the nanometer scale.,” *Cell*, vol. 147, no. 5, pp. 979–982, Nov. 2011, doi: 10.1016/j.cell.2011.11.017.

[8] C. Zhu, G. Bao, and N. Wang, “Cell mechanics: mechanical response, cell adhesion, and molecular deformation.,” *Annu. Rev. Biomed. Eng.*, vol. 2, pp. 189–226, 2000, doi: 10.1146/annurev.bioeng.2.1.189.

[9] P. Egan, R. Sinko, P. R. LeDuc, and S. Keten, “The role of mechanics in biological and bio-inspired systems,” *Nat. Commun.*, vol. 6, no. 1, p. 7418, Jul. 2015, doi: 10.1038/ncomms8418.

[10] C.-Y. Su *et al.*, “The Biological Functions and Clinical Applications of Integrins in Cancers,” *Front. Pharmacol.*, vol. 11, pp. 579068–579068, Sep. 2020, doi: 10.3389/fphar.2020.579068.

[11] C.-H. Heldin, B. Lu, R. Evans, and J. S. Gutkind, “Signals and Receptors,” *Cold Spring Harb. Perspect. Biol.*, vol. 8, no. 4, pp. a005900–a005900, Apr. 2016, doi: 10.1101/cshperspect.a005900.

[12] S. Suresh, “Biomechanics and biophysics of cancer cells,” *Acta Biomater.*, vol. 3, no. 4, pp. 413–438, Jul. 2007, doi: 10.1016/j.actbio.2007.04.002.

[13] D. J. Müller, J. Helenius, D. Alsteens, and Y. F. Dufrêne, “Force probing surfaces of living cells to molecular resolution.,” *Nat. Chem. Biol.*, vol. 5, no. 6, pp. 383–390, Jun. 2009, doi: 10.1038/nchembio.181.

[14] M. T. Woodside and S. M. Block, “Reconstructing folding energy landscapes by single-molecule force spectroscopy.,” *Annu. Rev. Biophys.*, vol. 43, pp. 19–39, 2014, doi: 10.1146/annurev-biophys-051013-022754.

[15] Y. Shan and H. Wang, “The structure and function of cell membranes examined by atomic force microscopy and single-molecule force spectroscopy.,” *Chem. Soc. Rev.*, vol. 44, no. 11, pp. 3617–3638, Jun. 2015, doi: 10.1039/c4cs00508b.

[16] A. M. Whited and P. S.-H. Park, “Atomic force microscopy: a multifaceted tool to study membrane proteins and their interactions with ligands.,” *Biochim. Biophys. Acta*, vol. 1838, no. 1 Pt A, pp. 56–68, Jan. 2014, doi: 10.1016/j.bbamem.2013.04.011.

[17] K. H. Vining and D. J. Mooney, “Mechanical forces direct stem cell behaviour in development and regeneration,” *Nat. Rev. Mol. Cell Biol.*, vol. 18, no. 12, pp. 728–742, Dec. 2017, doi: 10.1038/nrm.2017.108.

[18] P. Romani, L. Valcarcel-Jimenez, C. Frezza, and S. Dupont, “Crosstalk between mechanotransduction and metabolism,” *Nat. Rev. Mol. Cell Biol.*, vol. 22, no. 1, pp. 22–38, Jan. 2021, doi: 10.1038/s41580-020-00306-w.

[19] E. Evans and A. Yeung, “Apparent viscosity and cortical tension of blood granulocytes determined by micropipet aspiration.,” *Biophys. J.*, vol. 56, no. 1, pp. 151–160, Jul. 1989, doi: 10.1016/S0006-3495(89)82660-8.

[20] M. Dao, C. T. Lim, and S. Suresh, “Mechanics of the human red blood cell deformed by optical tweezers,” *J. Mech. Phys. Solids*, vol. 51, no. 11, pp. 2259–2280, 2003, doi: https://doi.org/10.1016/j.jmps.2003.09.019.

[21] J. Chen, B. Fabry, E. L. Schiffrin, and N. Wang, “Twisting integrin receptors increases endothelin-1 gene expression in endothelial cells.,” *Am. J. Physiol. Cell Physiol.*, vol. 280, no. 6, pp. C1475-1484, Jun. 2001, doi: 10.1152/ajpcell.2001.280.6.C1475.

[22] S. Suresh *et al.*, “Connections between single-cell biomechanics and human disease states: gastrointestinal cancer and malaria.,” *Acta Biomater.*, vol. 1, no. 1, pp. 15–30, Jan. 2005, doi: 10.1016/j.actbio.2004.09.001.

[23] Y. F. Dufrêne *et al.*, “Imaging modes of atomic force microscopy for application in molecular and cell biology.,” *Nat. Nanotechnol.*, vol. 12, no. 4, pp. 295–307, Apr. 2017, doi: 10.1038/nnano.2017.45.

[24] S. Suresh, “Biomechanics and biophysics of cancer cells.,” *Acta Biomater.*, vol. 3, no. 4, pp. 413–438, Jul. 2007, doi: 10.1016/j.actbio.2007.04.002.

[25] M. Duman *et al.*, “Atomic Force Microscopy (AFM) for Topography and Recognition Imaging at Single Molecule Level,” in *Encyclopedia of Biophysics*, G. C. K. Roberts, Ed. Berlin, Heidelberg: Springer Berlin Heidelberg, 2013, pp. 102–112. doi: 10.1007/978-3-642-16712-6_496.

[26] D. Mitrossilis *et al.*, “Real-time single-cell response to stiffness,” *Proc. Natl. Acad. Sci.*, vol. 107, no. 38, pp. 16518–16523, 2010, doi: 10.1073/pnas.1007940107.

[27] S. E. Cross, Y.-S. Jin, J. Rao, and J. K. Gimzewski, “Nanomechanical analysis of cells from cancer patients.,” *Nat. Nanotechnol.*, vol. 2, no. 12, pp. 780–783, Dec. 2007, doi: 10.1038/nnano.2007.388.

[28] R. P. Rambo and J. A. Tainer, “Super-Resolution in Solution X-Ray Scattering and Its Applications to Structural Systems Biology,” *Annu. Rev. Biophys.*, vol. 42, no. 1, pp. 415–441, May 2013, doi: 10.1146/annurev-biophys-083012-130301.

[29] P. Ray *et al.*, “Size-Transformable, Multifunctional Nanoparticles from Hyperbranched Polymers for Environment-Specific Therapeutic Delivery,” *ACS Biomater. Sci. Eng.*, vol. 5, no. 3, pp. 1354–1365, Mar. 2019, doi: 10.1021/acsbiomaterials.8b01608.

[30] Q. Li *et al.*, “Size-Tunable Metal–Organic Framework-Coated Magnetic Nanoparticles for Enzyme Encapsulation and Large-Substrate Biocatalysis,” *ACS Appl. Mater. Interfaces*, vol. 12, no. 37, pp. 41794–41801, Sep. 2020, doi: 10.1021/acsami.0c13148.

[31] J. Farmakes *et al.*, “Enzyme Immobilization on Graphite Oxide (GO) Surface via One-Pot Synthesis of GO/Metal–Organic Framework Composites for Large-Substrate Biocatalysis,” *ACS Appl. Mater. Interfaces*, vol. 12, no. 20, pp. 23119–23126, May 2020, doi: 10.1021/acsami.0c04101.

[32] J. Guck *et al.*, “Optical Deformability as an Inherent Cell Marker for Testing Malignant Transformation and Metastatic Competence,” *Biophys. J.*, vol. 88, no. 5, pp. 3689–3698, May 2005, doi: 10.1529/biophysj.104.045476.

[33] S. Suresh, “Elastic clues in cancer detection,” *Nat. Nanotechnol.*, vol. 2, no. 12, pp. 748–749, Dec. 2007, doi: 10.1038/nnano.2007.397.

[34] J. Tamayo, A. D. L. Humphris, R. J. Owen, and M. J. Miles, “High-Q Dynamic Force Microscopy in Liquid and Its Application to Living Cells,” *Biophys. J.*, vol. 81, no. 1, pp. 526–537, Jul. 2001, doi: 10.1016/S0006-3495(01)75719-0.

[35] E. L. Florin, V. T. Moy, and H. E. Gaub, “Adhesion forces between individual ligand-receptor pairs.,” *Science*, vol. 264, no. 5157, pp. 415–417, Apr. 1994, doi: 10.1126/science.8153628.

[36] J. Yu *et al.*, “Single-molecule force spectroscopy study of interaction between transforming growth factor beta1 and its receptor in living cells.,” *J. Phys. Chem. B*, vol. 111, no. 48, pp. 13619–13625, Dec. 2007, doi: 10.1021/jp0758667.

[37] E. Evans and K. Ritchie, “Dynamic strength of molecular adhesion bonds,” *Biophys. J.*, vol. 72, no. 4, pp. 1541–1555, Apr. 1997, doi: 10.1016/S0006-3495(97)78802-7.

[38] P. Hinterdorfer and Y. F. Dufrêne, “Detection and localization of single molecular recognition events using atomic force microscopy,” *Nat. Methods*, vol. 3, no. 5, pp. 347–355, May 2006, doi: 10.1038/nmeth871.

[39] P. Bongrand, C. Capo, J.-L. Mege, and A.-M. Benoliel, “Use of Hydrodynamic Flows to Study Cell Adhesion,” 2018, pp. 125–156. doi: 10.1201/9781351075572-6.

[40] D. E. Leckband, J. N. Israelachvili, F. J. Schmitt, and W. Knoll, “Long-range attraction and molecular rearrangements in receptor-ligand interactions.,” *Science*, vol. 255, no. 5050, pp. 1419–1421, Mar. 1992, doi: 10.1126/science.1542789.

[41] R. Merkel, P. Nassoy, A. Leung, K. Ritchie, and E. Evans, “Energy landscapes of receptor–ligand bonds explored with dynamic force spectroscopy,” *Nature*, vol. 397, no. 6714, pp. 50–53, Jan. 1999, doi: 10.1038/16219.

[42] A. Ashkin, “Optical trapping and manipulation of neutral particles using lasers,” *Proc. Natl. Acad. Sci.*, vol. 94, no. 10, pp. 4853–4860, 1997, doi: 10.1073/pnas.94.10.4853.

[43] C. Stroh *et al.*, “Single-molecule recognition imaging microscopy,” *Proc. Natl. Acad. Sci.*, vol. 101, no. 34, pp. 12503–12507, 2004, doi: 10.1073/pnas.0403538101.

[44] J. H. Krege *et al.*, “Generation and reproductive phenotypes of mice lacking estrogen receptor β,” *Proc. Natl. Acad. Sci.*, vol. 95, no. 26, pp. 15677–15682, 1998, doi: 10.1073/pnas.95.26.15677.

[45] L. Marinelli, A. Lavecchia, K.-E. Gottschalk, E. Novellino, and H. Kessler, “Docking Studies on αvβ3 Integrin Ligands: Pharmacophore Refinement and Implications for Drug Design,” *J. Med. Chem.*, vol. 46, no. 21, pp. 4393–4404, Oct. 2003, doi: 10.1021/jm020577m.

[46] J. S. Desgrosellier and D. A. Cheresh, “Integrins in cancer: biological implications and therapeutic opportunities,” *Nat. Rev. Cancer*, vol. 10, no. 1, pp. 9–22, Jan. 2010, doi: 10.1038/nrc2748.

[47] P. Hinterdorfer, W. Baumgartner, H. J. Gruber, K. Schilcher, and H. Schindler, “Detection and localization of individual antibody-antigen recognition events by atomic force microscopy,” *Proc. Natl. Acad. Sci.*, vol. 93, no. 8, pp. 3477–3481, 1996, doi: 10.1073/pnas.93.8.3477.

[48] A. Ebner *et al.*, “Functionalization of probe tips and supports for single-molecule recognition force microscopy.,” *Top. Curr. Chem.*, vol. 285, pp. 29–76, 2008, doi: 10.1007/128_2007_24.

[49] L. Wildling *et al.*, “Linking of Sensor Molecules with Amino Groups to Amino-Functionalized AFM Tips,” *Bioconjug. Chem.*, vol. 22, no. 6, pp. 1239–1248, Jun. 2011, doi: 10.1021/bc200099t.

[50] Bell George I., “Models for the Specific Adhesion of Cells to Cells,” *Science*, vol. 200, no. 4342, pp. 618–627, May 1978, doi: 10.1126/science.347575.

[51] H. A. Kramers, “Brownian motion in a field of force and the diffusion model of chemical reactions,” *Physica*, vol. 7, no. 4, pp. 284–304, Apr. 1940, doi: 10.1016/S0031-8914(40)90098-2.

[52] P. Hänggi, P. Talkner, and M. Borkovec, “Reaction-rate theory: fifty years after Kramers,” *Rev. Mod. Phys.*, vol. 62, no. 2, pp. 251–341, Apr. 1990, doi: 10.1103/RevModPhys.62.251.

[53] S. N. Zhurkov, “Kinetic concept of the strength of solids,” *Int. J. Fract.*, vol. 26, no. 4, pp. 295–307, Dec. 1984, doi: 10.1007/BF00962961.

[54] T. Strunz, K. Oroszlan, I. Schumakovitch, H.-J. Güntherodt, and M. Hegner, “Model Energy Landscapes and the Force-Induced Dissociation of Ligand-Receptor Bonds,” *Biophys. J.*, vol. 79, no. 3, pp. 1206–1212, Sep. 2000, doi: 10.1016/S0006-3495(00)76375-2.

[55] T. Lecuit and P.-F. Lenne, “Cell surface mechanics and the control of cell shape, tissue patterns and morphogenesis,” *Nat. Rev. Mol. Cell Biol.*, vol. 8, no. 8, pp. 633–644, Aug. 2007, doi: 10.1038/nrm2222.

[56] M. P. Sheetz, “Cell control by membrane-cytoskeleton adhesion.,” *Nat. Rev. Mol. Cell Biol.*, vol. 2, no. 5, pp. 392–396, May 2001, doi: 10.1038/35073095.

[57] D. E. Discher, P. Janmey, and Y.-L. Wang, “Tissue cells feel and respond to the stiffness of their substrate.,” *Science*, vol. 310, no. 5751, pp. 1139–1143, Nov. 2005, doi: 10.1126/science.1116995.

[58] V. Vogel and M. Sheetz, “Local force and geometry sensing regulate cell functions.,” *Nat. Rev. Mol. Cell Biol.*, vol. 7, no. 4, pp. 265–275, Apr. 2006, doi: 10.1038/nrm1890.

[59] W. A. Lam, M. J. Rosenbluth, and D. A. Fletcher, “Chemotherapy exposure increases leukemia cell stiffness.,” *Blood*, vol. 109, no. 8, pp. 3505–3508, Apr. 2007, doi: 10.1182/blood-2006-08-043570.

[60] D. Yamazaki, S. Kurisu, and T. Takenawa, “Regulation of cancer cell motility through actin reorganization.,” *Cancer Sci.*, vol. 96, no. 7, pp. 379–386, Jul. 2005, doi: 10.1111/j.1349-7006.2005.00062.x.

[61] J. Rao and N. Li, “Microfilament actin remodeling as a potential target for cancer drug development.,” *Curr. Cancer Drug Targets*, vol. 4, no. 4, pp. 345–354, Jun. 2004, doi: 10.2174/1568009043332998.

[62] D. Gaspar, J. M. Freire, T. R. Pacheco, J. T. Barata, and M. A. R. B. Castanho, "Apoptotic human neutrophil peptide-1 anti-tumor activity revealed by cellular biomechanics.," *Biochim. Biophys. Acta*, vol. 1853, no. 2, pp. 308–316, Feb. 2015, doi: 10.1016/j.bbamcr.2014.11.006.

[63] M. Plodinec *et al.*, "The nanomechanical signature of breast cancer.," *Nat. Nanotechnol.*, vol. 7, no. 11, pp. 757–765, Nov. 2012, doi: 10.1038/nnano.2012.167.

[64] B. C. Özdemir *et al.*, "Depletion of carcinoma-associated fibroblasts and fibrosis induces immunosuppression and accelerates pancreas cancer with reduced survival.," *Cancer Cell*, vol. 25, no. 6, pp. 719–734, Jun. 2014, doi: 10.1016/j.ccr.2014.04.005.

[65] D. T. Butcher, T. Alliston, and V. M. Weaver, "A tense situation: forcing tumour progression.," *Nat. Rev. Cancer*, vol. 9, no. 2, pp. 108–122, Feb. 2009, doi: 10.1038/nrc2544.

[66] R. Sinkus, J. Lorenzen, D. Schrader, M. Lorenzen, M. Dargatz, and D. Holz, "High-resolution tensor MR elastography for breast tumour detection.," *Phys. Med. Biol.*, vol. 45, no. 6, pp. 1649–1664, Jun. 2000, doi: 10.1088/0031-9155/45/6/317.

[67] R. L. J. Satcher and C. F. J. Dewey, "Theoretical estimates of mechanical properties of the endothelial cell cytoskeleton.," *Biophys. J.*, vol. 71, no. 1, pp. 109–118, Jul. 1996, doi: 10.1016/S0006-3495(96)79206-8.

[68] P. A. Janmey, U. Euteneuer, P. Traub, and M. Schliwa, "Viscoelastic properties of vimentin compared with other filamentous biopolymer networks.," *J. Cell Biol.*, vol. 113, no. 1, pp. 155–160, Apr. 1991, doi: 10.1083/jcb.113.1.155.

[69] C. C.-L. Wong *et al.*, "Hypoxia-inducible factor 1 is a master regulator of breast cancer metastatic niche formation.," *Proc. Natl. Acad. Sci. U. S. A.*, vol. 108, no. 39, pp. 16369–16374, Sep. 2011, doi: 10.1073/pnas.1113483108.

[70] D. Huang *et al.*, "Hypoxia induces actin cytoskeleton remodeling by regulating the binding of CAPZA1 to F-actin via PIP2 to drive EMT in hepatocellular carcinoma.," *Cancer Lett.*, vol. 448, pp. 117–127, Apr. 2019, doi: 10.1016/j.canlet.2019.01.042.

[71] B. A. Teicher, "Hypoxia and drug resistance.," *Cancer Metastasis Rev.*, vol. 13, no. 2, pp. 139–168, Jun. 1994, doi: 10.1007/BF00689633.

[72] T. Puntheeranurak, I. Neundlinger, R. K. H. Kinne, and P. Hinterdorfer, "Single-molecule recognition force spectroscopy of transmembrane transporters on living cells.," *Nat. Protoc.*, vol. 6, no. 9, pp. 1443–1452, Sep. 2011, doi: 10.1038/nprot.2011.370.

[73] X. Lu and Y. Kang, "Hypoxia and hypoxia-inducible factors: master regulators of metastasis.," *Clin. Cancer Res. Off. J. Am. Assoc. Cancer Res.*, vol. 16, no. 24, pp. 5928–5935, Dec. 2010, doi: 10.1158/1078-0432.CCR-10-1360.

[74] W. R. Wilson and M. P. Hay, “Targeting hypoxia in cancer therapy.,” *Nat. Rev. Cancer*, vol. 11, no. 6, pp. 393–410, Jun. 2011, doi: 10.1038/nrc3064.

[75] G. Bao and S. Suresh, “Cell and molecular mechanics of biological materials.,” *Nat. Mater.*, vol. 2, no. 11, pp. 715–725, Nov. 2003, doi: 10.1038/nmat1001.

[76] Y. F. Dufrêne *et al.*, “Imaging modes of atomic force microscopy for application in molecular and cell biology,” *Nat. Nanotechnol.*, vol. 12, no. 4, pp. 295–307, Apr. 2017, doi: 10.1038/nnano.2017.45.

[77] M. I. Confeld *et al.*, “Targeting the Tumor Core: Hypoxia-Responsive Nanoparticles for the Delivery of Chemotherapy to Pancreatic Tumors.,” *Mol. Pharm.*, vol. 17, no. 8, pp. 2849–2863, Aug. 2020, doi: 10.1021/acs.molpharmaceut.0c00247.

[78] P. Kulkarni, M. K. Haldar, S. You, Y. Choi, and S. Mallik, “Hypoxia-Responsive Polymersomes for Drug Delivery to Hypoxic Pancreatic Cancer Cells.,” *Biomacromolecules*, vol. 17, no. 8, pp. 2507–2513, Aug. 2016, doi: 10.1021/acs.biomac.6b00350.

[79] H.-J. Butt and M. Jaschke, “Calculation of thermal noise in atomic force microscopy,” *Nanotechnology*, vol. 6, no. 1, pp. 1–7, Jan. 1995, doi: 10.1088/0957-4484/6/1/001.

[80] M. Rodríguez-Nieto *et al.*, “Viscoelastic properties of doxorubicin-treated HT-29 cancer cells by atomic force microscopy: the fractional Zener model as an optimal viscoelastic model for cells.,” *Biomech. Model. Mechanobiol.*, vol. 19, no. 3, pp. 801–813, Jun. 2020, doi: 10.1007/s10237-019-01248-9.

[81] A. Touhami, B. Nysten, and Y. F. Dufrêne, “Nanoscale Mapping of the Elasticity of Microbial Cells by Atomic Force Microscopy,” *Langmuir*, vol. 19, no. 11, pp. 4539–4543, May 2003, doi: 10.1021/la034136x.

[82] D. C. Lin, E. K. Dimitriadis, and F. Horkay, “Robust strategies for automated AFM force curve analysis--I. Non-adhesive indentation of soft, inhomogeneous materials.,” *J. Biomech. Eng.*, vol. 129, no. 3, pp. 430–440, Jun. 2007, doi: 10.1115/1.2720924.

[83] N. Walter, T. Busch, T. Seufferlein, and J. P. Spatz, “Elastic moduli of living epithelial pancreatic cancer cells and their skeletonized keratin intermediate filament network.,” *Biointerphases*, vol. 6, no. 2, pp. 79–85, Jun. 2011, doi: 10.1116/1.3601755.

[84] M. Nikkhah, J. S. Strobl, E. M. Schmelz, and M. Agah, “Evaluation of the influence of growth medium composition on cell elasticity.,” *J. Biomech.*, vol. 44, no. 4, pp. 762–766, Feb. 2011, doi: 10.1016/j.jbiomech.2010.11.002.

[85] P. Jiang *et al.*, “Novel anti-glioblastoma agents and therapeutic combinations identified from a collection of FDA approved drugs.,” *J. Transl. Med.*, vol. 12, p. 13, Jan. 2014, doi: 10.1186/1479-5876-12-13.

[86] E. C. Faria *et al.*, “Measurement of elastic properties of prostate cancer cells using AFM.,” *The Analyst*, vol. 133, no. 11, pp. 1498–1500, Nov. 2008, doi: 10.1039/b803355b.

[87] N. Colwell *et al.*, “Hypoxia in the glioblastoma microenvironment: shaping the phenotype of cancer stem-like cells.,” *Neuro-Oncol.*, vol. 19, no. 7, pp. 887–896, Jul. 2017, doi: 10.1093/neuonc/now258.

[88] M. A. Jordan and L. Wilson, “Microtubules as a target for anticancer drugs.,” *Nat. Rev. Cancer*, vol. 4, no. 4, pp. 253–265, Apr. 2004, doi: 10.1038/nrc1317.

[89] C. O. Nyongesa and S. Park, “Chemotherapeutic resistance: a nano-mechanical point of view.,” *Biol. Chem.*, vol. 399, no. 12, pp. 1433–1446, Nov. 2018, doi: 10.1515/hsz-2018-0274.

[90] N. P. B. Au, Y. Fang, N. Xi, K. W. C. Lai, and C. H. E. Ma, “Probing for chemotherapy-induced peripheral neuropathy in live dorsal root ganglion neurons with atomic force microscopy.,” *Nanomedicine Nanotechnol. Biol. Med.*, vol. 10, no. 6, pp. 1323–1333, Aug. 2014, doi: 10.1016/j.nano.2014.03.002.

[91] F. Yang, S. S. Teves, C. J. Kemp, and S. Henikoff, “Doxorubicin, DNA torsion, and chromatin dynamics.,” *Biochim. Biophys. Acta*, vol. 1845, no. 1, pp. 84–89, Jan. 2014, doi: 10.1016/j.bbcan.2013.12.002.

[92] K. Fraczkowska *et al.*, “Alterations of biomechanics in cancer and normal cells induced by doxorubicin.,” *Biomed. Pharmacother. Biomedecine Pharmacother.*, vol. 97, pp. 1195–1203, Jan. 2018, doi: 10.1016/j.biopha.2017.11.040.

[93] M. Li, L. Liu, X. Xiao, N. Xi, and Y. Wang, “Effects of methotrexate on the viscoelastic properties of single cells probed by atomic force microscopy.,” *J. Biol. Phys.*, vol. 42, no. 4, pp. 551–569, Oct. 2016, doi: 10.1007/s10867-016-9423-6.

[94] J. L. Nitiss, “Targeting DNA topoisomerase II in cancer chemotherapy.,” *Nat. Rev. Cancer*, vol. 9, no. 5, pp. 338–350, May 2009, doi: 10.1038/nrc2607.

[95] S. E. Cross, Y.-S. Jin, Q.-Y. Lu, J. Rao, and J. K. Gimzewski, “Green tea extract selectively targets nanomechanics of live metastatic cancer cells.,” *Nanotechnology*, vol. 22, no. 21, p. 215101, May 2011, doi: 10.1088/0957-4484/22/21/215101.

[96] A. L. Harris, “Hypoxia--a key regulatory factor in tumour growth.,” *Nat. Rev. Cancer*, vol. 2, no. 1, pp. 38–47, Jan. 2002, doi: 10.1038/nrc704.

[97] B. Muz, P. de la Puente, F. Azab, and A. K. Azab, “The role of hypoxia in cancer progression, angiogenesis, metastasis, and resistance to therapy.,” *Hypoxia Auckl. NZ*, vol. 3, pp. 83–92, 2015, doi: 10.2147/HP.S93413.

[98] A. Zieseniss, “Hypoxia and the modulation of the actin cytoskeleton - emerging interrelations.,” *Hypoxia Auckl. NZ*, vol. 2, pp. 11–21, 2014, doi: 10.2147/HP.S53575.

[99] C.-H. Chang, H.-H. Lee, and C.-H. Lee, “Substrate properties modulate cell membrane roughness by way of actin filaments.,” *Sci. Rep.*, vol. 7, no. 1, p. 9068, Aug. 2017, doi: 10.1038/s41598-017-09618-y.

[100] R. Voisard *et al.*, “The in-vitro effect of antineoplastic agents on proliferative activity and cytoskeletal components of plaque-derived smooth-muscle cells from human coronary arteries.,” *Coron. Artery Dis.*, vol. 4, no. 10, pp. 935–942, Oct. 1993, doi: 10.1097/00019501-199310000-00014.

[101] A. E. Pelling, F. S. Veraitch, C. P.-K. Chu, C. Mason, and M. A. Horton, “Mechanical dynamics of single cells during early apoptosis.,” *Cell Motil. Cytoskeleton*, vol. 66, no. 7, pp. 409–422, Jul. 2009, doi: 10.1002/cm.20391.

[102] G. Banfalvi, “Methods to detect apoptotic cell death.,” *Apoptosis Int. J. Program. Cell Death*, vol. 22, no. 2, pp. 306–323, Feb. 2017, doi: 10.1007/s10495-016-1333-3.

[103] R. C. Taylor, S. P. Cullen, and S. J. Martin, “Apoptosis: controlled demolition at the cellular level.,” *Nat. Rev. Mol. Cell Biol.*, vol. 9, no. 3, pp. 231–241, Mar. 2008, doi: 10.1038/nrm2312.

[104] N. S. H. Motlagh, P. Parvin, F. Ghasemi, and F. Atyabi, “Fluorescence properties of several chemotherapy drugs: doxorubicin, paclitaxel and bleomycin.,” *Biomed. Opt. Express*, vol. 7, no. 6, pp. 2400–2406, Jun. 2016, doi: 10.1364/BOE.7.002400.

[105] J. Lankelma *et al.*, “Doxorubicin gradients in human breast cancer.,” *Clin. Cancer Res. Off. J. Am. Assoc. Cancer Res.*, vol. 5, no. 7, pp. 1703–1707, Jul. 1999.

[106] J. F. Casella, M. D. Flanagan, and S. Lin, “Cytochalasin D inhibits actin polymerization and induces depolymerization of actin filaments formed during platelet shape change.,” *Nature*, vol. 293, no. 5830, pp. 302–305, Sep. 1981, doi: 10.1038/293302a0.

[107] H. Takamatsu, R. Takeya, S. Naito, and H. Sumimoto, “On the mechanism of cell lysis by deformation.,” *J. Biomech.*, vol. 38, no. 1, pp. 117–124, Jan. 2005, doi: 10.1016/j.jbiomech.2004.03.011.

[108] A. Kubiak, T. Zieliński, J. Pabijan, and M. Lekka, “Nanomechanics in Monitoring the Effectiveness of Drugs Targeting the Cancer Cell Cytoskeleton.,” *Int. J. Mol. Sci.*, vol. 21, no. 22, Nov. 2020, doi: 10.3390/ijms21228786.

[109] S. E. Leggett, A. M. Hruska, M. Guo, and I. Y. Wong, “The epithelial-mesenchymal transition and the cytoskeleton in bioengineered systems,” *Cell Commun. Signal. CCS*, vol. 19, no. 1, pp. 32–32, Mar. 2021, doi: 10.1186/s12964-021-00713-2.

[110] L. Alhalhooly, B. Mamnoon, J. Kim, S. Mallik, and Y. Choi, “Dynamic cellular biomechanics in responses to chemotherapeutic drug in hypoxia probed by atomic force spectroscopy,” *Oncotarget*, vol. 12, no. 12. 2021. [Online]. Available: https://www.oncotarget.com/article/27974/

[111] P. Moreno-Layseca and C. H. Streuli, “Signalling pathways linking integrins with cell cycle progression,” *Matrix Biol.*, vol. 34, pp. 144–153, Feb. 2014, doi: 10.1016/j.matbio.2013.10.011.

[112] H. E. Balcioglu, H. van Hoorn, D. M. Donato, T. Schmidt, and E. H. J. Danen, “The integrin expression profile modulates orientation and dynamics of force transmission at cell–matrix adhesions,” *J. Cell Sci.*, vol. 128, no. 7, pp. 1316–1326, Apr. 2015, doi: 10.1242/jcs.156950.

[113] J. S. Desgrosellier and D. A. Cheresh, “Integrins in cancer: biological implications and therapeutic opportunities,” *Nat. Rev. Cancer*, vol. 10, no. 1, pp. 9–22, Jan. 2010, doi: 10.1038/nrc2748.

[114] J. D. Humphries, A. Byron, and M. J. Humphries, “Integrin ligands at a glance,” *J. Cell Sci.*, vol. 119, no. 19, pp. 3901–3903, Oct. 2006, doi: 10.1242/jcs.03098.

[115] I. D. Campbell and M. J. Humphries, “Integrin structure, activation, and interactions,” *Cold Spring Harb. Perspect. Biol.*, vol. 3, no. 3, p. a004994, Mar. 2011, doi: 10.1101/cshperspect.a004994.

[116] H. Hamidi and J. Ivaska, “Every step of the way: integrins in cancer progression and metastasis,” *Nat. Rev. Cancer*, vol. 18, no. 9, pp. 533–548, Sep. 2018, doi: 10.1038/s41568-018-0038-z.

[117] A. Hoshino *et al.*, “Tumour exosome integrins determine organotropic metastasis,” *Nature*, vol. 527, no. 7578, pp. 329–335, Nov. 2015, doi: 10.1038/nature15756.

[118] F. Danhier, A. Le Breton, and V. Préat, “RGD-Based Strategies To Target Alpha(v) Beta(3) Integrin in Cancer Therapy and Diagnosis,” *Mol. Pharm.*, vol. 9, no. 11, pp. 2961–2973, Nov. 2012, doi: 10.1021/mp3002733.

[119] F. Li, S. D. Redick, H. P. Erickson, and V. T. Moy, “Force measurements of the alpha5beta1 integrin-fibronectin interaction,” *Biophys. J.*, vol. 84, no. 2 Pt 1, pp. 1252–1262, Feb. 2003, doi: 10.1016/S0006-3495(03)74940-6.

[120] I. Lee and R. E. Marchant, “Force measurements on the molecular interactions between ligand (RGD) and human platelet αIIbβ3 receptor system,” *Surf. Sci.*, vol. 491, no. 3, pp. 433–443, Oct. 2001, doi: 10.1016/S0039-6028(01)01309-7.

[121] P. Hinterdorfer, K. Schilcher, W. Baumgartner, H. J. Gruber, and H. Schindler, “A mechanistic study of the dissociation of individual antibody-antigen pairs by atomic force microscopy,” *Nanobiology*, vol. 4, no. 3, p. 177, 1998, [Online]. Available: https://ezproxy.lib.ndsu.nodak.edu/login?url=https://www.proquest.com/scholarly-journals/mechanistic-study-dissociation-individual/docview/194465134/se-2?accountid=6766

[122] T. Schmidt, G. J. Schütz, W. Baumgartner, H. J. Gruber, and H. Schindler, “Imaging of single molecule diffusion,” *Proc. Natl. Acad. Sci.*, vol. 93, no. 7, pp. 2926–2929, 1996, doi: 10.1073/pnas.93.7.2926.

[123] T. V. Ratto, R. E. Rudd, K. C. Langry, R. L. Balhorn, and M. W. McElfresh, “Nonlinearly Additive Forces in Multivalent Ligand Binding to a Single Protein Revealed with Force Spectroscopy,” *Langmuir*, vol. 22, no. 4, pp. 1749–1757, Feb. 2006, doi: 10.1021/la052087d.

[124] A. Taubenberger, D. A. Cisneros, J. Friedrichs, P.-H. Puech, D. J. Muller, and C. M. Franz, “Revealing Early Steps of α2β1 Integrin-mediated Adhesion to Collagen Type I by Using Single-Cell Force Spectroscopy,” *Mol. Biol. Cell*, vol. 18, no. 5, pp. 1634–1644, May 2007, doi: 10.1091/mbc.e06-09-0777.